



HAL
open science

Study of possible mechanisms of formation and destruction for anions in the interstellar medium.

Miguel Lara Moreno

► **To cite this version:**

Miguel Lara Moreno. Study of possible mechanisms of formation and destruction for anions in the interstellar medium.. Theoretical and/or physical chemistry. Université de Bordeaux, 2018. English. NNT : 2018BORD0220 . tel-02003699

HAL Id: tel-02003699

<https://theses.hal.science/tel-02003699>

Submitted on 1 Feb 2019

HAL is a multi-disciplinary open access archive for the deposit and dissemination of scientific research documents, whether they are published or not. The documents may come from teaching and research institutions in France or abroad, or from public or private research centers.

L'archive ouverte pluridisciplinaire **HAL**, est destinée au dépôt et à la diffusion de documents scientifiques de niveau recherche, publiés ou non, émanant des établissements d'enseignement et de recherche français ou étrangers, des laboratoires publics ou privés.

THÈSE PRÉSENTÉE
POUR OBTENIR LE GRADE DE

**DOCTEUR DE
L'UNIVERSITÉ DE BORDEAUX**

ÉCOLE DOCTORALE DES SCIENCES CHIMIQUES
SPÉCIALITÉ: Chimie-Physique

Par Miguel LARA MORENO

**ÉTUDE DE MÉCANISMES POSSIBLES DE FORMATION ET DESTRUCTION
D'ANIONS EN MILIEU INTERSTELLAIRE**

Sous la direction de: Thierry STOECKLIN
codirecteurs: Philippe HALVICK
Jean-Christophe LOISON

Soutenue le 14/11/2018

Membres de jury:

Mme. VASTEL, Charlotte	Astronome	Université de Toulouse	Président
M. KOKOULINE, Viatcheslav	Professeur	University of Central Florida	Rapporteur
M. ANCARANI, Ugo	Professeur	Université de Lorraine	Rapporteur
M. HOCHLAF, Majdi	Professeur	Université Paris-Est	Examineur
M. LOISON, Jean-Christophe	Directeur de Recherche	Université de Bordeaux	Examineur
M. HALVICK, Philippe	Chargé de Recherche	Université de Bordeaux	Examineur
M. STOECKLIN, Thierry	Directeur de Recherche	Université de Bordeaux	Examineur



Ce travail de thèse a été financé par le programme AnionCosChem de l'Agence Nationale de la Recherche.

Unité de recherche
Institut des Sciences Moléculaires–UMR 5255
Université de Bordeaux. 351 cours de la Libération
33405 TALENCE cedex
FRANCE

Abstract

The mechanisms of formation and destruction of molecular anions have become a field of special interest after the recent detection of six molecular anions (C_4H^- , C_6H^- , C_8H^- , CN^- , C_3N^- , C_5N^-) in the interstellar medium. The main channel of formation of these anions is expected to be radiative electron attachment in environments where the density of electron is relatively important. There is however at the moment a lack of experimental and theoretical data allowing to assess this hypothesis. Photodetachment, on the other hand, is the main source of destruction of the anions in diffuse clouds and photodissociation regions. A single center expansion approach is applied to the study of both processes: photodetachment and radiative electron attachment. The results obtained with the present method are compared to previously reported experimental and theoretical data and show a good agreement. This method is then employed to determine the rate constants which are needed to confirm whether or not these mechanisms are crucial for the chemistry of the interstellar anions. Along with the formation and destruction rates, rotational excitation rate coefficients are needed to accurately model the observed anions abundances. We focus on the calculation of state-to-state rotational transitions rate coefficients of the C_3N^- molecule in its ground vibrational state in collisions with H_2 and He using new potential energy surfaces

KEYWORDS: interstellar anions, radiative electron attachment, photodetachment, state-to-state rate coefficients, potential energy surfaces

Résumé court

L'étude des mécanismes de formation et de destruction des anions moléculaires est devenu un champ d'intérêt prononcé après la détection récente de six anions moléculaires (C_4H^- , C_6H^- , C_8H^- , CN^- , C_3N^- , C_5N^-) dans le milieu interstellaire. Dans les environnements interstellaires où la densité d'électrons est relativement importante, le canal principal de formation de ces anions devrait être l'attachement électronique radiatif. Mais il manque aujourd'hui des données expérimentales et théoriques permettant d'évaluer cette hypothèse. D'autre part, le photodétachement est la principale cause de destruction de ces anions dans les nuages diffus et les régions de photodissociation. Une approche basée sur un développement monocentrique est appliquée à l'étude de ces deux processus opposés que sont le photodétachement et l'attachement électronique radiatif. Les résultats obtenus avec la présente méthode sont comparés à des données expérimentales et théoriques précédemment rapportées et montrent un bon accord. Cette méthode est ensuite utilisée pour déterminer les constantes de vitesse nécessaires pour confirmer si ces mécanismes sont cruciaux pour la chimie d'anions interstellaires. En plus des constantes de vitesse de formation et de destruction des anions, les constantes de vitesse d'excitation collisionnelle sont nécessaires pour modéliser les abondances observées des anions. Nous avons choisi de porter notre effort sur le calcul des constantes de vitesse de transition entre états rotationnels de la molécule C_3N^- dans son état vibrationnel fondamental lors des collisions avec H_2 et He en utilisant de nouvelles surfaces d'énergie potentielles.

MOTS CLÉS: anions interstellaires, attachement électronique radiatif, photodétachement, constantes de vitesse de transitions rotationnelle, surfaces d'énergie potentielle.

Résumé long

Chimie des anions : mécanismes de formation et de destruction

Depuis la détection récente dans le milieu interstellaire des anions moléculaires, la question des mécanismes de leur formation, destruction et excitation est posée. En phase gazeuse, les ions négatifs sont typiquement formés par l'attachement d'un électron sur une molécule neutre. Dans les conditions du milieu interstellaire, c'est-à-dire à température et densité basses, les anions interstellaires sont probablement formés par attachement radiatif.

Les mesures expérimentales des constantes de vitesses d'attachement radiatif sont difficiles à réaliser car un vide presque parfait est nécessaire pour éviter toute stabilisation des anions par collision avec un tiers corps avant une émission radiative qui peut être tardive. Pendant longtemps, les constantes de vitesses d'attachement radiatif ont été obtenues par un modèle statistique. Mais récemment, une nouvelle approche de l'attachement radiatif basée sur les principes fondamentaux a été développée. Les constantes de vitesses d'attachement radiatif obtenues dans cette nouvelle approche sont particulièrement faibles, ce qui invalide la formation des anions interstellaires par attachement radiatif ainsi que cela avait été supposé. En conséquence, des travaux théoriques et expérimentaux supplémentaires sont nécessaires pour bien comprendre si l'attachement radiatif peut être ou non le principal mécanisme de formation des anions interstellaires.

D'autre part, le photodétachement est supposé être l'un des mécanismes les plus importants de destruction des anions interstellaires dans les régions de photodissociation du milieu interstellaire. Jusqu'à présent, les constantes de vitesses de photodétachement étaient principalement obtenues de manière empirique par des expressions mathématiques qui dépendent seulement de l'affinité électronique de la molécule neutre. Il est bien connu que ces expressions empiriques sous-estiment les constantes de vitesses de photodétachement. Une évaluation de meilleure qualité est nécessaire.

En raison de l'importance des mécanismes de formation et de destruction des anions dans les modèles d'astrochimie, nous proposons une nouvelle méthode basée sur un développement monocentrique dans le repère attaché à la molécule et avec diverses approximations de l'orbitale de Dyson. Les méthodes utilisées pour calculer l'orbitale de Dyson ainsi que la fonction d'onde de diffusion sont présentées

en détail. Les résultats obtenus par ces méthodes sont comparés aux données expérimentales existantes pour les trois anions CN^- , O_2^- et OH^- . On observe un bon accord entre les résultats obtenus avec la nouvelle approche et les résultats expérimentaux et théoriques précédents.

Nous avons montré que l'onde plane est une bonne approximation de la fonction d'onde de diffusion pour les molécules étudiées. De plus cette approximation simple réduit fortement le temps de calcul numérique. Les effets de la taille et du type de la base d'orbitales atomiques ont aussi été analysés. Nous avons constaté que les bases d'orbitales de type Slater donnent de meilleurs résultats que les bases d'orbitales de type gaussien, et ceci pour un plus petit nombre de fonctions de bases.

Les constantes de vitesses d'attachement radiatif et de photodétachement ont aussi été calculées pour les six anions détectés dans le milieu interstellaire ainsi que pour plusieurs autres anions appartenant aux familles C_n^- , C_nH^- , C_nN^- , lesquels sont des candidats possibles à la détection dans le milieu interstellaire. La comparaison entre nos constantes de vitesses et celles habituellement utilisées dans les modèles astrochimiques montrent que ces dernières sous-estiment fortement les constantes de vitesses de photodétachement. Utiliser nos constantes de vitesses de photodétachement dans les modèles astrochimiques devrait donc conduire à une forte diminution du rapport d'abondance anion sur neutre, et par suite, diminuer la qualité de l'accord existant actuellement entre les modèles et les observations. Nous avons aussi calculé les constantes de vitesses d'attachement radiatif pour la formation des états fondamentaux ou bien des états dipolaires (états liés par l'interaction charge-dipole) des anions. La comparaison entre nos résultats et les constantes de vitesses d'attachement radiatif utilisées jusqu'à présent montre que ces dernières sont beaucoup plus grandes, jusqu'à plusieurs ordres de grandeur. Nos résultats indiquent donc que les anions interstellaires ne peuvent pas être formés par attachement radiatif, y compris par la formation d'états dipolaires transitoires. En conséquence, l'accord présent entre les abondances observées et celles obtenues par les modèles est discutable.

Analyse des spectres : excitation et désexcitation rotationnelle

Pratiquement tout ce qui est connu sur la chimie du milieu interstellaire est issu des spectres atomiques et moléculaires enregistrés par les télescopes. L'analyse des raies d'émission et d'absorption des molécules dans le but d'en déduire des paramètres physico-chimiques tels que la température, la densité et les abondances moléculaires demande d'utiliser un modèle réaliste du transfert radiatif. A leur tour, ces modèles nécessitent la connaissance des paramètres spectroscopiques des molécules tels que les niveaux d'énergie, les poids statistiques, les fréquences de transition et les coefficients d'Einstein. Ces informations sont généralement obtenues par des mesures expérimentales.

En plus des paramètres spectroscopiques, les modèles de transfert radiatif ont

besoin des constantes de vitesse d'excitation et de désexcitation rotationnelle des molécules sous l'effet des collisions avec les espèces les plus abondantes dans l'environnement des molécules étudiées. Dans le cas du milieu interstellaire, le partenaire de collision le plus abondant est H_2 . Les collisions avec les atomes H, He et les électrons libres peuvent aussi jouer un rôle non négligeable. La connaissance des constantes de vitesse des processus collisionnels est limité à quelques molécules seulement. Dans le cas des anions interstellaires détectés, on a seulement des données sur les constantes de vitesse d'excitation et de désexcitation de CN^- et C_6H^- par collision avec H_2 .

En l'absence de données collisionnelles pour les molécules étudiées, ainsi que c'est le cas pour les anions interstellaires, les astronomes utilisent des approximations pour remédier au manque de données précises. La solution la plus généralement utilisée consiste à supposer que l'équilibre thermodynamique local est établi. Cependant, en raison de la très faible densité du milieu interstellaire, cette approximation peut conduire à des évaluations très imprécises des abondances des anions interstellaires.

En l'absence de données collisionnelles pour les anions interstellaires et en raison de l'importance de ces informations pour l'évaluation des abondances moléculaires, nous avons calculé les constantes de vitesse des transitions rotationnelles d'état à état de C_3N^- induites par collisions avec He et H_2 .

Dans ce but, nous avons construit les modèles numériques des deux surfaces d'énergie potentielle des complexes de van der Waals $\text{He-C}_3\text{N}^-$ et $\text{H}_2\text{-C}_3\text{N}^-$ à partir d'un large ensemble de calculs *ab initio* de haute qualité. Un soin particulier a été apporté à la description des interactions à longue portée, et nous avons constaté que nos modèles numériques sont en très bon accord avec les données des calculs *ab initio*.

Avec les surfaces de potentiel précédemment déterminées, nous avons aussi calculé, par une méthode variationnelle basée entre autres sur une base de fonctions sturmiennes, les états rovibrationnels des complexes $\text{He-C}_3\text{N}^-$ et $\text{H}_2\text{-C}_3\text{N}^-$. Une analyse détaillée des fonctions d'ondes rovibrationnelles obtenues a permis de mettre en évidence des effets quantiques tels que l'effet tunnel, l'effet de mémoire vibrationnelle, et aussi les résonances anharmoniques. Par exemple, l'effet tunnel a pour conséquence la levée de dégénérescence entre des états liés appartenant à des puits de potentiel distincts, mais équivalents par symétrie d'échange des atomes d'hydrogène dans le cas de $\text{H}_2\text{-C}_3\text{N}^-$. Les fréquences vibrationnelles et les constantes rotationnelles pour les deux complexes ont aussi été calculées. Les résultats obtenus montrent que seul un traitement quantique des mouvements des noyaux atomiques permet de calculer avec précision les énergies rovibrationnelles de ces complexes de van der Waals anioniques.

Les constantes de vitesse des transitions rotationnelles d'état à état de C_3N^- induites par collisions avec He et H_2 ont été calculées dans l'intervalle de température [10,300] K par la combinaison des méthodes Close-coupling et Uniform J-shifting. Pour les collisions avec He, une tendance forte pour les transitions telles

que $\Delta j_{C_3N^-} = 2$ a été observée pour les petites valeurs de $\Delta j_{C_3N^-}$, alors que pour les grandes valeurs de $\Delta j_{C_3N^-}$, ce sont les valeurs impaires qui sont favorisées. Inversement, pour les collisions avec l'*ortho*-H₂ et le *para*-H₂, c'est la tendance $\Delta j_{C_3N^-} = 1$ qui est observée. La forte ressemblance, spécialement à haute température, entre les constantes de vitesse avec *ortho*-H₂ et avec *para*-H₂ est un résultat important pour ce système. Cela peut être attribué à l'anisotropie du potentiel d'interaction et aussi à l'interaction répulsive à courte distance. Nous avons aussi testé l'approximation qui consiste à déterminer les constantes de vitesse des transitions induites par collision avec *para*-H₂ à partir de celles calculées dans les collisions avec He multipliées par le rapport des masses réduites. On montre que cette approximation est largement erronée et donne des lois de tendance fausses.

Nous avons aussi évalué la qualité de l'estimation des constantes de vitesse de désexcitation rotationnelle de C₃N⁻ par collision avec H₂ à partir des constantes de vitesse connues pour CN⁻ et C₆H⁻. On observe que l'accord entre les constantes de vitesse pour CN⁻ et C₃N⁻ est relativement bon, mais seulement pour les transitions avec des petites valeurs de Δj , alors que pour les grandes valeurs, les constantes de vitesse pour CN⁻ sont plus petites que celles pour C₃N⁻. Plus la molécule est grande et plus le potentiel d'interaction à courte distance est répulsif, ce qui favorise les transitions rotationnelles avec un grand Δj . Les résultats avec C₆H⁻ sont au contraire en bon accord avec ceux pour C₃N⁻ pour toutes les transitions. On peut donc supposer que des effets similaires à ceux observés pour C₃N⁻ et C₆H⁻ pourrait aussi exister pour les autres chaînes longues de leurs familles respectives C_{2n+1}N⁻ et C_{2n}H⁻, ce qui permettrait d'évaluer les constantes de vitesse à partir de ces premières.

Effet tunnel dans les complexes moléculaires faiblement liés

Les propriétés physiques et chimiques des complexes moléculaires faiblement liés sont susceptibles de présenter des aspects complexes dont certains peuvent être observés expérimentalement. On peut citer l'effet tunnel, la localisation des mouvements vibrationnels, les résonances quantiques, la variation non-Arrhenius des constantes de vitesse. Certains de ces effets ne sont pas encore complètement compris, surtout quand une physico-chimie non-intuitive est en action. Il est donc important d'étudier ces effets quantiques avec les techniques théoriques et expérimentales les plus avancées.

Nous présentons des calculs précis des états vibrationnels inter-monomère du système de van der Waals CO₂-N₂. Les effets des permutations des atomes identiques sont pris en compte et examinés. L'effet le plus notable est l'existence de puits de potentiel symétriquement équivalents, ce qui mène à une levée de dégénérescence systématique induite par l'effet tunnel. L'examen des fonctions d'onde a révélé des caractéristiques imprévues : la fonction d'onde fondamentale a plusieurs plan nodaux et les fonctions d'ondes d'états hautement excités sont localisées dans

de petites régions de l'espace des coordonnées bien que la délocalisation dans presque tout l'espace soit permise. Un bon accord avec les énergies de transition rotationnelles expérimentales a été obtenu, ce qui confirme l'exactitude de notre modèle 4D de surface d'énergie potentielle ainsi que du traitement quantique des mouvements nucléaires.

En plus de son importance pour la chimie atmosphérique, ce travail révèle que la structure et la spectroscopie du complexe $\text{CO}_2\text{-N}_2$ sont gouvernés des effets quantiques qui sont l'effet tunnel, des mouvements de grande amplitude, des résonances anharmoniques et la localisation vibrationnelle. Leurs signatures spectroscopiques ont déjà été observées expérimentalement et sont analysées ici. Le travail présent suggère que leur spectroscopie et dynamique ne peuvent pas être complètement comprises sans la prise en compte de l'effet tunnel.

Contents

Introduction	1
1 Theoretical framework	7
1.1 Schrödinger equation	8
1.1.1 Born-Oppenheimer approximation	9
1.2 Electronic structure calculation	10
1.2.1 Hartree-Fock method	10
1.2.2 Multi-configurational self-consistent field method	11
1.2.3 Coupled cluster methods	11
1.2.4 Basis sets	13
1.3 Quantum nuclear motions	13
1.3.1 Coupled channel method	14
1.3.2 Variational approach	14
2 A single center approach to REA and PD	19
2.1 Introduction	20
2.2 Theory	21
2.2.1 REA and PD cross sections	21
2.2.2 Calculation of the Dyson orbital	22
2.2.3 Calculation of the electron continuum wave function	23
2.2.3.1 Scattered wave	23
2.2.3.2 Plane wave	26
2.3 Parameters of the calculations	26
2.3.1 Dyson orbital	26
2.3.2 Continuum wave function	27
2.3.2.1 Scattered wave	27
2.3.2.2 Plane wave	27
2.3.3 Spin and electronic degeneracies	28
2.4 Comparison between theory and experiment	28
2.4.1 Comparison of the methods and basis sets for the Dyson orbital evaluations	32

2.5	Conclusion	34
3	REA and PD rate coefficients	37
3.1	Introduction	38
3.2	Methods	39
3.3	PD rate coefficients	39
3.4	REA rate coefficients	41
3.4.1	REA through the formation of dipole bound states	44
3.5	Conclusions	45
4	Interaction of rigid C_3N^- with He	47
4.1	Introduction	48
4.2	PES: ab-initio calculations and functional form	48
4.2.1	Features of the PES	51
4.3	Bound states calculations	52
4.4	Rovibrational spectrum	57
4.5	Conclusion	58
5	Rotational relaxation of C_3N^- by collisions with He	61
5.1	Introduction	62
5.2	Methods	63
5.2.1	The atom-linear rigid rotor coupled equations	63
5.2.2	PES and the matrix element of the potential	65
5.2.3	Inelastic boundary conditions and cross sections	66
5.2.4	Scattering calculations and rate coefficients	66
5.3	Results	68
5.4	Conclusions	73
6	Interaction of rigid C_3N^- with H_2	75
6.1	Introduction	76
6.2	Ab-initio calculations	76
6.3	Analytical representation of PES	77
6.3.1	Features of the PES	78
6.3.2	Long-range intermolecular forces	79
6.4	Bound states	82
6.4.1	Vibrational levels and wave functions	83
6.4.1.1	Vibrational frequencies	90
6.4.1.2	Rotational Constants	90
6.4.2	Para and ortho states	90
6.5	Conclusion	91

7	Rotational relaxation of C_3N^- by collision with H_2	93
7.1	Introduction	94
7.2	Method	94
7.2.1	The two linear rigid rotors coupled equations	94
7.2.2	PES and the coupling matrix elements	96
7.2.3	Boundary conditions and cross sections	98
7.2.4	Parameters of the calculations	98
7.2.5	Computational methodology	99
7.3	Results	100
7.4	Conclusions	104
8	Quantum tunneling in weakly bound complexes	107
8.1	Introduction	108
8.2	Variational bound states calculations	109
8.2.1	The CO_2-N_2 PES	109
8.2.2	Symmetry of the CO_2-N_2 vibrational wave functions	111
8.3	Vibrational normal modes – asymmetric top model	111
8.3.1	Symmetry considerations	113
8.4	Rovibrational bound states	115
8.5	Rovibrational spectrum	122
8.5.1	Dipole moment operator and selection rules	123
8.5.2	Nuclear spin wave function and spin statistic	123
8.5.3	Comparison with experiments	124
8.6	Conclusion	125
	General conclusions	127
A	Dyson orbital calculation	131
B	J-shifting approaches	135
C	The character tables	137
	Bibliography	139

Acronyms

aug-cc-pVNZ augmented correlation consistent polarized valence N-tuple zeta

B3LYP Becke 3-parameter Lee-Yang-Parr

BO Born-Oppenheimer

BSSE basis set superposition error

CASSCF complete active space self-consistent field

CC close coupling

CCSD(T) coupled cluster with single and double excitation and a perturbative treatment of triplet excitations

CPU central processing unit

DEA dissociative electron attachment

DFT density functional theory

DIB diffuse interstellar band

DVR discrete variable representation

FBA first Born approximation

FBR finite basis representation

FTMW Fourier transform microwave

GTO Gaussian type orbital

HF Hartree-Fock

HFFC Hartree-Fock frozen-core

- HFEGE** Hara's free electron gas exchange
- HOMO** highest occupied molecular orbital
- IOS** infinite order sudden
- ISM** interstellar medium
- KS** Kohn-Sham
- LTE** local thermal equilibrium
- MCSCF** multi-configurational self-consistent field
- MPI** message passing interface
- PD** photodetachment
- PES** potential energy surface
- REA** radiative electron attachment
- RMS** root mean square
- STO** Slater type orbital
- TBEA** third-body electron attachment
- UJS** uniform J-shifting
- VBR** variational basis representation

Introduction

Over the last 50 years, the formation of interstellar anions and their likely detection have been a controversial topic inside the astrochemistry community, starting with Dalgarno and McCray [1] who for the first time explored the role of anions, specifically H^- , O^- , C^- , CH^- , C_2H^- , CN^- , and S^- , in the formation of simple molecules in interstellar clouds. At that time it was concluded that interstellar anions were scarce and their contribution to the formation of other molecular species insignificant. These results were attributed to their relatively slow rate of formation through radiative electron attachment ($\sim 10^{-15} \text{ cm}^3\text{molecule}^{-1}\text{s}^{-1}$).

A few years later, based on a simple statistical model, Herbst [2] suggested that anions could be efficiently formed in dense interstellar clouds. Herbst suggested that for large neutral species with large electron affinity (C_4H , C_3N , C_5N , C_9N , etc) the radiative attachment rate could be near to the collision limit $\sim 10^{-7} \text{ cm}^3\text{molecule}^{-1}\text{s}^{-1}$. One of the most relevant results of this work was the prediction of an anion-to-neutral ratio between 1-10% which was later corroborated in astronomical observations.

In the late nineties, Tulej et al. [3] suggested that the negatively charged ions C_6^- to C_9^- , and more specifically C_7^- , could be responsible for some of the diffuse interstellar bands (DIBs). Subsequently, Terzieva and Herbst [4] examined the possible formation of these anions in interstellar diffuse clouds by radiative electron attachment and concluded that the abundance of large C_n^- anion could be prominent if the neutral precursors were copious and the reaction with the most abundant neutral species (such as H_2) did not occur. However, a few years later, the hypothesis of C_7^- being a carrier of DIBs was rejected with the advent of new high-resolution astronomical and laboratory spectroscopy data [5].

A few attempts were made to search for negative ions in molecular clouds. However, due to a lack of spectroscopic information on negative ions, these searches were either unsuccessful or leading to tentative detections [6]. The definite proof that anions could exist in interstellar medium came on 2006, when McCarthy et al. [7] detected for the first time C_6H^- in the circumstellar envelope IRC+10216 and the dark cloud TMC-1. The anion-to-neutral ratios were in agreement with the early predictions of Herbst: 1–5 % for IRC+10216 and 2.5 % for TMC-1, thus support-

Table 1: Anion-to-Neutral Ratios. Extracted from Table 1 of reference [8]

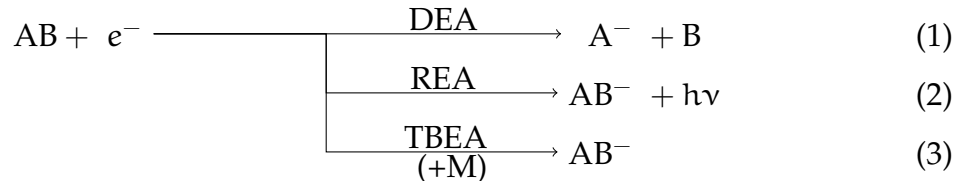
Source	C ₄ H ⁻	C ₆ H ⁻	C ₈ H ⁻	CN ⁻	C ₃ N ⁻	C ₅ N ⁻	References
TMC-1	0.0012%	1.6%	4.6%	≤ 3%	≤ 0.74%	–	[9–13]
L1544	–	2.5%	–	–	–	–	[14]
L1512F	–	4.0%	–	–	–	–	[14]
Lupus-1A	0.0088%	2.1%	4.7%	–	–	–	[15]
L1251A	–	3.6%	–	–	–	–	[16]
L1512	–	4.1%	–	–	–	–	[16]
L1527	0.0110%	9.3%		≤ 0.2%	–	–	[11, 12, 17]
IRC+10216	0.0240%	6.2%	26%	0.25%	0.52%	13%	[10, 18–21]

ing the hypothesis that anions could be efficiently synthesized in the interstellar medium (ISM) by radiative electron attachment. The detection of C₆H⁻ led to the subsequent detection of five other anions, namely C₄H⁻, C₈H⁻, CN⁻, C₃N⁻, C₅N⁻, in a variety of interstellar sources, see Table 1.

These observations gave rise quickly to new chemical models of the interstellar sources where the anions have been detected as well as other likely sources [18, 19, 22–24]. These models yielded anion-to-neutral ratios which were reasonably successful at reproducing observations for the largest anions (C₆H⁻, C₈H⁻, C₇N⁻) and less successful for smallest anions (CN⁻, C₄H⁻, C₃N⁻). Further investigations of the processes that form and destroy anions in the interstellar medium should help to solve these discrepancies.

Chemistry of anions

In the gas phase, negative ions are typically formed by the attachment of an electron to a neutral molecule. Depending on the molecule, the electron energy and the densities of particles in the medium, this collision process proceed toward one or more of the following exit channels:



Path (1) corresponds to dissociative electron attachment (DEA), in which the incoming electron attaches to a neutral molecule and then the molecular anion dissociates. In process (2) the anion is stabilized by the emission of a photon (often called radiative electron attachment, REA) while in the process (3), stabilization occurs by collision with a third body (often called third-body electron attachment, TBEA).

DEA is typically endothermic (i.e. the electron affinity is smaller than the chemical bonding energy), and so proceeds at slow rates at low temperatures. However as discussed by Herbst and Osamura [25], there might be some slightly exothermic

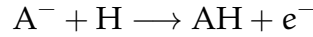
DEA processes, such as:



which might have a great contribution to the formation of interstellar anions. TBEA, on the other hand, will play an important role at low temperatures but it requires large densities of either AB or another gas M to act as a third-body for the collisional stabilization. Thus collisional stabilization is unlikely to occur in the ISM owing to the low density of the gas phase. Therefore, REA is the most likely mechanism to occur in the physical conditions of the ISM.

Experimental determinations of the REA rates are difficult to obtain due to the excellent vacuum conditions which are required to prevent collisional stabilization. For many years, the REA rates have been determined using the statistical model proposed by Herbst [2]. However, as mentioned before, these rates fail at reproducing the anion-to-neutral ratio of the small anions. Recently, Kokoouline et al. [26–29] developed a new approach to REA based on first principles and obtained REA rate coefficients which are several orders of magnitude smaller than those previously obtained by Herbst, thus concluding that REA cannot explain the formation of interstellar anions. Therefore, more theoretical and experimental data are required to clarify whether or not REA can be the main mechanism of formation of interstellar anions.

One of the most relevant processes that lead to the destruction of interstellar molecular anions is the reaction with the most abundant neutral species, namely H and H₂:



This process, which is called associative detachment, is often exothermic and occurs rapidly at low temperatures. For example the reaction of anions with atomic hydrogen occurs at rates $\sim 10^{-10} \text{ cm}^3 \text{ molecule}^{-1} \text{ s}^{-1}$ [30].

Photodetachment (PD), the reverse process of REA, is a major channel for photo-dissociation regions



Rates for PD are obtained from the absolute cross section which is estimated using the empirical formula [23]

$$\sigma_{\text{PD}} = 10^{-17} \left(1 - \frac{E_{\text{EA}}}{E} \right)^{1/2} \text{ cm}^2 \quad (4)$$

which only depends on the neutral electron affinity threshold E_{EA} . Recently, Kumar et al. [31] has shown that the use of equation (4) underestimate the PD rates, thus overestimating the anion-to-neutral fractional abundance. Hence, a better description of the PD process may be a solution to the discrepancy found between the astrochemical models and the observations.

Owing to the importance of the mechanisms of formation and destruction of anions in the astrochemical models, the first objective of this thesis is to develop a theoretical method that accurately yields both REA and PD rates.

Analysis of the molecular spectra

Almost all of what we know about the ISM is based on the interpretation of spectral lines detected by the telescopes. Analysis of the emission and absorption lines of a molecule to infer physical and chemical parameters such as temperature, density, and molecular abundances requires an efficient modeling of the radiative transfer. Radiative transfer models require the knowledge of spectroscopic data of the molecule such as: energy levels, statistical weights, line frequencies and Einstein coefficients. Usually, this information is obtained from experiments.

Besides the spectroscopic data, radiative transfer models rely also on excitation and de-excitation rates of the molecule induced by collision with the most abundant species around the molecule. In the case of the ISM, the most abundant collision partner is H_2 , however collisions with atomic H, He and electrons are sometimes relevant. The availability of collisional rates is limited to a few molecules only. Among the approximately 200 molecules that have been detected so far, there is only about one-fifth of them for which collisional rates are available in the specialized databases BASECOL¹ and LAMBDA². The lack of data is even worse in the case of detected interstellar anions, since there is only information of the excitation and de-excitation rates of CN^- [32] and C_6H^- [33] in collisions with H_2 .

When there is no collisional data for the molecule of interest, as it is the case for most of the interstellar anions, the astronomers use certain approximations to remedy the lack of information. One of the most widely used workarounds is to assume that the local thermal equilibrium (LTE) is established, which is equivalent to assume that the energy levels are populated according to the Maxwell-Boltzmann distribution for a given temperature. LTE conditions are satisfied at high densities when collisions determine the excitation of molecular modes of motion. However, owing to the low densities of ISM, the LTE approximation might be inaccurate. Indeed, at low densities, the radiative decay may compete with collisions and as a result, the energy level distribution will deviate from the Maxwell-Boltzmann distribution. Therefore LTE approximation can lead to inaccurate determination of the molecular abundance of the interstellar anions.

Due to the lack of collisional data for the interstellar anions and the importance that this information has in the determination of the molecular abundances, the second objective of this thesis is to calculate the rate coefficients for state-to-state rota-

¹<http://basecol.obspm.fr>

²<http://home.strw.leidenuniv.nl/~moldata>

tional transitions of C_3N^- induced by collisions with both H_2 and He.

Quantum tunneling in weakly bound complexes

The physical and chemical properties of weakly bound molecular systems may exhibit complex behaviors that could be observed experimentally. Among them, we can cite tunneling, vibrational quantum localization, quantum resonances, non-Arrhenius law evolution of rate constants. Some of these effects remain not yet fully understood, where a non-intuitive physical chemistry is in action. However they are important for understanding the dynamics of complex molecular systems. It is hence worth investigating them using state-of-the-art theoretical and experimental techniques. Due to its importance for atmospheric chemistry the last objective of this thesis is to study the dynamics of the CO_2-N_2 van der Waals complex using a first principle treatment where nuclear motions and nuclear spins are fully considered.

Chapter 1

Theoretical framework

Contents

1.1	Schrödinger equation	8
1.1.1	Born-Oppenheimer approximation	9
1.2	Electronic structure calculation	10
1.2.1	Hartree-Fock method	10
1.2.2	Multi-configurational self-consistent field method	11
1.2.3	Coupled cluster methods	11
1.2.4	Basis sets	13
1.3	Quantum nuclear motions	13
1.3.1	Coupled channel method	14
1.3.2	Variational approach	14

1.1 Schrödinger equation

In quantum mechanics, the state of a system is fully described by a function $\Psi(\mathbf{r}_1, \mathbf{r}_2, \dots, t)$ which evolves in time according to the following equation

$$i\hbar \frac{\partial}{\partial t} \Psi(\mathbf{r}_1, \mathbf{r}_2, \dots, t) = \mathbf{H} \Psi(\mathbf{r}_1, \mathbf{r}_2, \dots, t) \quad (1.1)$$

This partial differential equation is known as the time-dependent Schrödinger equation and the function Ψ is called the wave function. In the previous equation, $\mathbf{r}_1, \mathbf{r}_2, \dots$ are the spatial coordinates of particles 1, 2, ... and \mathbf{H} is the Hamiltonian operator which is commonly expressed as the sum of operators corresponding to the kinetic \mathbf{K} and \mathbf{V} potential energies of a system.

$$\mathbf{H} = \mathbf{K} + \mathbf{V} \quad (1.2)$$

If the potential energy operator \mathbf{V} is independent of time, equation (1.1) can be separated into equations for the time and spatial variations of the wave function

$$\mathbf{H}\psi(\mathbf{r}_1, \mathbf{r}_2, \dots) = E\psi(\mathbf{r}_1, \mathbf{r}_2, \dots) \quad (1.3)$$

$$i\hbar \frac{d}{dt} \theta(t) = E\theta(t) \quad (1.4)$$

with $\Psi(\mathbf{r}_1, \mathbf{r}_2, \dots, t) = \psi(\mathbf{r}_1, \mathbf{r}_2, \dots)\theta(t)$ and E is the total energy of the system. Equation (1.3) is the time-independent Schrödinger equation. Hereafter, when we mention the Schrödinger equation, we refer to time-independent equation.

Exact solutions of the Schrödinger equation are only possible for simple systems such as the hydrogen atom. Therefore certain approximations must be done in order to find the solutions of equation (1.3) for complex systems. As an example, let us consider the case of a system formed by M nuclei and N electrons. For this system the non relativistic Hamiltonian¹ operator is

$$\begin{aligned} \mathbf{H} = & - \sum_k^M \frac{\hbar^2}{2m_k} \nabla_k^2 - \sum_i^N \frac{\hbar^2}{2m_e} \nabla_i^2 + \sum_i^N \sum_{j>i}^N \frac{e^2}{|\mathbf{r}_i - \mathbf{r}_j|} \\ & - \sum_k^M \sum_i^N \frac{Z_k e^2}{|\mathbf{R}_k - \mathbf{r}_i|} + \sum_k^M \sum_{l>k}^M \frac{Z_k Z_l e^2}{|\mathbf{R}_k - \mathbf{R}_l|} \end{aligned} \quad (1.5)$$

where the \mathbf{R}_k and \mathbf{r}_i are the vector position of nuclei and electrons respectively, m_k and m_e their respective masses. ∇_i^2 and ∇_k^2 are Laplacian operators which involve differentiation over the electrons and nuclei coordinates respectively. The Hamiltonian in equation (1.5) contains pairwise attraction and repulsion terms implying that no particle is moving independently of all the other. This interdependency which is called correlation, is the main reason why exact solutions of the Schrödinger equation are difficult to obtain. In order to simplify the problem, we invoke the Born-Oppenheimer approximation.

¹Additional terms may appear in the Hamiltonian when relativity or interactions with electromagnetic radiation fields are taken into account.

1.1.1 Born-Oppenheimer approximation

The Born-Oppenheimer (BO) approximation assumes that the motion of atomic nuclei and electrons in a molecule can be separated. The foundation of this approximation resides in the fact that as electron are lighter than the nuclei, thus they move faster. Hence, to a good approximation, one can consider the nuclei at a fixed position while the electrons are moving. Classically speaking, during the time of a cycle of electronic motion, the change in nuclear configuration is negligible. Therefore considering the nuclei as fixed, one can omit the kinetic operator of the nuclei, first term in equation (1.5) and consider constant the repulsion potential between nuclei, last term in equation (1.5). As any constant added to the a Hamiltonian operator only changes the values of the total energy and has no effect on the wave functions, the nuclei repulsion term can be dropped thus obtaining the Schrödinger equation for the electronic motion

$$\mathbf{H}_{\text{elec}}\psi_{\text{elec}}(\mathbf{r}, \mathbf{R}) = \varepsilon_{\text{elec}}(\mathbf{R})\psi_{\text{elec}}(\mathbf{r}, \mathbf{R}) \quad (1.6)$$

with

$$\mathbf{H}_{\text{elec}} = -\sum_i^N \frac{\hbar^2}{2m_e} \nabla_i^2 + \sum_i^N \sum_{j>i}^N \frac{e^2}{|\mathbf{r}_i - \mathbf{r}_j|} - \sum_k^M \sum_i^N \frac{Z_k e^2}{|\mathbf{R}_k - \mathbf{r}_i|} \quad (1.7)$$

and $\mathbf{R} = \{\mathbf{R}_1, \mathbf{R}_2, \dots\}$, $\mathbf{r} = \{\mathbf{r}_1, \mathbf{r}_2, \dots\}$. As can be seen both the electronic wave function ψ_{elec} and the pure electronic energy $\varepsilon_{\text{elec}}$ depend parametrically on the nuclei positions. The electronic contribution to the total energy is then obtained as

$$\varepsilon_{\text{tot}}(\mathbf{R}) = \varepsilon_{\text{elec}}(\mathbf{R}) + \sum_k^M \sum_{l>k}^M \frac{Z_k Z_l e^2}{|\mathbf{R}_k - \mathbf{R}_l|} \quad (1.8)$$

It is time now to consider nuclear motions. According to our picture, the electrons move much faster than the nuclei, thus it is reasonable to think that the nuclei move in an average field of the electrons in which the total energy $\varepsilon_{\text{tot}}(\mathbf{R})$ provides a potential for the nuclear motion. Hence the Schrödinger equation for the nuclear motion is

$$\mathbf{H}_{\text{nuc}}\psi_{\text{nuc}}(\mathbf{R}) = E\psi_{\text{nuc}}(\mathbf{R}) \quad (1.9)$$

where

$$\mathbf{H}_{\text{nuc}} = -\sum_k^M \frac{\hbar^2}{2m_k} \nabla_k^2 + \varepsilon_{\text{tot}}(\mathbf{R}) \quad (1.10)$$

and E is the total energy of the system that includes electronic, vibrational, rotational and translational energy. The nuclear wave function ψ_{nuc} describes the vibration, rotation, and translation of the system. Reached this point, we can introduce the concept of potential energy surface (PES): a PES is a surface defined by ε_{tot} over all nuclear coordinates on which the nuclei evolve.

Briefly, within the BO approximation the problem of finding the solution to the

Schrödinger equation is twofold. First, one solves the electronic equation for a grid of different nuclei orientations, thus obtaining the PES. Second, the nuclear equation is solved using the PES obtained in the previous step. Finally, the total wave function is

$$\psi(\mathbf{r}, \mathbf{R}) = \psi_{\text{elec}}(\mathbf{r}, \mathbf{R})\psi_{\text{nuc}}(\mathbf{R}) \quad (1.11)$$

Having introduced the BO approximation, we proceed to describe the methods used to solve both electronic and nuclear Schrödinger equations.

1.2 Electronic structure calculation

Nowadays with the increasing development of computational quantum chemistry, there are a great number of approximate methods which can be employed to solve the electronic Schrödinger equation. Most of these methods are implemented in commercial packages such as MOLPRO [34]. In the following subsection we will briefly describe the methods used in this work.

1.2.1 Hartree-Fock method

The Hartree-Fock (HF) method is one of the simplest approaches for solving the electronic Schrödinger equation. It is based on a simple approximation in which the electronic wave function is given by a single Slater determinant of N spin-orbitals χ_i

$$\psi^0(\mathbf{x}_1, \mathbf{x}_2, \dots, \mathbf{x}_N) = \frac{1}{\sqrt{N!}} \begin{vmatrix} \chi_1(\mathbf{x}_1) & \chi_1(\mathbf{x}_2) & \dots & \chi_1(\mathbf{x}_N) \\ \chi_2(\mathbf{x}_1) & \chi_2(\mathbf{x}_2) & \dots & \chi_2(\mathbf{x}_N) \\ \vdots & \vdots & \ddots & \vdots \\ \chi_N(\mathbf{x}_1) & \chi_N(\mathbf{x}_2) & \dots & \chi_N(\mathbf{x}_N) \end{vmatrix} \quad (1.12)$$

where the variables \mathbf{x} include both coordinates of space and spin.

By minimizing the electronic energy with respect to the choice of the spin-orbitals, one can obtain the HF equations.

$$f(i)\chi_i = \epsilon_i\chi_i \quad (1.13)$$

where $f(i)$ is an effective mono-electron operator, called the Fock operator

$$f(i) = -\frac{1}{2}\nabla_i^2 - \sum_k^M \frac{Z_k}{|\mathbf{r}_i - \mathbf{R}_k|} + v^{\text{HF}}(i) \quad (1.14)$$

The term $v^{\text{HF}}(i)$ is the average potential experienced by the i th electron due to the presence of the other electrons. In essence, the HF approximation replaces the many electron problem by a one-electron problem in which the electron-electron repulsion is treated in an average way. Since the HF potential $v^{\text{HF}}(i)$ depends on the spin-orbitals of the other electrons, equation (1.13) is not linear and must be solved iteratively. This iterative procedure is called the self-consistent field method.

The accuracy of a HF calculation will depend on a great extent on the size of the basis set used to expand the spin-orbitals but even for an infinite basis set there will be a difference between HF limit and the exact energy. This difference is called correlation energy and arise from the fact that the HF approximation does not include electron correlation. Usually the correlation energy represents 1% of the total energy. On an absolute basis this is not much, but for the study of chemical processes it is too large. There are many methods which take into account the electronic correlation. In the following subsections, we briefly describe those that were employed in the present study.

1.2.2 Multi-configurational self-consistent field method

The most straightforward way to include electron correlation in electronic structure calculations is to use more than one Slater determinant in the description of the electronic wave function. Following this concept, in the multi-configurational self-consistent field (MCSCF) method, one writes the wave function as a linear combination of Slater determinants $|\Psi_i\rangle$:

$$\psi_{\text{elec}} = \sum_i c_i |\Psi_i\rangle \quad (1.15)$$

Note that the HF and the MCSCF methods become identical for a closed-shell system in which only one determinant is included in the expansion (1.15). The major difficulty in the MCSCF is to choose which determinant should be included in the expansion (1.15). The most commonly used approach is the complete active space self-consistent field (CASSCF). In CASSCF, the determinants are selected as all possible ones that can be formed within a given set of "active" orbitals. Finally the coefficients c_i and the spin-orbitals contained in $|\Psi_i\rangle$ are varied to obtain the total electronic wave function with the lowest possible energy.

1.2.3 Coupled cluster methods

Coupled cluster methods were initially developed for the treatment of many body quantum systems in nuclear physics in the 1950s, but became more frequently used after Čížek and Paldus [35, 36] reformulated the method for electron correlation in atoms and molecules. Nowadays, coupled cluster methods are some of the most powerful quantum chemistry methods that include electronic correlation.

The electronic wave function of the coupled cluster theory is written as:

$$\psi_{\text{elec}} = e^T |\Psi_0\rangle \quad (1.16)$$

where $|\Psi_0\rangle$ is a reference wave function (typically a Slater determinant constructed from HF molecular orbitals). The operator e^T is defined by the Taylor series expansion

sion:

$$e^{\mathbf{T}} = \mathbf{1} + \mathbf{T} + \frac{\mathbf{T}^2}{2!} + \frac{\mathbf{T}^3}{3!} + \cdots = \sum_{k=0}^{\infty} \frac{\mathbf{T}^k}{k!} \quad (1.17)$$

and \mathbf{T} is the cluster operator which is written in the form,

$$\mathbf{T} = \mathbf{T}_1 + \mathbf{T}_2 + \mathbf{T}_3 + \cdots + \mathbf{T}_N, \quad (1.18)$$

where \mathbf{T}_1 is the operator of all single excitations, \mathbf{T}_2 is the operator of all double excitations and so forth. The \mathbf{T}_i operator acting on the reference wave function generates a linear combination of i -tuple excited Slater determinants. For example in the case of the single and double excitation operator we have

$$\mathbf{T}_1|\Psi_0\rangle = \sum_a \sum_i t_a^i |\Psi_a^i\rangle \quad (1.19)$$

$$\mathbf{T}_2|\Psi_0\rangle = \sum_{ab} \sum_{ij} t_{ab}^{ij} |\Psi_{ab}^{ij}\rangle \quad (1.20)$$

where $|\Psi_a^i\rangle$ and $|\Psi_{ab}^{ij}\rangle$ are respectively single and double excited Slater determinants. The coefficient t_a^i and t_{ab}^{ij} are called, respectively, single- and double-excitation amplitudes.

To apply the coupled cluster method, two approximations are made. First, instead of using a complete set of basis functions, one uses a finite basis set to express the spin-orbitals in the reference wave function $|\Psi_0\rangle$. Second, instead of including all the operators $\mathbf{T}_1, \mathbf{T}_2, \dots, \mathbf{T}_N$ one approximates the operator \mathbf{T} by including only some of these operators. The terms included in the expansion (1.18) determine the name of the coupled cluster method. For example in the CCSD(T) method, the excitation operator has the form $\mathbf{T} = \mathbf{T}_1 + \mathbf{T}_2$. Terms in round brackets indicate that the contribution of triple excitations is calculated with the perturbation theory.

The aim of a coupled cluster calculation is to find the excitation amplitudes which are obtained by solving the set of simultaneous nonlinear equations arising from the substitution of equations (1.16) in the electronic Schrödinger equation. Once the excitation amplitudes are known, the wave function and the energy can be determined.

Coupled cluster methods, like many other ab-initio methods, show an extremely slow basis set convergence of the correlation energy. The origin of this slow convergence is due to the use of Slater determinants to construct two-electron and higher-rank basis sets. Slater determinants fail to model the exact wave functions at short inter-electronic distances. To solve this problem, one can use the explicitly correlated methods (–F12) in which the wave function is modeled explicitly in terms of the inter-electronic distances.

1.2.4 Basis sets

In all the methods presented above, the spin-orbitals are represented as a linear combination of atomic orbitals (LCAO):

$$\chi_i = \sum_j^n c_{ij} \phi_j \quad (1.21)$$

where the set of n functions $\{\phi_i\}$ is known as basis set. The basis functions $\{\phi_i\}$ are commonly represented using either Slater type orbitals (STOs) or Gaussian type orbitals (GTOs). Each orbital type has their own advantages and disadvantages. For example, STOs are physically the best choice as they are solutions to the Schrödinger equation of hydrogen-like atoms, and decay exponentially far away from the nucleus. However, calculations of integrals over STO functions require long computational time. GTOs, on the other hand, lack physical meaning but are computationally tractable.

Nowadays, there are hundreds of basis sets. Some of the most widely used basis sets are the augmented correlation consistent polarized valence N -tuple zeta (aug-cc-pVNZ with $N = D, T, Q, 5, 6$) developed by Dunning et al. [37–41]. These GTO basis sets have become the current state-of-the-art for correlated calculations since they are designed to converge systematically to the complete basis set limit using empirical extrapolation techniques.

1.3 Quantum nuclear motions

Having discussed the methods to solve the electronic problem, we are in condition to introduce the methods for solving the nuclear Schrödinger equation. Specifically, the methods presented here focus on finding the bound and scattering states for the interaction between: (i)–an atom and a linear rigid rotor, (ii)–two linear rigid rotors. The first step in any formulation is to choose the reference coordinate frame. Throughout this monograph, unless specified, the reference coordinate frame is the space-fixed coordinate frame. For the systems under consideration the nuclear Hamiltonian, equation (1.10), can be written as :

$$\mathbf{H} = -\frac{\hbar^2}{2\mu} \left(\frac{1}{R} \frac{\partial^2}{\partial R^2} R \right) + \mathbf{H}_{\text{rot}}(\vartheta) + \mathbf{V}(R, \vartheta) \quad (1.22)$$

where μ is the reduced mass, R is the intermolecular distance and ϑ stands for all the other coordinates. $\mathbf{H}_{\text{rot}}(\vartheta)$ represents the sum of the rigid-rotor Hamiltonians of the isolated moieties and $\mathbf{V}(R, \vartheta)$ is an interaction potential which includes the centrifugal barrier.

1.3.1 Coupled channel method

The coupled channel method has been widely applied to the study of inelastic collision but is also applicable to vibrational-rotational levels of floppy molecules such as van der Waals complexes. In the coupled channel approach the wave function for the i th state is expanded as:

$$\Psi^{(i)}(\mathbf{R}, \vartheta) = \mathbf{R}^{-1} \sum_j \mathcal{Y}_j(\vartheta) G_j^{(i)}(\mathbf{R}) \quad (1.23)$$

where the functions $\mathcal{Y}_j(\vartheta)$ are eigenvectors of the internal Hamiltonian $\mathbf{H}_{\text{rot}}(\vartheta)$

$$\mathbf{H}_{\text{rot}} \mathcal{Y}_j = \epsilon_j \mathcal{Y}_j \quad (1.24)$$

Substituting the equations (1.22) and (1.23) into equation (1.9) and projecting onto a basis function $\mathcal{Y}_k(\vartheta)$, one obtains the following second-order differential equation for the channel function $G_k^{(i)}(\mathbf{R})$:

$$\frac{d^2}{d\mathbf{R}^2} G_k^{(i)}(\mathbf{R}) = \sum_j W_{jk}(\mathbf{R}) G_j^{(i)}(\mathbf{R}) \quad (1.25)$$

where

$$W_{jk}(\mathbf{R}) = \frac{2\mu}{\hbar^2} \int \mathcal{Y}_k^*(\vartheta) \mathbf{V}(\mathbf{R}, \vartheta) \mathcal{Y}_j(\vartheta) d\vartheta - \delta_{jk} \kappa_j^2 \quad (1.26)$$

with

$$\kappa_j^2 = \frac{2\mu}{\hbar^2} (E - \epsilon_j) \quad (1.27)$$

Similar equations arise for each channel and are coupled by the non-diagonal term $W_{jk}(\mathbf{R})$. The choice of the functions $\mathcal{Y}_j(\vartheta)$, the form of the term $W_{jk}(\mathbf{R})$ as well as the boundary conditions depend on the system under consideration. Therefore, they will be presented in chapters 5 and 7. The complete set of coupled equations is infinite, but it is necessary to truncate the basis set to perform actual computations. Calculations that use an exact formulation, with no approximation other than basis set truncation, are usually referred to as close coupling (CC) calculations. The resulting set of coupled one-dimensional second-order differential equations can be solved using standard numerical methods such as the R-matrix propagator [42] or the log-derivative propagator [43].

1.3.2 Variational approach

The variational approach is one of the most employed methods for finding the energy levels of weakly bounded van der Waals complexes. This approach is based on the variational principle which states that given a normalized wave function Ψ that satisfies the appropriated boundary conditions (usually $\Psi|_{\mathbf{R} \rightarrow \infty} = 0$), then the expectation value of the Hamiltonian is an upper bound to the exact energy

$$\int \Psi^* \mathbf{H} \Psi d\tau \geq E \quad (1.28)$$

For the systems under consideration, the unknown solution can be represented exactly in a complete set of orthogonal functions.

$$\Psi(\mathbf{R}, \vartheta) = \mathbf{R}^{-1} \sum_{jk}^{\infty} c_{jk} \mathcal{Y}_j(\vartheta) G_k(\mathbf{R}) \quad (1.29)$$

where the functions \mathcal{Y}_j satisfies equation (1.24) and G_k are usually a set of orthonormal \mathcal{L}^2 polynomials that satisfy the following equation:

$$-\frac{\hbar^2}{2\mu} \frac{d^2}{dR^2} G_k = \eta_k G_k \quad (1.30)$$

In practice, expansion (1.29) is truncated to a finite number of terms. This truncated representation is often called variational basis representation (VBR) [44–46]. The name "variational" applies because the expectation values of the Hamiltonian are larger than or equal to the corresponding exact energy (variational principle).

The coefficients c_{jk} are obtained by minimizing the variational integral (1.28) with the constraint that the wave function (1.29) must be orthonormal. The problem of minimizing a function subject to a constraint is solved by the method of Lagrange multipliers. This problem comes down to find the minimum values of the trial function

$$\mathcal{L}(c_{11}, c_{12}, \dots, c_{nm}, \lambda) = \sum_{jj'}^n \sum_{kk'}^m c_{jk} c_{j'k'} H_{jk,j'k'} + \lambda \left(\sum_j^n \sum_k^m c_{jk}^2 - 1 \right) \quad (1.31)$$

where

$$\begin{aligned} H_{jk,j'k'} &= \iint G_{k'}^*(\mathbf{R}) \mathcal{Y}_{j'}^*(\vartheta) \mathbf{H} \mathcal{Y}_j(\vartheta) G_k(\mathbf{R}) d\mathbf{R} d\vartheta \\ &= (\epsilon_j + \eta_k) \delta_{jj'} \delta_{kk'} + \int G_{k'}^*(\mathbf{R}) W_{jj'}(\mathbf{R}) G_k(\mathbf{R}) d\mathbf{R} \end{aligned} \quad (1.32)$$

Differentiating equation (1.31) with respect to $c_{j'k'}$ and setting the result equal to zero, one obtains a set of linear equations for the coefficients c_{jk} ,

$$\frac{\partial \mathcal{L}}{\partial c_{j'k'}} = 2 \sum_j^n \sum_k^m c_{jk} H_{jk,j'k'} + 2\lambda c_{j'k'} = 0 \quad (1.33)$$

This set of equations can be written in a matrix notation as

$$\mathbb{H} \mathbf{c} = \lambda \mathbf{c} \quad (1.34)$$

Finally, the expansion coefficients are nothing less than the eigenvector of the matrix \mathbb{H} . Solutions to equation (1.34) lead to a set of $(n \cdot m)$ orthonormal eigenvector $\mathbf{c}^{(i)}$ and eigenvalues $\lambda^{(i)}$ which for convenience are arranged as $\lambda^{(0)} < \lambda^{(1)} < \dots < \lambda^{(n \cdot m)}$.

Therefore, instead of finding just one solution for Ψ , we have found $(n \cdot m)$ solutions for which the expectation values of the Hamiltonian are $\lambda^{(i)}$. Furthermore, from the variational principle we obtain $E_i \leq \lambda^{(i)}$. Thus, the eigenvalues of \mathbb{H} provide upper bounds to the energies of the lowest bound states of the system and as $n, m \rightarrow \infty$, then $\lambda^{(i)} \rightarrow E_i$. The number of basis functions should then be increased

systematically until the calculation converges, i.e. until the quantities $\lambda^{(i)}$ become stationary.

The major difficulty in the VBR is the calculation of the matrix elements of the interaction potential

$$V_{jk,j'k'} = \int G'_k(\mathbf{R})W_{jj'}(\mathbf{R})G_k(\mathbf{R})d\mathbf{R} \quad (1.35)$$

For very simple systems, this integral can be done analytically. However, if the potential function is complicated, this integration must be done numerically, introducing a possible source of inaccuracy into the calculation. The approximation to the VBR in which matrix elements of the potential energy operator are evaluated by an m -point quadrature rule associated to the polynomial $\{G_k\}_m$ is called finite basis representation (FBR) [44–46].

$$V_{jk,j'k'}^{\text{FBR}} = \sum_{\alpha}^m G'_k(\mathbf{R}_{\alpha})W_{jj'}(\mathbf{R}_{\alpha})G_k(\mathbf{R}_{\alpha})\omega_{\alpha} \quad (1.36)$$

where ω_{α} is the quadrature weight associated with the α th grid point \mathbf{R}_{α} . The FBR can be transformed to a new representation $\{D_{\alpha}\}_m$ in which the basis functions are orthogonal on a set of points in the coordinate space. The points are usually obtained from a quadrature rule. Each function is worth 1 for one point and zero for all other points. This representation is called discrete variable representation (DVR). The transformation between the FBR and DVR basis sets is given by the matrix \mathbb{L}^{\dagger} defined as

$$L_{k\alpha}^{\dagger} = \omega_{\alpha}^{1/2}G_k(\mathbf{R}_{\alpha}) \quad (1.37)$$

The basis functions of the DVR are then

$$D_{\alpha}(\mathbf{R}) = \sum_k^m L_{k\alpha}^{\dagger}G_k(\mathbf{R}) \quad (1.38)$$

In the DVR, the matrix elements of the interaction potential are given by the potential evaluated at the set of quadrature points

$$V_{j\alpha,j'\beta}^{\text{DVR}} = W_{jj'}(\mathbf{R}_{\alpha})\delta_{\alpha\beta} \quad (1.39)$$

If the FBR basis functions are selected such that the FBR representation of the kinetic operator is easily evaluated, possibly diagonal, then the use of the FBR–DVR becomes highly advantageous. The transformation between the FBR and DVR matrix elements of the potential is obtained from equations (1.36) and (1.37):

$$V_{jk,j'k'}^{\text{FBR}} = \sum_{\alpha\beta}^n L_{k\alpha}^{\dagger}V_{\alpha\beta}L_{\beta k'} = (\mathbb{L}^{\dagger}\mathbb{V}^{\text{DVR}}\mathbb{L})_{jk,j'k'} \quad (1.40)$$

Consequently the matrix element of the Hamiltonian in the DVR are

$$\begin{aligned} H_{j\alpha,j'\beta}^{\text{DVR}} &= (\mathbb{L}H^{\text{FBR}}\mathbb{L}^{\dagger})_{j\alpha,j'\beta} \\ &= \sum_k \eta_k G_k(\mathbf{R}_{\alpha})(\omega_{\alpha}\omega_{\beta})^{1/2}G_k(\mathbf{R}_{\beta}) + \epsilon_j \delta_{\alpha\beta} \delta_{jj'} + W_{j\alpha,j'\beta}(\mathbf{R}_{\alpha})\delta_{\alpha\beta} \end{aligned} \quad (1.41)$$

which are more easily computed than the VBR matrix elements given by equation (1.32).

Chapter 2

A single center approach to REA and PD

Contents

2.1	Introduction	20
2.2	Theory	21
2.2.1	REA and PD cross sections	21
2.2.2	Calculation of the Dyson orbital	22
2.2.3	Calculation of the electron continuum wave function	23
2.3	Parameters of the calculations	26
2.3.1	Dyson orbital	26
2.3.2	Continuum wave function	27
2.3.3	Spin and electronic degeneracies	28
2.4	Comparison between theory and experiment	28
2.4.1	Comparison of the methods and basis sets for the Dyson orbital evaluations	32
2.5	Conclusion	34

Submitted

M. Lara-Moreno, T. Stoecklin, P. Halvick, and J.-C. Loison. New single-center approach of photodetachment and radiative electron attachment: Comparison with other theoretical approaches and with experimental photodetachment data. J. Chem. Phys., 2018

2.1 Introduction

As suggested by Herbst [2] long ago, REA is expected to be the main production channel of anions for environments where the density of electron is relatively important (10^{-7} the density of H_2). On the experimental side, measurements of REA cross sections are scarce due to the difficulties of measuring these very low magnitude cross sections. Conversely, PD is the subject of many studies. Also, experimental data are available for this process for several diatomic molecular anions which can be used to benchmark our theoretical results by using micro-reversibility.

On the theoretical side, the first methods which apply equivalently to REA and PD were proposed in the seventies [48] and were based on the use of the first Born approximation (FBA). This approach relies on the fact that for non-polar systems the long-range interaction between the outgoing or incoming electron and the neutral molecule is negligible, thus allowing the use of a plane wave for describing the continuum wave function of the departing electron. Within this one-electron approach, the wave function of the departing electron inside the anion is considered to be the highest occupied molecular orbital (HOMO). This approach was revised more recently by several authors who improved this treatment by taking into account the correlation with the electrons of the target through the use of Dyson orbital calculated at the CCSD(T) level [49] or from density functional theory (DFT) [50]. The use of a calculated continuum electron wave function instead of a plane wave was also considered very early in the field of molecular photoionization by Collins and Schneider [51] but its first use for PD was proposed in 2013 by Douguet et al. [26] within the complex-Kohn variational formalism. We use here a very similar approach but instead we use the integral equation formalism [52, 53] to obtain the scattered electron wave function. Before ending this introduction we would like also to mention a novel Sturmian approach which has been recently developed by Granados-Castro et al. [54] and satisfactory applies to photoionization, and could be potentially extended to PD.

The chapter is organized as follows. In section 2.2 we introduce the main steps of the scattering methods as well as the description of the calculation of the Dyson orbitals. The parameters of the different calculations are given in section 2.3 and a first test of the method for the calculation of the PD of O_2^- , CN^- and OH^- are presented in section 2.4 where a comparison is done with the available experimental data and with other theoretical results, e.g. Kohn variational and R-matrix methods. In the second part of this section, the FBA is used to discuss the convergence of the REA and PD cross sections as a function of the size and type of basis set as well as the different approximations for the calculation of the Dyson orbital. The conclusions of the present study are eventually presented in section 2.5.

2.2 Theory

In this section, we give a brief account of the method which allows us to obtain the REA and PD cross sections for linear molecules. The same method can be straightforwardly extended to treat non-linear molecules as well. This method relies on a single center body-fixed expansion of the bound and continuum wave around the center of mass of the molecule.

For a given value of the initial relative angular momentum l_0 and its projection Λ along the molecular axis one writes the scattered electron wave function like:

$$\psi_{\Lambda l_0}^{\text{Scat}}(\mathbf{r}) = \frac{1}{r} \sum_l \gamma_{\Lambda l_0, l}^{\text{Scat}}(\mathbf{r}) Y_l^\Lambda(\hat{\mathbf{r}}) \quad (2.1)$$

In a similar way the one-electron wave function of the anion is taken to be a Dyson orbital also expanded in spherical harmonics:

$$\psi_{\Lambda'}^{\text{Dyson}}(\mathbf{r}) = \frac{1}{r} \sum_{l'} \gamma_{\Lambda', l'}^{\text{Dyson}}(\mathbf{r}) Y_{l'}^{\Lambda'}(\hat{\mathbf{r}}) \quad (2.2)$$

where Λ' is the projection of the electronic angular momentum l' of the anion along its molecular axis.

2.2.1 Radiative electron attachment and photodetachment cross sections

The expressions of the cross section as a function of the dipole moment matrix elements were given long ago for the photoionization of neutral molecules [51] or for the PD [55].

$$\sigma_{\text{PD}}(\omega) = \frac{4\pi^2 e^2 \omega}{9c} \sum_{l_0 \Lambda} \|\mu_{l_0}^{\Lambda \Lambda'}\|^2 \quad (2.3)$$

where

$$\mu_{l_0 \pi}^{\Lambda \Lambda'} = N_0^{\frac{1}{2}} \langle \psi_{\Lambda l_0}^{\text{Scat}} | \mu^\pi | \psi_{\Lambda'}^{\text{Dyson}} \rangle \quad (2.4)$$

are the dipole matrix elements, N_0 is the degeneracy factor (see below subsection 2.3.3), ω is the photon frequency and c the speed of light and μ^π the components of the dipole moment with $\pi \in \{-1, 0, 1\}$. While the same expression is used for both processes PD and photoionization, the departing electron is subjected to potentials which differ strongly in strength and range.

Using equations (2.1) and (2.2), the expression (2.4) can be rewritten :

$$\mu_{l_0 \pi}^{\Lambda \Lambda'} = \sum_{l, l'} I_{\pi l l'}^{\Lambda \Lambda'} \int_0^\infty \gamma_{\Lambda l_0, l}^{\text{Scat}}(\mathbf{r}) r \gamma_{\Lambda', l'}^{\text{Dyson}}(\mathbf{r}) d\mathbf{r} \quad (2.5)$$

with:

$$I_{\pi l l'}^{\Lambda \Lambda'} = (-)^{\Lambda} \sqrt{(2l+1)(2l'+1)} \begin{pmatrix} l & 1 & l' \\ 0 & 0 & 0 \end{pmatrix} \begin{pmatrix} l & 1 & l' \\ -\Lambda & \pi & \Lambda' \end{pmatrix} \quad (2.6)$$

The corresponding equations for the REA cross section are straightforwardly ob-

tained from microscopic reversibility [56, 57]:

$$\sigma_{\text{REA}}(\epsilon) = \left(\frac{g_a}{g_n} \right) \frac{\hbar^2 \omega^2}{2m_e \epsilon c^2} \sigma_{\text{PD}}(\omega) \quad (2.7)$$

where the quantities g_n and g_a are the statistical weights of the electronic states of the neutral molecule and of the anion, respectively, ϵ is the electron kinetic energy and m_e is the electron mass. Let us note that this principle of micro-reversibility should be applied to processes with well-specified internal quantum states (rotational, vibrational, electronic) of the initial and final species. Since in the present work we are not considering the rovibrational states of the anion and of the neutral molecule, the use of equation (2.7) is an approximation.

We will now detail the procedure used for obtaining the radial coefficient of the Dyson $\Upsilon_{\Lambda', l'}^{\text{Dyson}}$ and the scattering $\Upsilon_{\Lambda l_0, l}^{\text{Scat}}$ wave functions.

2.2.2 Calculation of the Dyson orbital

Let us consider a N-electrons molecular system represented by the electronic wave function $\psi^N(\mathbf{r}_1, \mathbf{r}_2, \dots, \mathbf{r}_N)$. After ionization this system has lost one electron and its (N - 1)-electron wave function is represented by $\psi^{N-1}(\mathbf{r}_1, \mathbf{r}_2, \dots, \mathbf{r}_{N-1})$. The Dyson orbital is then defined as:

$$\psi_{\Lambda'}^{\text{Dyson}}(\mathbf{r}) = \sqrt{N} \int \psi^{N-1}(\mathbf{r}_1, \dots, \mathbf{r}_{N-1}) \psi^N(\mathbf{r}_1, \dots, \mathbf{r}_N) d\mathbf{r}_1 \dots d\mathbf{r}_{N-1} \quad (2.8)$$

If ψ^N and ψ^{N-1} are represented by accurate multi-configurational wave functions, then the Dyson orbital gathers the effects of electronic correlation on both systems and therefore the effects of the electronic relaxation which results from the addition or subtraction of one electron in the molecular electronic wave function.

A method for computing the Dyson orbital from MCSCF is detailed in appendix A. It is based on the overlaps between the orbitals of the N-electron system and the orbitals of the (N-1)-electron system. Other ab-initio methods have been reported, using the equation-of-motion coupled-cluster method [58] or the construction of a biorthonormal set of two multi-configurational wave functions [59].

The calculated Dyson orbital is then conveniently represented by an expansion over the molecular orbital set of the N-electron system

$$\psi_{\Lambda'}^{\text{Dyson}}(\mathbf{r}) = \sum_p b_p \phi_p(\mathbf{r}) \quad (2.9)$$

where the index p denotes any occupied orbital.

A simple approximation of the Dyson orbital is given by the Hartree-Fock frozen-core (HFFC) approach [48, 51]. Within this approximation, the HF orbitals of the anion are used to describe those of the remaining neutral core. In that case, the integral (2.8) is easily calculated. The Dyson orbital is just the spatial orbital from which the electron is ejected. This approximation neglects the electronic correlation and the relaxation of the molecular orbitals after PD.

Kohn-Sham (KS) orbitals have been recently proposed as good candidates for approximating the Dyson orbital [50, 60, 61]. Although KS orbitals were introduced as a mere artifact only for calculating the total energy and charge density, the latter proposition is based on the analogies found between the Dyson’s quasi-particle and KS equations.

In any case, the Dyson orbital is represented as a linear combination of either GTOs or STOs. The radial expansion coefficients, equation (2.2), are determined from a set of analytical relations expressed in term of modified Bessel functions [62, 63]. The different basis sets[38, 64] used in this work are detailed in Table 2.1

Table 2.1: Basis set used in the present work

Type	Basis	H	B–Ne
GTO	aug-cc-pVQZ	[5s4p3d2f]	[6s5p4d3f2g]
GTO	aug-cc-pV5Z	[6s5p4d3f2g]	[7s6p5d4f3g2h]
GTO	aug-cc-pV6Z	[7s6p5d4f3g2h]	[8s7p6d5f4g3h2i]
STO	VB2	4s2p1d	6s4p2d1f
STO	VB3	5s3p2d1f	7s5p3d2f1g

All electronic calculation needed for the computation of the Dyson orbital were performed using the MOLPRO package [34] and the SMILES package [65].

2.2.3 Calculation of the electron continuum wave function

2.2.3.1 Scattered wave

In this section we present our adaptation to PD and REA of the integral equations approach developed long ago by Rescigno and Orel [52, 53] for electron–molecule collisions. While only the main steps of the implementation of the method for linear molecules will be presented, more details can be found in the seminal references [52, 53]. First, the electronic wave function of the target is analytically expanded in symmetrized spherical harmonics and the expansion coefficients are employed for obtaining the static interaction potential. More specifically, we will consider here a MCSCF wave function and use the natural orbitals and their occupancies to obtain static contribution. The method also entails obtaining a diagonal separable form of the exchange potential kernel for the lowest symmetries Σ , Π and Δ of the scattered electron wave function in the same atomic orbital basis set than the one used for the Dyson orbital, possibly augmented with a few functions centered around the center of mass,

$$K(r, r') = \sum_{\alpha} \chi_{\alpha}(r) \xi_{\alpha} \chi_{\alpha}(r') \quad (2.10)$$

where ξ_α and $\chi_\alpha(Rr)$ are respectively the eigenvalues and eigenvectors of the exchange kernel in this basis set. If needed, a density functional Hara's free electron gas exchange (HFEGE) [66] is used for higher symmetries. A density functional form of the correlation-polarization potential as introduced by Padial and Norcross [67] is also obtained from the same electronic wave function and included in the local interaction potential.

The scattering wave function is expanded in spherical harmonics. The resulting single center coupled equations take the usual form :

$$\left(\frac{d^2}{dr^2} - \frac{l(l+1)}{r^2} + k^2 \right) \Phi_{l_0}(r) = \sum_{l'\alpha} \left[U_{ll'}(r) \Phi_{l'\alpha}(r) + \chi_\alpha^l(r) \xi_\alpha \int_0^\infty \chi_\alpha^{l'}(r') \Phi_{l'\alpha}(r') dr' \right] \quad (2.11)$$

where, to make the notation less cluttered, the projection Λ of the relative angular momentum associated with the symmetry for which the calculations are performed is not mentioned. In this expression, $U_{ll'}$ denotes the matrix elements of the local contributions to the interaction potential which includes the static and correlation-polarization potentials. The integral form of these equations are solved with the Sams and Kouri [68, 69] method extended by Rescigno and Orel [52, 53] to the multi-channel case with a separable exchange potential.

The radial components of the wave function are expressed as a linear combination of homogeneous and inhomogeneous terms

$$\Upsilon_{\Lambda l_0, l}^{\text{Scat}}(r) \equiv \Phi_{l_0}(r) = \Phi_{l_0}^0(r) + \sum_{\alpha} \Phi_l^\alpha(r) C_{l_0}^\alpha \quad (2.12)$$

which both satisfy a set of Volterra equations given by

$$\Phi_{l_0}^0(r) = \delta_{ll_0} j_l(kr) + \sum_{l'} \int_0^r g_l(r, r') U_{ll'}(r') \Phi_{l_0}^0(r') dr' \quad (2.13)$$

for the homogeneous term and for the inhomogeneous term

$$\Phi_l^\alpha(r) = \int_0^r g_l(r, r') \chi_l^\alpha(r') dr' + \sum_{l'} \int_0^r g_l(r, r') U_{ll'}(r') \Phi_l^\alpha(r') dr' \quad (2.14)$$

The integral-equations algorithm is very efficient but requires the use of two kinds of well documented stabilization methods [53] corresponding to a change of the initial conditions. The upper triangular stabilization entails decomposing the homogeneous solution, at some given propagation distance, into the product of the upper and lower triangular matrices. The solution matrix is replaced by the resulting upper triangular matrix whose columns are guaranteed to be linearly independent. The second kind of stabilization, referred to as *physical* by Rescigno and Orel [53], is designed to make the solution matrix resemble the physical solution as much as possible. In both cases, the stabilization of the homogeneous part of the solution

can be written in term of a transformation matrix \mathbb{T} such that

$$\Phi_{l_0}^0 \rightarrow \tilde{\Phi}_{l_0}^0 = \sum_k \Phi_{l_k}^0 T_{kl_0} \quad (2.15)$$

For the same value of the propagation distance, an associated stabilization of the non-homogeneous part of the scattering wave function needs also to be performed. For both kinds of stabilization, the non-homogeneous part of the scattering wave function can be written in terms of a transformation matrix \mathfrak{d} and the stabilized homogeneous part of the wave function:

$$\Phi_l^\alpha \rightarrow \tilde{\Phi}_l^\alpha = \Phi_l^\alpha + \sum_{l''} \tilde{\Phi}_{l''}^0 \mathfrak{d}_{l''l}^\alpha \quad (2.16)$$

The wave function is then propagated outwardly and stabilized regularly up to the asymptotic region where the boundary conditions are applied and the reactance matrix is obtained.

If we now apply this method to directly propagate the dipole moment matrix elements defined in equation (2.4), we see that the two terms of the electron continuum wave function (2.12) must be taken into account. Thus, the dipole moment matrix elements can be split into two contributions associated with the local and non-local parts of the interaction potential which are respectively denoted by static and exchange:

$$\mu_{l_0\pi}^{\wedge\wedge'} = [\mu_{l_0\pi}^{\wedge\wedge'}]_{\text{Stat}} + [\mu_{l_0\pi}^{\wedge\wedge'}]_{\text{Exc}} \quad (2.17)$$

The static contribution is

$$[\mu_{l_0\pi}^{\wedge\wedge'}]_{\text{Stat}} = \sum_{l,l'} I_{\pi ll'}^{\wedge\wedge'} \int_0^\infty \Phi_{l_0}^0(r) r \gamma_{\wedge',l'}^{\text{Dyson}}(r) dr \quad (2.18)$$

and the exchange contribution is

$$[\mu_{l_0\pi}^{\wedge\wedge'}]_{\text{Exc}} = \sum_\alpha C_{l_0}^\alpha M_{\alpha\pi}^{\wedge\wedge'} \quad (2.19)$$

with

$$M_{\alpha\pi}^{\wedge\wedge'} = \sum_{l,l'} I_{\pi ll'}^{\wedge\wedge'} \int_0^\infty \Phi_l^\alpha(r) r \gamma_{\wedge',l'}^{\text{Dyson}}(r) dr \quad (2.20)$$

These two contributions are accumulated along the propagation of the continuum wave function and then need also to be stabilized at the points where the wave function is stabilized.

We obtain straightforwardly from equation (2.15) that the stabilization procedure of the homogeneous part of the dipole matrix is simply given by:

$$[\mu_{l_0\pi}^{\wedge\wedge'}]_{\text{Stat}} \rightarrow [\tilde{\mu}_{l_0\pi}^{\wedge\wedge'}]_{\text{Stat}} = \sum_k T_{kl_0} [\mu_{k\pi}^{\wedge\wedge'}]_{\text{Stat}} \quad (2.21)$$

while using equation (2.16) the corresponding transformation of the exchange part of the dipole matrix is found to be for the intermediary matrix \tilde{M} :

$$M_{\alpha\pi}^{\wedge\wedge'} \rightarrow \tilde{M}_{\alpha\pi}^{\wedge\wedge'} = M_{\alpha\pi}^{\wedge\wedge'} + \sum_{l''} \mathfrak{d}_{l''l}^\alpha [\tilde{\mu}_{l''\pi}^{\wedge\wedge'}]_{\text{Exc}} \quad (2.22)$$

2.2.3.2 Plane wave

We have also applied the FBA to the study of REA and PD processes as it is very simple to use and allows huge computer time saving since neither the electron-molecule interaction potential nor the scattering wave function need to be calculated. Indeed, within the FBA, the electron continuum wave function is just a plane wave and the interaction potential between the electron and the target is then implicitly considered to be zero. This is a reasonable approximation in the case of the interaction between an electron and neutral non-dipolar molecule for which the interaction is relatively short-ranged. The first implementation of the method for the PD from anions was proposed long ago [48]. In this early attempt, the Dyson orbital was approximated by the HOMO of the anion. More recently, new implementations of the method using instead a Dyson orbital calculated by the DFT or coupled-cluster methods were shown to give very good results for several systems[49, 50].

The expansion coefficients in spherical harmonics of the scattering wave function defined in equation (2.1) are easily obtained from

$$\begin{aligned}\psi_{\lambda l_0}^{\text{Scat}}(\mathbf{r}) &= \sqrt{\frac{k}{(2\pi)^3}} e^{i\mathbf{k}\mathbf{r}} \\ &= \sqrt{\frac{k}{(2\pi)^3}} \sum_l i^l j_l(kr) P_l(\cos\theta_{kr})\end{aligned}\quad (2.23)$$

The radial expansion coefficients $\Upsilon_{\lambda l_0, l}^{\text{Scat}}(r)$ of equation (2.1) reduce, in this case, to the Ricatti-Bessel functions.

2.3 Parameters of the calculations

All the calculations are performed using the following assumptions:

- The electron affinities, the ionization energies, the parallel and perpendicular polarizabilities of the neutral molecules are fixed to the values shown in Table 2.2.
- We consider only the contributions from the electronic ground states of both the anion and the neutral molecule to the REA or PD processes.

2.3.1 Dyson orbital

In the case of the HFFC and KS approach, since CN^- and OH^- have a singlet ground state, the Dyson orbital is just the HOMO. For O_2^- which has a $^2\Pi$ ground state with the configuration π^3 , and becomes after PD the O_2 molecule with a $^3\Sigma^-$ ground state and the π^2 configuration, the Dyson orbital is the π orbital occupied by 2 electrons in the ground state of O_2^- .

Table 2.2: Dipole moment (μ), polarizabilities (α), ionization energies (IE) and electron affinities (EA) used in the calculations. Dipole moments and polarizabilities were calculated using the finite field method implemented in MOLPRO at CCSD(T)/aug-cc-pV6Z level.

Molecule	μ (Debye)	α_{\parallel} (a_0^3)	α_{\perp} (a_0^3)	IE (eV)	EA (eV)
O ₂	0	14.11	8.74	12.07[70]	0.4480[71]
CN	1.40	25.13	16.32	14.17[72]	3.8620[73]
OH	1.63	8.62	6.21	13.02[74]	1.8277[75]

Experimental equilibrium bond lengths of the anions are employed in the calculations, namely 2.224, 2.551, 1.833 a_0 for CN⁻ [73], O₂⁻ [76], and OH⁻ [77], respectively. The maximum value of l' for the expansion of the Dyson orbital in spherical harmonics, equation (2.2), is fixed to 35, 34 and 25 for CN⁻, O₂⁻ and OH⁻, respectively.

2.3.2 Continuum wave function

2.3.2.1 Scattered wave

In order to solve the integro-differential equation detailed in section 2.2.3 we need first to obtain the static, correlation polarization and exchange potential.

Static potential. The fundamental electronic wave functions of the CN, O₂ and OH molecules are described at the CASSCF level with full valence active space and using the basis set shown in Table 2.1 and the experimental geometries. A total of 150 values of l are included in the analytical expansions of the natural orbitals in spherical harmonics. We then use this expansion together with the natural orbital populations to obtain the 80 first terms of the static potential multipole expansion.

Correlation-polarization potential. We use the local density functional form of Padial and Norcross [67] and the polarizabilities given in Table 2.2 to obtain the $l = 0$ and $l = 2$ contributions included in our calculations.

Exchange potential. First, the local density functional HFEGE [66] is calculated for a maximum values of $l = 40$ and using the ionization energies given in Table 2.2. Secondly, a non-local separable form [52] is computed for the Σ and Π symmetries in the GTO basis set used to calculate the electronic wave functions. The maximum value of l considered for the expansion in GTO functions is 80 for the three systems. For the Δ symmetry, a HFEGE potential is used as it was shown to give equivalent results.

2.3.2.2 Plane wave

In all calculations the partial wave expansion of a plane wave, equation (2.23), was truncated at a maximum value of 40 Riccati-Bessel functions for the three systems.

2.3.3 Spin and electronic degeneracies

In the case of PD or photoionization of a closed-shell system with no electronic degeneracy, the calculated cross section must be multiplied by 2 [51, 78, 79]. This arises from the fact that the final state combines two electrons in two different orbitals and must be a singlet state. The spin of the electron ejected from the initial closed-shell system can be up or down. Both spin projections lead to the same cross section and we have to sum over these two cases. This applies to the PD of $\text{CN}^- (X^1\Sigma^+)$ giving $\text{CN}(X^2\Sigma^+)$. Let us now consider the PD from $\text{OH}^- (X^1\Sigma^+)$. The HOMO is a π orbital occupied by 4 electrons. The final state is $\text{OH}(X^2\Pi)$ with the π orbital occupied by 3 electrons. The ejected electron can be any of the 4 initial electrons occupying the HOMO. The total PD cross section is then the sum of the four equivalent cross sections calculated by considering only one electron among the four available ones. Thus we multiply the calculated cross section by 4. Finally, let us turn to the PD from $\text{O}_2^- (X^2\Pi)$ which has a π HOMO occupied by 3 electrons. We consider only the final state $\text{O}_2(X^3\Sigma_g^-)$. The final π HOMO is occupied by 2 electrons and must be a triplet state. This requires two open shells. Let us denote by π_x and π_y the two degenerate orbitals which form the π orbital. The initial state has two electrons in the π_x or π_y orbital and one electron in the other degenerate orbital. The final state must have one electron in each π_x and π_y orbitals. Therefore there is only the possibility to eject an electron from the doubly occupied orbital. This case reduces to the case of a closed-shell system with no electronic degeneracy and therefore, we multiply the calculated cross section by 2. Furthermore we have to average the cross section over all initial states. The two initial degenerate states of $\text{O}_2^- (X^2\Pi)$ are equivalent (2 electrons in π_x and 1 in π_y or the reverse). Therefore the cross section of only one case needs to be calculated.

2.4 Comparison between theory and experiment

In this section we first test our theoretical approaches by comparing our results for the PD cross sections with the experimental data available for O_2^- , OH^- and CN^- respectively in Figure 2.1, 2.2 and 2.3. In these calculations, the Dyson orbital as well as the different contributions to the interaction potential were calculated at the CASSCF level using the VB3 basis set.

For O_2^- we see in Figure 2.1 that there is a global good agreement between theory and experiment whatever the theoretical method used. The relatively good agreement between the scattered wave and plane wave calculations was expected as O_2 has no dipole and the interaction potential between the ejected electron and O_2 is driven by the charge quadrupole ($\propto r^{-3}$) and charge-induced dipole ($\propto r^{-4}$) contributions which are not very strong. Thus the continuum wave function is well

described by a plane wave for this system. The present PD cross section obtained using the FBA is in very good agreement with the cross section reported by Oana and Krylov [49]. Although both calculations use a plane wave to describe the electron continuum wave, they employ different basis sets and methods for the calculation of the Dyson orbital. The PD cross section of O_2^- is, however, rather insensitive to the basis set, as shown below in section 2.4.1. Furthermore, due to symmetry, the Dyson orbital is essentially the π_g orbital with a small contribution from the π_g^* orbital, therefore reducing the discrepancy which could come from the different methods of calculating the Dyson orbital.

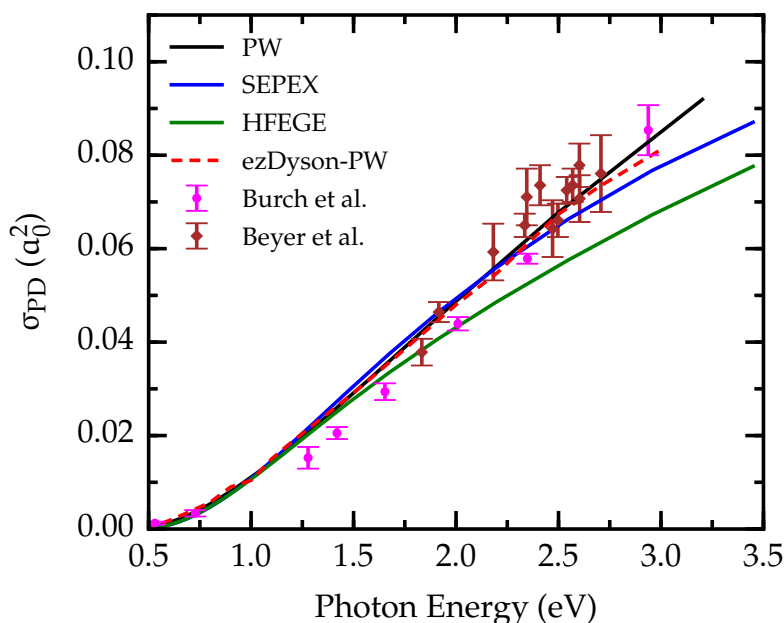


Figure 2.1: Experimental [80, 81] and calculated PD cross section of O_2^- . The calculated cross sections correspond to different descriptions of the electron continuum wave function: plane wave (PW), scattered wave using a separable exchange potential (SEPEX), scattered wave using a HFEGE potential. The red dashed line depicts the cross section obtained by Oana and Krylov [49] using the FBA.

In the case of OH^- represented in Figure 2.2, four sets of experimental data are available which agree only for the lowest photon energies. At higher energy it becomes difficult to decide which set of experimental data is the most reliable. But let us note that the experimental work of Branscomb [77] is the oldest one (1966) and gives the largest cross section while the work of Lee and Smith [82] is more recent (1979) and is in good agreement with the most recent works of Hlavenka et al. [84](2009).

Near the PD threshold, the three sets of calculations describe reasonably well the increase of the cross section. At higher energies, a large discrepancy is observed between the cross section calculated using a plane wave and the other two calcu-

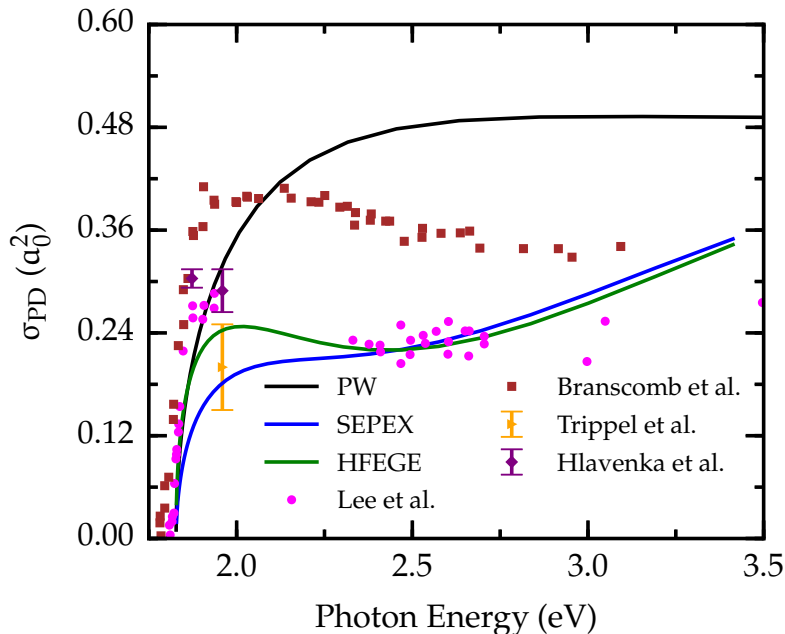


Figure 2.2: Experimental [77, 82–84] and calculated PD cross section of OH^- . Notation as in Figure 2.1.

lated using the scattered wave function. This can be understood by reminding that OH is a strongly dipolar molecule and that consequently the interaction potential of this molecule with the ejected electron cannot be neglected. While the agreement between theory and experiment is not as good as for O_2^- , the set of experimental points of Lee and Smith [82] is however reasonably well reproduced by the separable exchange and HFEGE approaches, with a better match of the HFEGE approach which exhibits the low energy bump observed in the experimental results. Among the three molecules considered in this study, OH^- is the one with the largest dipole moment. It is known from previous studies [55] that rotation should be taken into account in the case of strongly dipolar systems whereas it is neglected within our approaches. This approximation is a possible cause of the disagreement between theory and experiment for this system.

The calculated PD cross sections for CN^- are compared in Figure 2.3 with the only experimental point available. Our results agree reasonably well with the experiment but the cross section obtained from the scattered wave with separable exchange potential is too large. In order to assess the energy dependence of the cross section, we compared in the same figure our results with those obtained from state-of-the-art R-matrix calculation of Khamesian et al. [29]. Again the agreement with our calculations is relatively good, especially for the plane wave and scattered wave using a HFEGE potential. The PD cross section reported by Skomorowski et al. [85] for CN^- , calculated using the FBA, is slightly lower than ours using the same approximation. There are at least two reasons for this discrepancy. First, Skomorowski

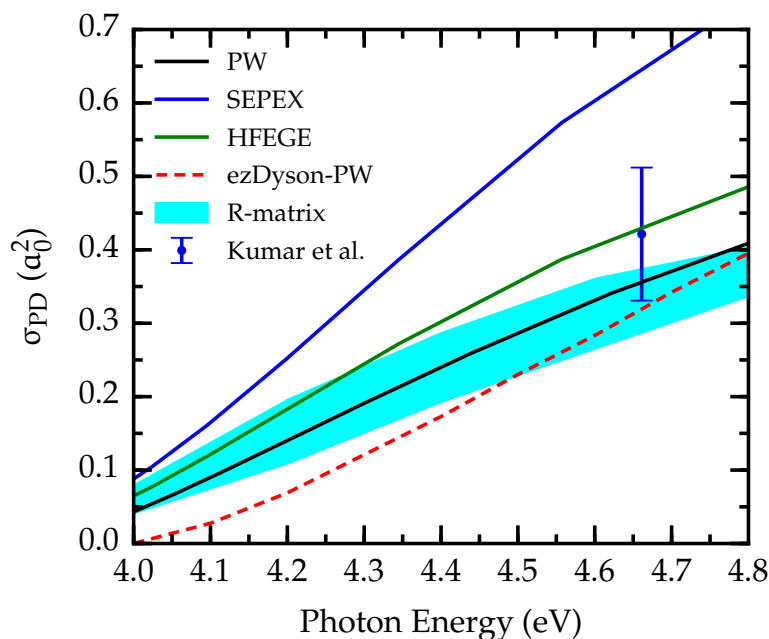


Figure 2.3: Experimental [31] and calculated PD cross section of CN^- . The cyan area corresponds to the R-matrix calculations of Khamesian et al. [29] while the red dashed line depicts the cross section obtained by Skomorowski et al. [85] using the FBA. Notation as in Figure 2.1.

et al. use a calculated value (3.99 eV) for the PD threshold energy, while we use the experimental value, namely 3.86 eV. The second reason for these differences is the basis set used in the calculation of the Dyson orbital. Skomorowski et al. use a GTO basis set while we use the VB3 STO basis set. The basis set dependence is discussed in more details in section 2.4.1.

There are unfortunately no experimental REA data for these three systems but two sets of theoretical calculations are available for CN using the complex Kohn variational principle [26] and the R-matrix method [29]. The results of this calculation are compared with ours in Figure 2.4. It can be seen that the cross sections calculated using scattered wave agree quite well with the R-matrix and Kohn variational result. Conversely, the FBA does not reproduce the very low collision energy behavior. This result is understandable as the FBA is expected to work well when the kinetic energy of the electron is large compared to the electron affinity of the target molecule. We then suggest that the scattered wave should be preferred for REA calculations at very low energy.

We eventually calculated the REA rate coefficient at 300 K by Boltzmann averaging of the REA cross sections for the three approaches presented above, see Table 2.3. In the case of CN, among the three continuum wave functions used, it is the plane wave which gives the best agreement with the value reported by Douguet et al. [26], $7 \times 10^{-16} \text{ cm}^3 \text{ molecule}^{-1} \text{ s}^{-1}$. While not realistic at very low energy, the FBA

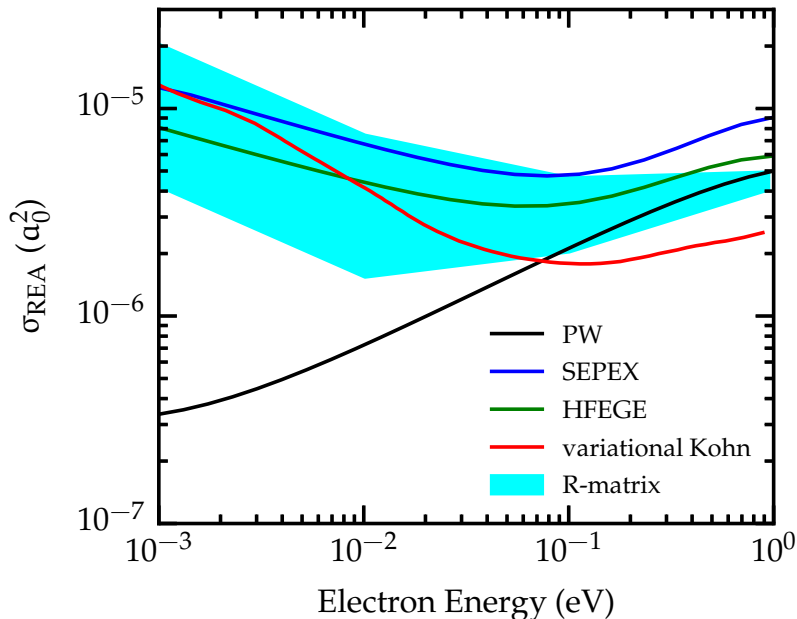


Figure 2.4: Calculated REA cross section of CN^- . The cyan area corresponds to R-matrix calculation of Khamesian et al. [29]. The red line corresponds to the variational Kohn calculations of Douguet et al. [26]. Notation as in Figure 2.1.

then appears to give the right order of magnitude of the REA rate coefficient at 300 K and offers a simple alternative for larger molecules for which the scattering wave calculations could be time consuming. Also shown in Table 2.3 are the REA rate coefficients obtained using the statistical expression proposed by Herbst [2]. The statistical rate coefficients differ from our calculations by about 2 orders of magnitude. However all calculations agree with the fact that the REA rate coefficients for diatomic molecules are particularly small.

Table 2.3: REA rate coefficients at 300 K for the different approaches discussed in the text. We have used the notation $a(b)$ which stands for $a \times 10^b$

Molecule	SEPEX	HFEGE	PW	Herbst
O_2	6.1(-20)	7.1(-20)	5.1(-19)	2.0(-17)
CN	1.6(-15)	1.1(-15)	4.4(-16)	4.0(-18)
OH	4.8(-16)	6.8(-16)	6.8(-16)	1.1(-18)

2.4.1 Comparison of the methods and basis sets for the Dyson orbital evaluations

As seen above, there are several methods available to calculate the Dyson orbital and it is also necessary to select a one-electron basis set. In this section, we investigate how the REA and PD cross sections are depending on the type and size of the one-

electron basis set and also on the method used to calculate the Dyson orbital. We consider both STO and GTO basis sets and apply the various approaches and basis sets to the three diatoms CN, O₂ and OH. As it was found in the previous section that the FBA gives reasonable results for a low computation time, we decided to use this approximation to carry out this study.

Figure 2.5 shows first a comparison of the PD cross sections obtained using several different electronic calculation method for obtaining the Dyson orbital. We compare CASSCF calculations with the HFFC approximation and the KS-B3LYP approach. As can be seen on this figure, the HFFC approximation moderately underestimates the exact CASSCF cross sections as it neglects the electron-correlation. In spite of the foregoing, the HFFC approach may offer a first estimate of the Dyson orbital when the size of the system prohibits performing exact CASSCF calculations.

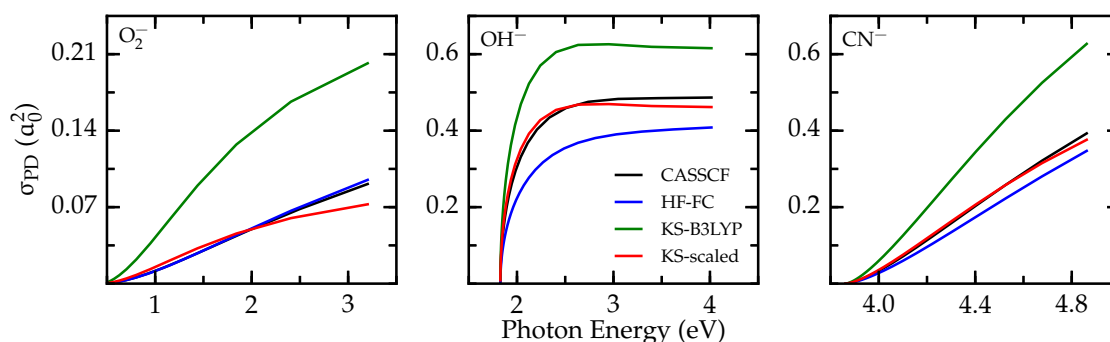


Figure 2.5: Plane wave PD cross section for different approaches in the calculation of the Dyson orbital.

We also find that the KS-B3LYP Dyson orbitals fail to provide the right order of magnitude of the PD cross sections as it always overestimates its value. As KS orbitals are proportional to the Dyson orbital [60] one can understand why KS orbitals are able to reproduce relative measurements like momentum distributions while they fail to estimate absolute values of the PD cross sections. This interpretation is confirmed by looking at the scaled KS results Figure 2.5, which reproduce correctly the energy dependence of the CASSCF PD cross sections.

We now focus on the convergence of the PD and REA cross sections as a function of the size and the type of basis set used to perform the computation of the Dyson orbital. These results are shown in Figure 2.6. The PD cross section for O₂⁻ shows almost no variation with respect to the choice of the basis set. Conversely, the PD cross section for OH⁻ and CN⁻ show a strong dependence. This can be understood by reminding that both OH and CN are polar molecules while O₂ is not. As a consequence the interaction potential between the electron and CN or OH is more long-ranged than for O₂ and more diffuse functions are then required to properly describe the interaction potential. This is indeed what can be seen in Figure 2.6.

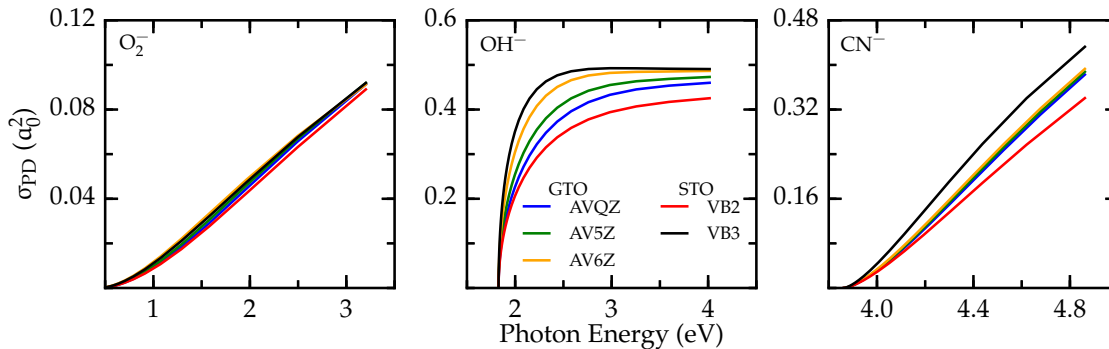


Figure 2.6: Plane wave PD cross section for different basis sets employed in the calculation of the Dyson orbital. $AVNZ \equiv aug\text{-}cc\text{-}pVNZ$.

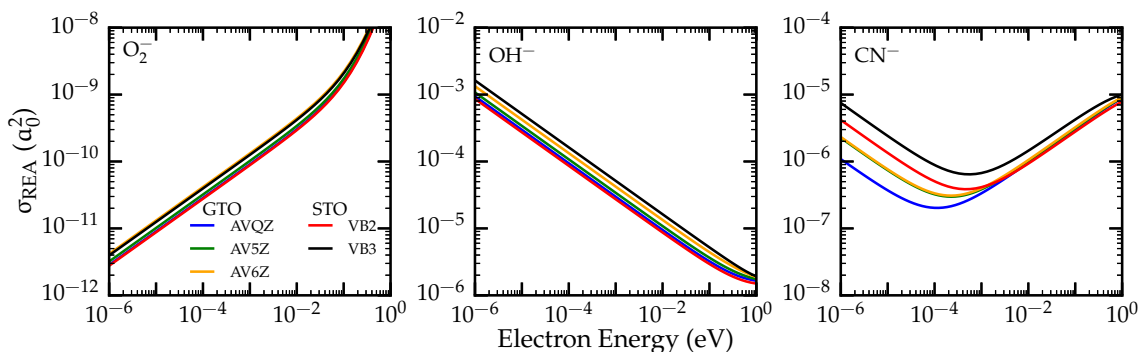


Figure 2.7: Plane wave REA cross section for different basis sets employed in the calculation of the Dyson orbital. $AVNZ \equiv aug\text{-}cc\text{-}pVNZ$.

The largest STO basis set gives better results than the GTO ones since they are more diffuse. This is clearly seen when comparing the VB3 and $aug\text{-}cc\text{-}pV6Z$ results in spite of the important difference of size between these two basis sets (Table 2.1). Since STOs reproduce accurately the cusp of the atomic orbitals, a smaller number of STOs is sufficient to properly describe the Dyson orbital in the short-range region.

If we now compare the results obtained for the REA cross sections, Figure 2.7, we can see that only the low energy regime is significantly dependent on the choice of the basis set. The explanation of this dependence is identical to the one discussed for the PD cross sections.

2.5 Conclusion

A new method based on a body-fixed single-center approach and a variety of approximations of the Dyson orbital was presented for the calculation of the PD and REA cross sections. Both the methods used to calculate the Dyson orbital and the scattered wave function were reviewed in detail. The methods were benchmarked by applying them to the three molecules CN^- , O_2^- and OH^- for which experimental PD data are available. The results of these approaches compare well with both

experimental data and the only R-matrix and Kohn variational principle calculations available. We however expect that it may not be the case for strongly polar molecules as it is based on a body-fixed approach.

We also compared available REA and PD data for these three systems with the results given by the combination of FBA and the calculation of a Dyson orbital. We found that a plane wave is an unexpectedly good approximation of the scattering wave of the studied systems. Furthermore this simplified approximation reduces drastically computer time.

The FBA was used to compare the results of several kinds of methods for the evaluation of the Dyson orbital which is a key ingredient in the calculation of PD and REA cross sections. We find that the KS-B3LYP results give the right energy dependence of the cross sections but overestimates the absolute magnitudes, while CASSCF and HFFC give relatively close results. The effects of the size and type of orbital basis set were also investigated still within the FBA. STO basis sets are found to perform better for a smaller number of basis functions than GTO basis sets. The FBA combined with the HFFC Dyson orbitals appears to be an efficient alternative tool for computing REA and PD cross sections for large molecular systems.

Chapter 3

REA and PD rate coefficients for carbon chains

Contents

3.1	Introduction	38
3.2	Methods	39
3.3	PD rate coefficients	39
3.4	REA rate coefficients	41
3.4.1	REA through the formation of dipole bound states	44
3.5	Conclusions	45

3.1 Introduction

So far, interstellar anions are expected to be formed by REA



Experimental measurements of REA are very difficult to perform mainly because of the very high vacuum required in order to prevent stabilization through collisions with the background gas particles. For this reason most electron attachment experiments [86–89] are only able to measure TBEA rates.

Long ago, Herbst [2] derived an expression for REA rate coefficients based on phase-space theory. This model makes the assumption that the electron is first attached through the formation of a temporary negative ion which is then stabilized by the emission of a photon. At this early time, accurate calculations were impossible to perform but the application of this model allowed Herbst to predict that for species with large electron affinities the REA coefficient could be close to $10^{-7} \text{ cm}^3 \text{ molecule}^{-1} \text{ s}^{-1}$ at cloud temperatures of 10–50 K. The same model was later on used to obtain REA rate coefficients for CN [90], C_3N [91], C_n [4] and C_nH [25].

More recently, Douguet et al. [26, 28], Khamesian et al. [29] revised the quantum theory of REA and proposed a new mechanism in which the electron is attached without the formation of any negative intermediate state. To distinguish the two mechanisms they called the one-step process direct-REA and indirect-REA, the two-step process proposed by Herbst [2]. They then calculated direct-REA rates for the six detected anions up to now and found results which are several orders of magnitude smaller than the indirect-REA rates calculated by Herbst and Osamura [25]. By applying a purely quantum-mechanical approach to the indirect mechanism, Douguet et al. [28] concluded that the contribution of indirect-REA process is negligible compared to that of direct-REA if no unusual threshold effects like virtual state, vibrational, Feshbach or dipolar resonances is involved in the process.

On the other hand, the reverse process PD (3.2) seems to be one of the most important mechanism of destruction of interstellar anions.



Kumar et al. [31] found for example that ultraviolet PD is the main destruction mechanism of both CN^- and C_3N^- anions in the IRC+10216 envelope. Experimental measurements of PD are easier to perform and experimental data are available for some of the detected anions [31, 92, 93]. On the theoretical side, many approaches have also been applied to the study of PD [27, 29, 85]. The main differences between these methods can be found in the treatment of the bound and continuum wave of the outgoing electron.

In the previous chapter, we introduced a method allowing to compute both the direct-REA and PD cross sections for diatomic molecules. It is based on the use of

the FBA and on the computation of Dyson orbital to describe the electron bound wave function. In the present chapter, we will extend this method to the study of larger molecules, our main objective is to compute both the REA and PD rates for the detected anions as well as for other potential candidates.

3.2 Methods

A PD process (3.2) with absolute cross section σ_{PD} proceeds at rate:

$$k_{\text{PD}} = 4\pi \int_{E_{\text{EA}}}^{E_{\text{H}}} J_{\lambda}(E) \sigma_{\text{PD}}(E) dE \quad (3.3)$$

where $J_{\lambda}(E)$ is the average intensity of the interstellar radiation field (ISRF) in units of photons $\text{cm}^{-2} \text{s}^{-1} \text{sr}^{-1} \text{eV}^{-1}$. The integral over photon energy E runs from the electron affinity threshold E_{EA} to the hydrogen ionization limit $E_{\text{H}} = 13.6 \text{ eV}$. Here, we use the ISRF defined by Heays et al. [94].

On the other hand, the thermally average rate coefficient for a REA process (3.1) with cross section σ_{REA} is:

$$k_{\text{REA}}(T) = \sqrt{\frac{8}{m_e \pi}} (k_B T)^{-3/2} \int_0^{\infty} \sigma_{\text{REA}}(\epsilon) e^{-\epsilon/k_B T} \epsilon d\epsilon \quad (3.4)$$

where k_B is the Boltzmann's constant, m_e and $\epsilon = E - E_{\text{EA}}$ are the electron mass and energy respectively.

The total REA cross section is the sum of the contribution from the direct-REA and indirect-REA processes. Following the conclusions of the study of Douguet et al. [28] we will neglect the contribution from indirect-REA in the present study and write $\sigma_{\text{REA}} \equiv \sigma_{\text{DREA}}$

The use of equations (3.3) and (3.4) would require the knowledge of both the PD and REA cross sections respectively. The calculation of PD and REA cross-section has been described in detail in section 2.2.1. Here we employ the FBA approximation to describe the continuum wave function and a Dyson orbital calculated at the CASSCF as the bound wave functions.

3.3 PD rate coefficients

The PD cross sections required for the calculation of the rate coefficients in equation (3.3), are calculated by neglecting the contributions from excited states of the neutral molecule. As the inclusion of these contributions will increase the PD rate coefficients, our calculations give a lower limit of the PD rate. Our results for the PD rates of selected linear anions are shown in Table 3.1.

We find that the PD rates are about the same order of magnitude regardless of the anion family and carbon chain size ($10^{-9} - 10^{-8}$). We then suggest that the present results can be used as a first rough estimate of the PD rates for other interstellar anions which have not been previously experimentally measured nor calculated.

3.3. PD RATE COEFFICIENTS

Table 3.1: PD rate coefficient k_{PD} in s^{-1} for selected linear molecular anions. The format $a(b)$ corresponds to $a \times 10^b$

n	C_n^-		C_nH^-	
	This work	Millar et al. [23]	This work	Millar et al. [23]
1		...	3.32(-8)	1.41(-8)
2	4.02(-9)	3.77(-9)	4.00(-9)	3.39(-9)
3	4.18(-9)	6.60(-9)	8.75(-9)	7.50(-9)
4	5.84(-9)	2.16(-9)	4.67(-9)	2.50(-9)
5	4.42(-9)	3.41(-9)	8.38(-9)	4.35(-9)
6	7.83(-9)	1.90(-9)	5.41(-9)	2.23(-9)
7	5.18(-9)	2.75(-9)	8.08(-9)	3.39(-9)
8	1.05(-8)	1.67(-9)	5.96(-9)	2.08(-9)
9	5.47(-9)	2.36(-9)	7.48(-9)	2.87(-9)
10	1.39(-8)	1.67(-9)	7.12(-9)	2.13(-9)

n	C_nN^-		HC_nO^-	
	This work	Millar et al. [23]	This work	Millar et al. [23]
1	5.10(-9)	2.17(-9)	8.48(-8)	1.38(-7)
2	4.92(-9)	3.86(-9)		...
3	3.90(-9)	1.80(-9)		...
4	5.14(-9)	3.14(-9)		...
5	5.03(-9)	1.70(-9)		...
6	6.44(-9)	2.74(-9)		...
7	4.90(-9)	1.53(-9)		...

Also shown in Table 3.1 are the rate coefficients obtained by estimating the PD cross section with the simple empirical formula, equation (4). This formula which was initially proposed by Millar et al. [23] has been widely used to obtain the PD rates currently included in most astrochemical databases like (KIDA¹, UMIST²). We then conclude that such PD rates are underestimated by approximately a factor of 3. Another important drawback of equation (4) is that it does not reproduce the energy dependence of the PD cross section especially at low photon energy as can be seen in Figure 3.1.

These two important deficiencies of equation (4) suggest that its use should be abandoned and replaced when possible by the present approach. We furthermore expect that the replacement of the previous database rate coefficients by our calculated values will lead to a decrease in the anion column density and will deteriorate the agreement between the modeled and observed anion-to-neutral abundances, as was shown by Kumar et al. [31].

¹<http://www.kida.obs.u-bordeaux1.fr>

²<http://www.udfa.ajmarkwick.net>

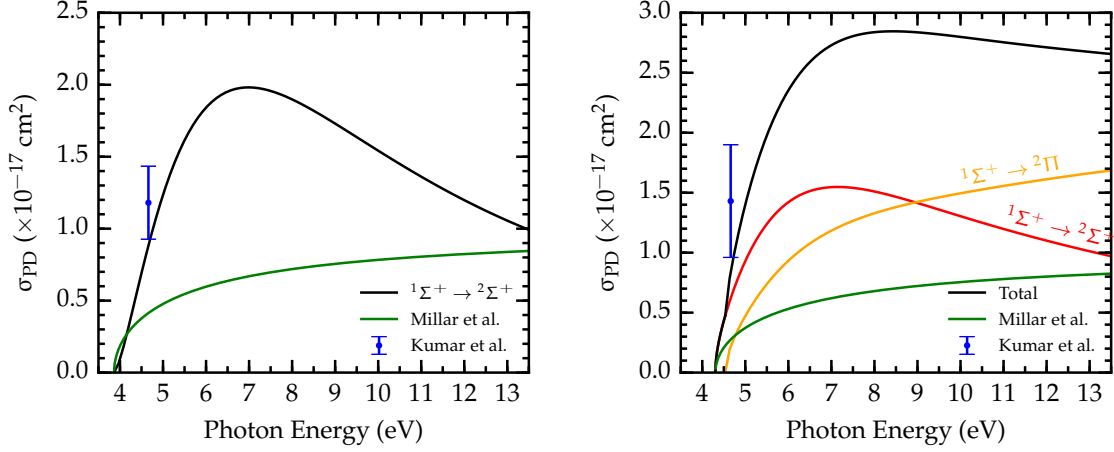


Figure 3.1: PD cross section of CN^- (left panel) and C_3N^- (right panel).

3.4 REA rate coefficients

The calculated REA rate coefficients for several linear chains are shown in Table 3.2 for the temperatures 10, 50, 100 and 300 K. As for the calculations of the PD rate coefficients, we neglect contributions from excited states of the neutral molecule in the calculations. This simplification should not change much the values of the REA rates since only the electronic ground state of the neutral molecules are populated for these low temperatures.

As can be seen in this table, the REA rate coefficients are extremely small ($10^{-17} - 10^{-14}$) in good agreement with the results of Douguet et al. [26, 27], Khameisian et al. [29]. For the largest chains the rate coefficients are seen to not vary as a function of temperature. At very low temperature the variation of the REA rate coefficient follows the threshold laws predicted by Wigner [95] as the interaction potential between one electron and a neutral molecule falls off faster than r^{-1} . The Wigner law for the cross section and rate coefficient are respectively: [48, 95]

$$\sigma_{\text{REA}}(\epsilon \rightarrow 0) = \sum_l a_l \epsilon^{l-1/2} \quad (3.5)$$

and

$$k_{\text{REA}}(T \rightarrow 0) = \sum_l b_l T^l \quad (3.6)$$

where l is the incoming electron angular momentum quantum number and a_l is a constant. If we only consider the first value λ of l for which a_l is not equal to zero we write:

$$k_{\text{REA}}(T \rightarrow 0) \approx b_\lambda T^\lambda + O(T^\lambda) \quad (3.7)$$

The value of λ can be straightforwardly determined using expansion (2.1) and (2.2) as well as the $\Delta l = \pm 1$ selection rule. Applying this simple rule we see that σ type ($l' = 0, 1, \dots$), π type ($l' = 1, 2, \dots$) or π_u type ($l' = 1, 2, \dots$) Dyson orbitals are

3.4. REA RATE COEFFICIENTS

Table 3.2: REA rate coefficient k_{REA} in $\text{cm}^3\text{molecule}^{-1}\text{s}^{-1}$ for selected linear molecules for various temperatures. The column Ψ_d corresponds to the symmetry type of the Dyson orbital. The format $a(b)$ corresponds to $a \times 10^b$

	n	Ψ_d	T = 10 K	T = 50 K	T = 100 K	T = 300 K
C_n	2	σ_g	1.03(-17)	5.19(-17)	1.04(-16)	3.14(-16)
	3	π_g	5.23(-18)	2.63(-17)	5.28(-17)	1.61(-16)
	4	π_g	2.34(-17)	1.17(-16)	2.33(-16)	6.97(-16)
	5	π_u	6.34(-15)	6.31(-15)	6.27(-15)	6.14(-15)
	6	π_u	1.22(-14)	1.22(-14)	1.21(-14)	1.17(-14)
	7	π_g	4.04(-17)	2.01(-16)	3.98(-16)	1.15(-15)
	8	π_g	6.48(-17)	3.21(-16)	6.34(-16)	1.82(-15)
	9	π_u	6.92(-15)	6.82(-15)	6.70(-15)	6.32(-15)
	10	π_u	8.30(-15)	8.14(-15)	7.95(-15)	7.39(-15)
	$C_n\text{H}$	1	π	2.36(-15)	2.37(-15)	2.38(-15)
2		σ	2.55(-16)	2.70(-16)	2.89(-16)	3.65(-16)
3		π	1.58(-16)	1.64(-16)	1.72(-16)	2.02(-16)
4		σ	2.77(-15)	2.80(-15)	2.83(-15)	2.97(-15)
5		π	1.87(-15)	1.86(-15)	1.84(-15)	1.80(-15)
6		π	1.67(-15)	1.67(-15)	1.66(-15)	1.62(-15)
7		π	3.87(-16)	4.15(-16)	4.51(-16)	5.85(-16)
8		π	7.54(-16)	7.73(-16)	7.95(-16)	8.80(-16)
9		π	1.38(-15)	1.36(-15)	1.35(-15)	1.30(-15)
10		π	1.12(-15)	1.11(-15)	1.11(-15)	1.09(-15)
$C_n\text{N}$	1	σ	1.30(-17)	5.71(-17)	1.12(-16)	3.31(-16)
	2	π	1.31(-15)	1.32(-15)	1.33(-15)	1.37(-15)
	3	σ	4.68(-15)	4.71(-15)	4.75(-15)	4.89(-15)
	4	π	1.41(-15)	1.41(-15)	1.41(-15)	1.39(-15)
	5	σ	8.92(-15)	8.94(-15)	8.96(-15)	9.07(-15)
	6	π	8.22(-16)	8.37(-16)	8.56(-16)	9.27(-16)
	7	π	2.34(-15)	2.35(-15)	2.36(-15)	2.40(-15)
HCO		σ	1.64(-17)	1.71(-17)	1.79(-17)	2.17(-17)

coupled with the electron s-wave ($l = 0$). Then the first non-vanishing term in (3.6) is b_0 and the REA rate coefficient in this case is constant at low temperature.

Conversely, σ_g ($l' = 0, 2, \dots$) or π_g ($l' = 2, 4, \dots$) Dyson orbitals are coupled with the p-wave ($l = 1$) then the first non-vanishing term in (3.6) is b_1 and the threshold rate coefficient increase linearly with the temperature. These behaviors can be clearly identified in Figure 3.2.

We see that these very simple symmetry arguments allow us sorting the REA rates at very low temperature without performing any calculation. Indeed REA processes ruled by p-wave electrons cannot take place when $T \rightarrow 0$ K ($k_{\text{REA}} \approx 0$) while those ruled by s-wave electrons can occur ($k_{\text{REA}} \neq 0$). This can be equivalently interpreted in terms of the presence or the absence of the centrifugal barrier

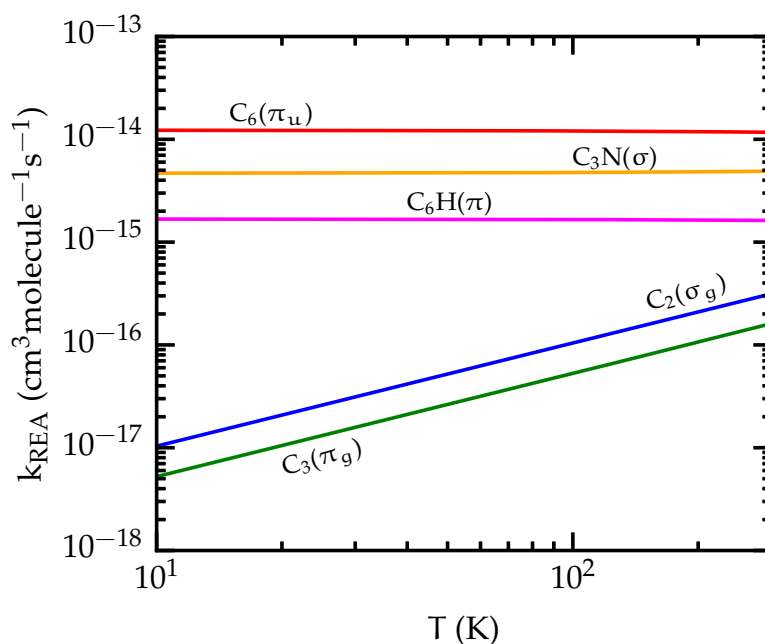


Figure 3.2: REA rate coefficient as a function of the temperature for selected linear chains. The curves are labeled by molecule and symmetry type of the Dyson orbital.

$-\frac{l(l+1)}{r^2}$. For s-wave electrons there is no centrifugal barrier so they can attach even at very low temperatures, conversely to p-wave electrons which cannot approach the molecule because of the centrifugal barrier.

So far REA rate coefficients used to model the formation of interstellar anions (KIDA, UMIST) have been calculated using the model proposed by Herbst [2], see Table 3.3.

Table 3.3: Currently used REA rate coefficients for linear molecules. The rate coefficient are given for $T = 300$ K. In order to obtain these rate coefficient at different temperatures, the values must be multiplied by $(T/300)^{1/2}$. The format $a(b)$ corresponds to $a \times 10^b$

n	C_n [4]	$C_n\text{H}$ [25]	$C_n\text{N}$
2	...	2.0(-15)	...
3	...	1.7(-14)	2.6(-10) [91]
4	1.4(-8)	1.1(-8)	...
5	3.3(-8)	4.1(-8)	1.3(-7) [96]
6	1.7(-7)	6.2(-8)	...
7	5.0(-7)	1.9(-7)	...
8	1.7(-7)	6.2(-8)	...
9	5.0(-7)

This model is based on phase space theory and consider only contributions from the indirect-REA mechanism.



k_{REA} in this case is obtained from the following expression

$$k_{\text{REA}} = \frac{k_c k_r}{k_d + k_r} \tag{3.9}$$

In this expression k_d is negligible in comparison with k_r for the largest molecules. In this case k_{REA} reduces to the capture rate k_c which is given by:

$$k_c = \frac{\hbar^2 g_a}{g_n} \sqrt{\frac{2\pi}{m_e^3 kT}} = 4.982 \times 10^{-7} \frac{g_a}{g_n} \left(\frac{T}{300\text{K}} \right)^{-\frac{1}{2}} \tag{3.10}$$

If we compare our results with those of Herbst given in Table 3.3 we can see that apart from the smallest molecules C_2H and C_3H , the two methods give results which differ by several orders of magnitude. The main reason for this strong discrepancy is, we believe, due to the main assumption of the model of Herbst [2] which states that all the collisions lead to the formation of a transient negative ion thus overestimating strongly the indirect-REA cross sections. Moreover, as mentioned before, a recent quantum mechanical treatment of the indirect-REA process showed that indirect-REA is negligible with respect to the direct-REA mechanism [28].

The very small value of our calculated direct-REA rate coefficients cannot explain the formation of the interstellar anions and then demonstrate that the actual astrochemical models of the formation of anions are strongly deficient.

3.4.1 REA through the formation of dipole bound states

Recently, Carelli et al. [97] discussed the possibility of forming interstellar anions through the formation of dipole-bound states. These very excited states of the anion lie a few meV below the neutral ground state and can be formed only by molecules whose permanent dipole moment is greater than the critical value of 2.5 Debye. This critical value was suggested long ago by Fermi and Teller and revisited since then by many authors [98]. In any case the application of this mechanism could apply only to this kind of molecules and then cannot explain the formation of all the interstellar anions. Here, we consider the special case of C_3N^- but we will see that the results obtained for this anion can be extrapolated to some other systems. Two dipole-bound states of C_3N^- with symmetry $a^3\Sigma$ and $A^1\Sigma$ were found at the CASSCF level, their binding energies being respectively equal to $E_b = 0.25$ meV and $E_b = 0.21$ meV. The REA rate of these dipole-bound states are shown in Figure 3.3. We can see in this figure that the formation of dipole-bound states is quite small compared with

the formation of the anion in its electronic ground state $X^1\Sigma$, $E_b = 4.305$ eV. This suggests that the role of the dipole bound states in the formation of the anion is negligible.

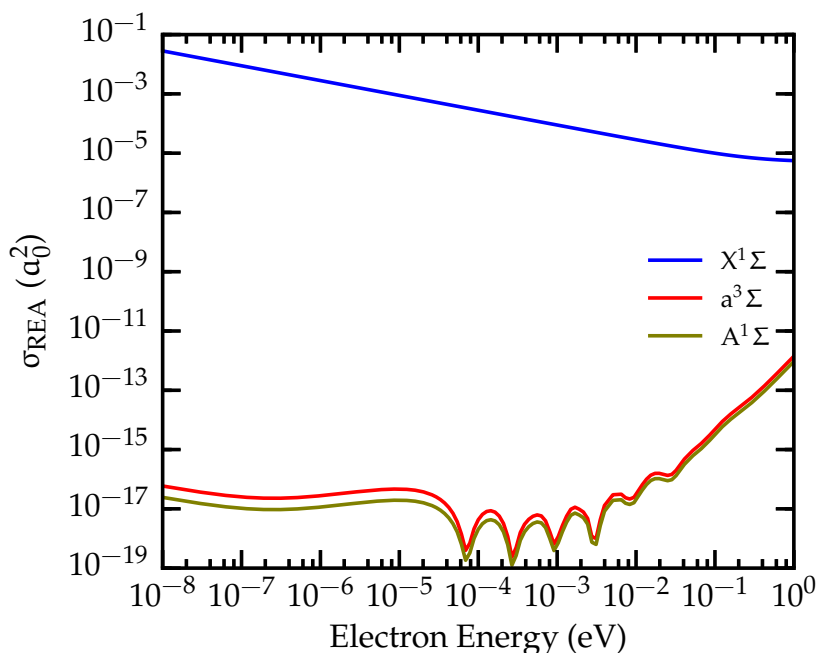


Figure 3.3: REA cross section of C_3N . The curves are labeled by the electronic state of the C_3N^- anion.

The very small value of the REA rate coefficient for the formation of dipole bound states is simply due to the very small value of their binding energies. It can indeed be demonstrated using equations (2.3), (2.7) and $E = E_b + \epsilon$ that $\sigma_{\text{REA}} \propto (E_b)^3$ at low electron energy. This means that the bigger the binding energy the bigger will be the REA cross sections. We can then conclude that the formation of a dipole-bound state of the anion can be neglected compared with the formation of the anion in its ground state.

3.5 Conclusions

REA and PD cross section were calculated for the six detected anions as well as for several other potential candidates. The cross sections were obtained by using Dyson orbitals to describe the bound wave function of the anion and a plane wave for describing the free electron. PD rates were calculated for several anions belonging to the families C_n^- , C_nH^- , C_nN^- and HC_nO^- . A comparison between our rates and the rates currently used in the astrochemical model shows that the latter strongly underestimate the PD rates. The inclusion of our PD rates in the astrochemical model will then strongly decrease the anion-to-neutral abundance, thus deteriorating the current agreement between models and observations. REA rates, as well as the

3.5. CONCLUSIONS

rates of formation of dipole-bound states, were also calculated and compared with the currently used values.

We found that the current REA rates are overestimated by several orders of magnitudes. Our results suggest that interstellar anion cannot be formed by REA even through the formation of transient dipole bound states. Consequently, the current agreement between observed and modeled anions abundances is artificial. Other mechanisms like DEA, need then to be thoroughly explored in order to understand the formation of anions in the interstellar condition.

Chapter 4

Interaction of rigid C_3N^- with He: PES, bound states and rotational spectrum

Contents

4.1	Introduction	48
4.2	PES: ab-initio calculations and functional form	48
4.2.1	Features of the PES	51
4.3	Bound states calculations	52
4.4	Rovibrational spectrum	57
4.5	Conclusion	58

Published

M. Lara-Moreno, T. Stoecklin, and P. Halvick. Interaction of rigid C_3N^- with He: Potential energy surface, bound states, and rotational spectrum. *J. Chem. Phys.*, 146(22):224310, 2017

4.1 Introduction

Cyanoethynyl anion C_3N^- is one of the six molecular carbon chain anions detected in the ISM. It has been detected in two different sources: the carbon star IRC+10216 and the molecular cloud TMC-1 [10]. Both sources are rich in highly saturated long carbon chain (C_nH , C_nN) for which electron attachment rate coefficients are estimated to be large due to their high electron affinities and molecular sizes [2]. Within this hypothesis, the abundance ratio $[A^-]/[A]$ of the C_3N^- anion should be approximately 1% [91]. Experimentally the magnitude of this ratio is obtained from the analysis of emission spectra and requires the knowledge of radiative and collisional rate coefficients with the most abundant species. In the absence of such collisional data, the application of the LTE approximation is known to produce a poor estimate of the abundance of a given specie in the regions of ISM where the density of particles is insufficient for the establishment of LTE. This is the reason why, as the first step of a general study of this anion in the ISM, we developed the first PES for the $He-C_3N^-$ collision which is presented in section 4.2.

The second part of this chapter is dedicated to the calculation of the bound states energy levels as well as the rovibrational spectrum of the $He-C_3N^-$ van der Waals complex. The calculation of such spectrum is often used to test the accuracy of the PES by comparison with experiment. In the case of $He-C_3N^-$, the experimental spectrum has not been experimentally measured yet. Nevertheless, we hope that this first theoretical work will be of help in the future assignation of the experimental rovibrational spectrum. The bound states calculations and the spectrum computation are respectively presented in section 4.3 and 4.4. The conclusion of this study is presented in section 4.5.

4.2 PES: ab-initio calculations and functional form

C_3N^- , in its $^1\Sigma$ electronic ground state, is a closed-shell linear floppy molecule as indicated by the low value of the frequency of its ω_5 bending mode ($\omega_5 = 203 \text{ cm}^{-1}$) [100]. For a floppy molecule, the use of the rigid monomer approximation is questionable. However in a recent study dedicated to the rovibrational excitation of C_3 by collisions with He, Stoecklin et al. [101] have shown that the use of this approximation leads to accurate results for rotational excitation provided that the maximum temperature considered in the calculations is lower than the vibrational threshold. In the case of C_3N^- , the rigid monomer calculations should then be accurate for temperatures $T < 300\text{K}$ which is the domain of interest for the regions of the ISM where this anion was detected.

Interaction energies were first computed for a 2D grid of geometries of the $He-C_3N^-$ complex expressed in body-fixed Jacobi coordinates (R, θ) , where R

Table 4.1: He–C₃N⁻ interaction energy at R = 6.50 a₀, θ = 90°. BF stands for bond functions.

Basis set	Energy (cm ⁻¹)
aug-cc-pVTZ	-52.526
aug-cc-pVTZ + BF	-58.790
aug-cc-pVQZ	-56.280
aug-cc-pVQZ + BF	-59.282

stands for the intermolecular distance between He and the center of mass of C₃N⁻ while θ is the angle between the C₃N⁻ axis and the intermolecular axis, with θ = 0 corresponding to He facing the N-end of C₃N⁻. These calculations were done at the coupled cluster level with the CCSD(T) [102] method and using the aug-cc-pVQZ basis set complemented with a set of mid-bond functions [103] to get a better description of the van der Waals interaction.

A comparison of the interaction energy computed at a near equilibrium configuration for different basis sets with or without the inclusion of bond functions, placed at the half of intermolecular distance, is shown in Table 4.1. It can be appreciated that the interaction energy shows a small variation with respect to the size of the basis sets and the inclusion of bond function. If we consider the two basis sets with bond functions, the energy difference is less than 0.5 cm⁻¹. It can be expected that the lowering of energy induced by the aug-cc-pV5Z + bond functions will be even smaller. At this point it is safe to assume that the aug-cc-pVQZ + bond functions basis set is sufficient enough to describe the He–C₃N⁻ complex.

The inclusion of bond functions at short R distances can affect the repulsive wall but for these configurations, due to the overlap between He and C₃N⁻ electronic clouds, the interaction energy is significantly large. As this PES has been designed for cold chemistry, this implies that for typical collisions, most of the repulsive wall belongs to the classically forbidden region. Therefore the possible distortion of the repulsive wall induced by the bond functions is expected to have no effect on the collisional dynamics at low temperature.

All the C₃N⁻ bond distances were set to their equilibrium values in the ground state obtained from corrected CCSD(T)/aug-cc-pV5Z calculations [100], namely r_{C₁-C₂} = 2.3653 a₀, r_{C₂-C₃} = 2.5817 a₀, r_{C₃-N} = 2.2136 a₀. This correction is based on the bond length deviation between the accurate equilibrium structure for HC₃N, established through the combination of experimental and theoretical data, and the one obtained from CCSD(T)/aug-cc-pV5Z calculations. The radial grid includes 31 values of R ranging from 2 to 50 a₀ while the angular grid was made of 37 values of θ ranging from 0° to 180° by step of 5°. The use of this fine angular grid was required for reproducing the very strong angular anisotropy of the PES. All the calculations were done using the MOLPRO package [34] and the total number of geometries con-

sidered was 1147. The interaction energy was obtained by subtracting the energy of the complex to the sum of the energies of the two isolated monomers, the latter being computed in the same basis set than the complex. This corresponds to the basis set superposition error (BSSE) correction by using the counterpoise procedure of Boys and Bernardi [104] applied to the rigid rotor case. The functional form of the PES used to fit this grid of energy is defined as the sum of two terms associated with the long-range v_{LR} and short-range v_{SR} contributions and mixed by a switching function $S(R)$:

$$V(R, \theta) = S(R)v_{SR}(R, \theta) + [1 - S(R)]v_{LR}(R, \theta) \quad (4.1)$$

where

$$S(R) = \frac{1}{2} [1 - \tanh(A_0(R - R_0))] \quad (4.2)$$

The long-range v_{LR} and short-range v_{SR} functions are expressed in a basis set obtained by a product of radial and angular functions:

$$v(R, \theta) = \sum_l f_l(R) P_l(\cos \theta) \quad (4.3)$$

where the P_l are normalized Legendre polynomials. Sets of 21 ($0 \leq l \leq 20$) and 5 ($0 \leq l \leq 4$) angular functions were respectively used for describing the short-range and long-range contributions. As mentioned before, a large number of angular functions were required for describing the strong angular anisotropy of the short-range interaction energy. The long-range radial functions are defined as linear combinations of reciprocal power functions:

$$f_l^{LR}(R) = \sum_{k=4}^8 \frac{t_k(\beta R)}{R^k} C_{lk} \quad (4.4)$$

where t_k is the Tang-Toennies damping function:

$$t_k(x) = 1 - e^{-x} \sum_{i=0}^k \frac{x^i}{i!} \quad (4.5)$$

The fitting procedure of this functional form was performed in two steps. First, a weighted linear least squares procedure was used to determine the expansion coefficient $f_l(R)$ in equation (4.3) for each point of the radial grid. Then a cubic spline interpolation of these coefficients was used to obtain the short-range radial functions. In order to decrease the fitting error in the regions of the PES where the interaction energy is lower than a threshold E_0 , an energy-dependent hyperbolic tangent weighting function was used:

$$w(E) = w_{\min} + \frac{w_{\max}}{2} [1 - \tanh(\alpha(E - E_0))] \quad (4.6)$$

For small values of R and for θ close to 0° or 180° , the He atom is very close to one end of the C_3N^- molecule. The interaction energy becomes extremely large. Fitting correctly this drastic variation of the interaction energy would require a very large angular basis set. Furthermore, in some cases, the CCSD(T) calculations happen to

fail. Therefore, a cut-off energy was set at $50\,000\text{ cm}^{-1}$ to circumvent both difficulties. Such large cut-off energy is expected to have no consequences in the collisional dynamics at low temperatures.

In the second step, the $f_l^{LR}(R)$ functions were obtained from a least square fitting to equation (4.4), using only ab-initio data for $R \geq 15\ a_0$. The non-linear parameter as well as those of the weighting function were determined by the trial and error method, giving the following values: $A_0 = 1.8\ a_0^{-1}$, $R_0 = 18\ a_0$, $\beta = 6.0\ a_0^{-1}$, $w_{\min} = 0.01$, $w_{\max} = 100$, $E_0 = 4000\text{ cm}^{-1}$, $\alpha = 1.553 \times 10^{-3}\text{ cm}$.

An estimate of the accuracy of the fit was obtained by computing the root mean square (RMS) of the differences between the ab-initio and fitted energies. In the attractive region ($E < 0$) the RMS is 0.007 cm^{-1} and the maximum difference is 0.05 cm^{-1} while in the long-range region ($E < 0$, $R \geq 14\ a_0$) the RMS is even lower (0.0025 cm^{-1}). As expected the major differences are found for the repulsive part ($E > 0$) where the RMS increases proportionately as the energy. For energies below $5\,000\text{ cm}^{-1}$ the maximum difference is 0.779 cm^{-1} and the maximum relative error is 0.018%. For R smaller than the radial lower bound of the ab-initio data, large and sudden fluctuations of the fitted energies are a common artifact arising from polynomial interpolation. We checked the PES and concluded that the repulsive part has a realistic behavior up to $40\,000\text{ cm}^{-1}$.

4.2.1 Features of the PES

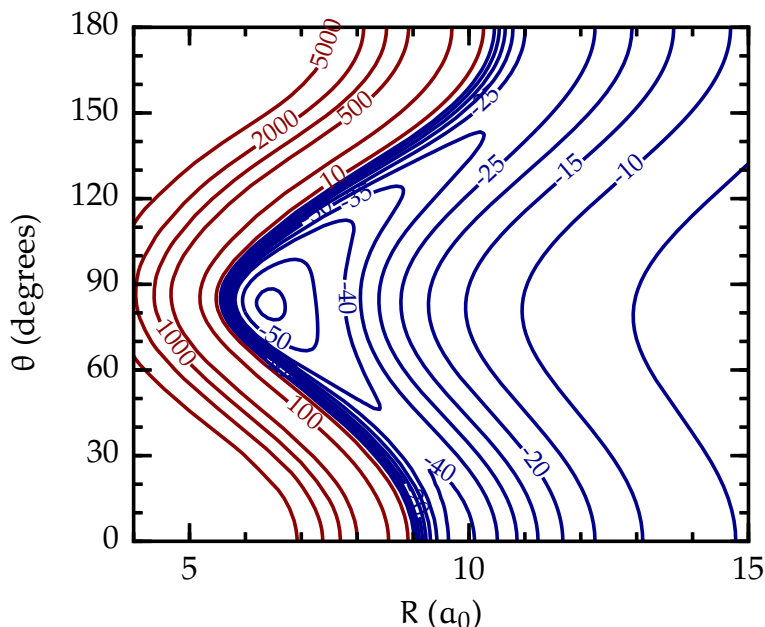


Figure 4.1: Contour plot of the PES. Contour levels are labeled by the energy given in cm^{-1} . The blue and red contour lines are respectively associated with negative and positive interaction energies.

Figure 4.1 shows a contour plot of the PES. The global minimum is found at a near T-shape geometry of the complex, namely $R = 6.42 a_0$, $\theta = 82.96^\circ$, with the dissociation energy $D_e = 62.114 \text{ cm}^{-1}$. A secondary minimum with $D_e = 41.384 \text{ cm}^{-1}$ is also found for a linear configuration of the system in which the N-end points to the He atom, with $R = 9.83 a_0$ and $\theta = 0^\circ$. The saddle point between these two minima appears at 22.595 cm^{-1} above the global minimum for the bent geometry $R = 8.83 a_0$ and $\theta = 37.85^\circ$. A second saddle point at 33.604 cm^{-1} above the global minimum, with the linear geometry $R = 11.5 a_0$ and $\theta = 180^\circ$, connects the two equivalent configurations of the global minimum.

In Figure 4.2 the Legendre polynomial expansion coefficients defined in equation (4.3) are represented as a function of the intermolecular coordinate. For distances up to $10 a_0$, the even terms are the largest while the potential appears clearly to be strongly anisotropic. For larger distances, the $l = 0$ isotropic term is the largest although the $l = 1$ and 2 contributions are still not negligible for distances smaller than $16 a_0$. Also shown in Figure 4.2, the long-range interaction leading contribution $l = 0$ agrees very well with the charge-induced dipole interaction energy

$$V = -\frac{\alpha e^2}{2R^4} \quad (4.7)$$

where α is the static dipole polarizability of the helium atom. This agreement confirms the validity of our ab-initio calculations and suggests that our PES is a realistic model for the study of low energy collisions. It also means eventually that the inelastic rate coefficients, in agreement with the Langevin's law, should be constant at very low temperature.

4.3 Bound states calculations

The calculation of the bound states can give valuable information about the dynamics of the van der Waals complex as shown in two recent studies [105, 106]. We use here a slightly different approach and solve the variational Schrödinger equation of the system expanding the solutions in a basis set which is made of a direct product of a one-dimensional radial basis set describing the motion along R coordinates and a coupled angular basis set describing both the rotation of the linear molecule and the relative angular motion of the atom with respect to the C_3N^- molecule. The latter coupled angular basis set takes the usual form:

$$y_{jl}^{JM}(\hat{\mathbf{R}}, \hat{\mathbf{r}}) = \sum_{m_j=-j}^j \sum_{m_l=-l}^l \langle j m_j l m_l | JM \rangle Y_{j m_j}(\hat{\mathbf{r}}) Y_{l m_l}(\hat{\mathbf{R}}) \quad (4.8)$$

where $Y_{j m_j}(\hat{\mathbf{r}})$ and $Y_{l m_l}(\hat{\mathbf{R}})$ are spherical harmonics. In order to describe accurately the stretching motion of the complex, we need a basis set allowing to simulate the radial motion both in the short-range strong anharmonic potential and the long-range charge-induced dipole potential. The usual imaginary exponentials or Chebyshev

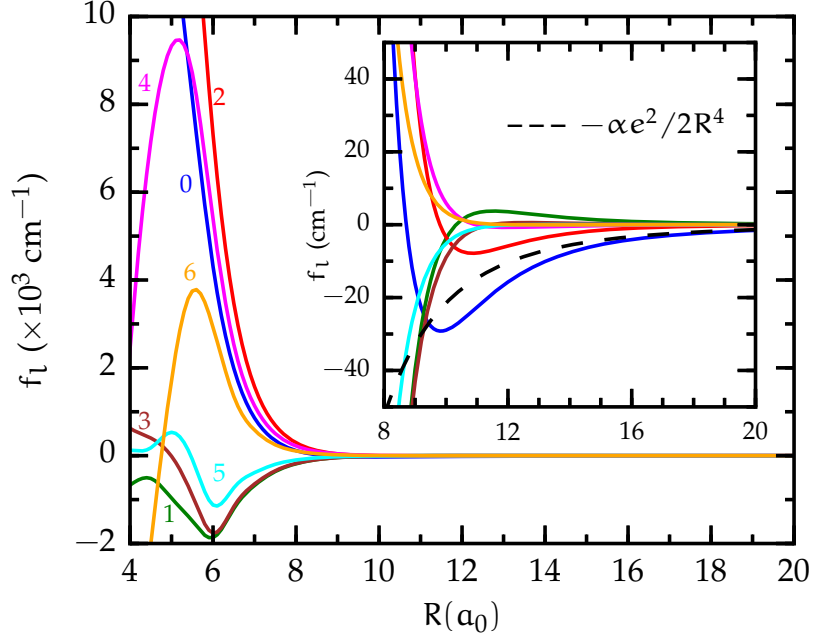


Figure 4.2: Variation of the first eight Legendre expansion coefficients $f_l(R)$ of the interaction energy as a function of the intermolecular distance. The curves are labeled by the corresponding value of l . The dashed black line shows the long-range charge-induced dipole interaction energy.

basis sets, as well as all the basis sets providing evenly spaced DVR grids are inefficient to achieve this goal. Conversely, Sturmian functions [107] which are highly anharmonic and allow using a sparse grid of points in the long-range region have been shown to be very effective for describing the radial motion [108, 109]. The most widely used Sturmian functions are those associated with the Coulomb potential, the generating equation is given by:

$$\left[\frac{d^2}{dR^2} + \frac{l(l+1)}{R^2} - \frac{2kn}{R} - E_0 \right] S_{nl}(R) = 0 \quad (4.9)$$

where

$$S_{nl}(R) = \left\{ \frac{(n-l-1)!}{[(n+l)!]^3} \right\}^{1/2} e^{-kR} (2kR)^{l+1} L_{n+l}^{2l+1}(2kR) \quad (4.10)$$

and where $L_{n+l}^{2l+1}(2kR)$ are the associated Laguerre polynomial and k is an energy dependent parameter. As the Sturmian functions defined in equation (4.10) are orthonormal with respect to the weight function R^{-1} , we use a set of orthonormal Sturmian functions defined by $\mathcal{S}_{nl} = \sqrt{\frac{1}{R}} S_{nl}$ such that

$$\langle \mathcal{S}_{ml} | \mathcal{S}_{nl} \rangle = \int_0^\infty \frac{1}{R} S_{nl}(R) S_{ml}(R) dR = \delta_{mn} \quad (4.11)$$

The matrix elements of the kinetic operator in this new basis set are then obtained by using the chain rule as well as equation (4.9) and (4.11):

$$\begin{aligned} \langle \mathcal{S}_{ml} | \mathbf{T} | \mathcal{S}_{nl} \rangle &= -\frac{\hbar^2}{2\mu} [k^2 \delta_{mn} - k(2n-1) \langle \mathcal{S}_{ml} | \frac{1}{R} | \mathcal{S}_{nl} \rangle + [l(l+1) - n + 3/4] \\ &\quad \times \langle \mathcal{S}_{ml} | \frac{1}{R^2} | \mathcal{S}_{nl} \rangle + \sqrt{n(n-1) - l(l+1)} \langle \mathcal{S}_{ml} | \frac{1}{R^2} | \mathcal{S}_{n-1,l} \rangle] \end{aligned} \quad (4.12)$$

where for $n \geq m$:

$$\begin{aligned} \langle \mathcal{S}_{ml} | R^p | \mathcal{S}_{nl} \rangle &= (-1)^{n+m} \frac{(2l+p+1)!}{(2k)^p} \left[\frac{(n-l-1)!(m-l-1)!}{(n+l)!(m+l)!} \right]^{\frac{1}{2}} \\ &\quad \times \sum_{i=0}^{m-l-1} \binom{p}{n-l-i-1} \binom{p}{m-l-i-1} \binom{2l+p+i+1}{i} \end{aligned} \quad (4.13)$$

A Sturmian DVR grid of 150 points in the range $[3,50] a_0$ is then generated from the zeros of the Laguerre polynomials. The matrix elements of the kinetic operator in the DVR grid are computed by using equation (4.12) and the Sturmian collocation matrix which is obtained from the diagonalization of the R operator in the Sturmian basis using equation (4.13). The vibrational ground state rotational constant of C_3N^- was set to its experimental value, $B_0 = 4851.62183$ MHz [10]. The parameter k was chosen in order to set up the maximum value of R of the DVR grid.

The Hamiltonian matrix calculated in the direct product basis set made of the DVR Sturmian grid and the angular basis set is then diagonalized for a given value of the total angular momentum J and of the parity $\epsilon = (-1)^{j+l}$. The convergence of the bound states as a function of both the size of the DVR grid and the number of rotational basis functions was checked. The maximum value of the total angular momentum J leading to bound states was found to be 10. A total of 134 bound states were obtained for the He- C_3N^- complex. In table 4.2, the $J \leq 2$ bound states energies are given with respect to the asymptotic limit of the infinitely separated fragments C_3N^- and He.

The zero point energy of the complex is 34.473 cm^{-1} . This energy is larger than the potential energy of both saddle points. Consequently the ground state wave function of the He- C_3N^- complex is spread over the whole interval of variation of the angular coordinate.

This result can be observed in Figure 4.3 where all the $J = 0$ bound state wave functions are shown. One can also see in the same figure that the most probable configuration of the complex in the ground state is located around the near T-shape minimum of the PES while the wave function extends up to the linear geometry.

In Table 4.2, we report our tentative assignation of the vibrational quantum numbers v_1 and v_2 obtained from the analysis of the bound states wave functions represented in Figure 4.3. It can be seen in the panels 2 and 3 of Figure 4.3 that both fundamental modes result from a combination of motions along the R and θ coordinates. The analysis of the wave function and the assignation of the vibrational quantum numbers become more and more difficult when J increases. This task be-

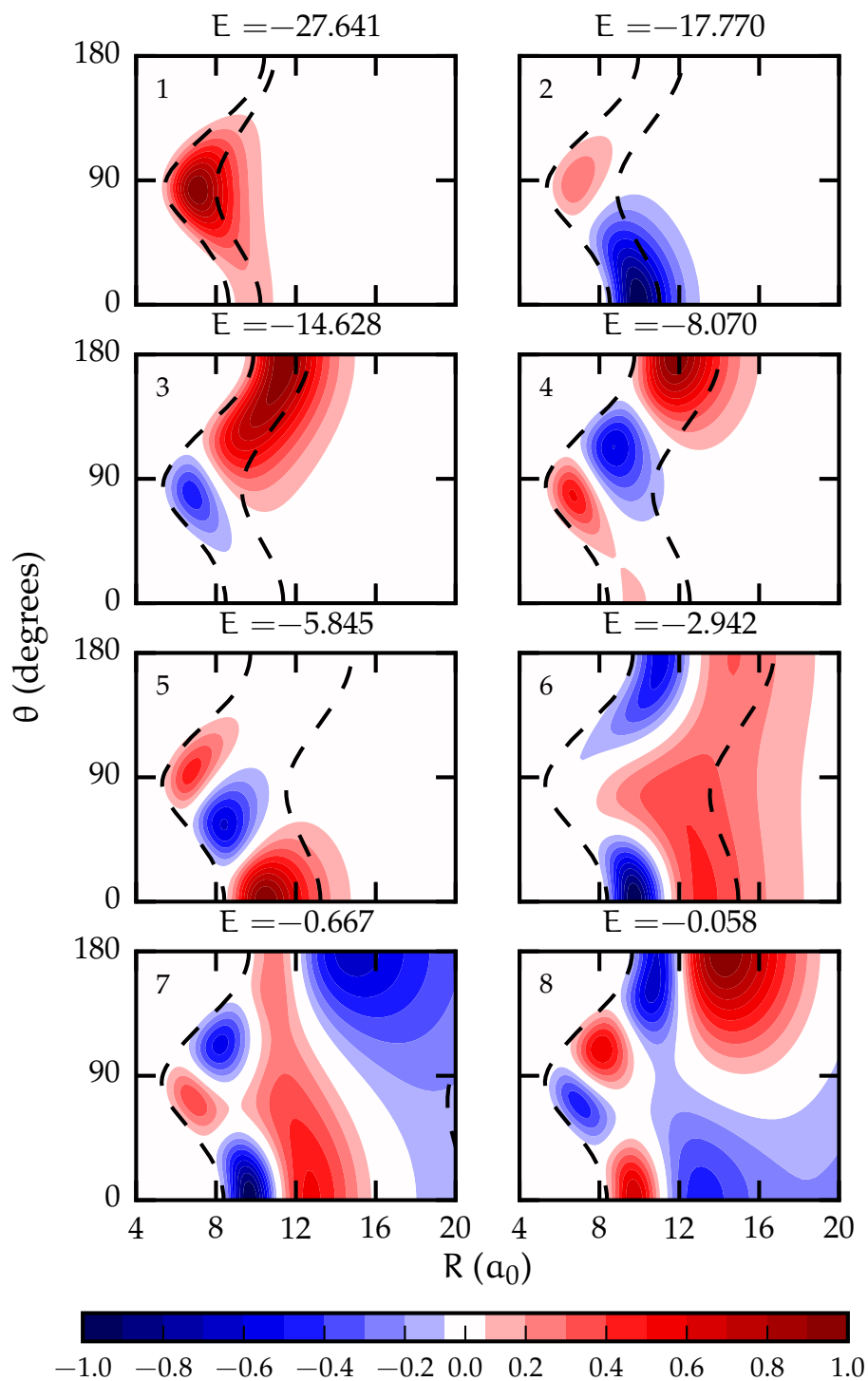


Figure 4.3: Contour plot of the bound states wave functions for total angular momentum $J = 0$. The bound states are labeled by their energy. The black dashed line is the potential isoline equal to the energy of the bound state.

4.3. BOUND STATES CALCULATIONS

Table 4.2: Bound states energies of the He–C₃N[−] van der Waals complex for $J \leq 2$ and their tentative assignment. v_1 and v_2 are the vibrational quantum numbers of the complex, ϵ is the parity and J_{K_a, K_c} is the asymmetric top rotational quantum number. Unassigned bound states are labeled with the symbol *.

J	ϵ	Energy (cm ^{−1})	v_1	v_2	J_{K_a, K_c}	J	ϵ	Energy (cm ^{−1})	v_1	v_2	J_{K_a, K_c}
0	+	−27.64	0	0	0 ₀₀	1	+	−0.52	*	*	*
0	+	−17.77	1	0	0 ₀₀	2	−	−26.03	0	0	2 ₀₂
0	+	−14.63	0	1	0 ₀₀	2	−	−24.50	0	0	2 ₁₂
0	+	−8.07	2	0	0 ₀₀	2	+	−24.32	0	0	2 ₁₁
0	+	−5.84	0	2	0 ₀₀	2	−	−19.82	0	0	2 ₂₀
0	+	−2.94	*	*	0 ₀₀	2	+	−19.82	0	0	2 ₂₁
0	+	−0.67	*	*	0 ₀₀	2	−	−16.73	1	0	2 ₀₂
0	+	−0.06	*	*	0 ₀₀	2	−	−13.71	0	1	2 ₀₂
1	+	−27.10	0	0	1 ₀₁	2	−	−10.17	1	0	2 ₁₂
1	+	−25.51	0	0	1 ₁₁	2	+	−10.04	1	0	2 ₁₁
1	−	−25.45	0	0	1 ₁₀	2	−	−9.46	0	1	2 ₁₂
1	+	−17.42	1	0	1 ₀₁	2	+	−9.37	0	1	2 ₁₁
1	+	−14.32	0	1	1 ₀₁	2	−	−7.05	2	0	2 ₀₂
1	+	−10.87	1	0	1 ₁₁	2	−	−4.68	0	2	2 ₀₂
1	−	−10.83	1	0	1 ₁₀	2	+	−3.58	*	*	*
1	+	−10.19	0	1	1 ₁₁	2	−	−3.58	*	*	*
1	−	−10.16	0	1	1 ₁₀	2	−	−2.29	*	*	*
1	+	−7.73	2	0	1 ₀₁	2	−	−0.98	*	*	*
1	+	−5.45	0	2	1 ₀₁	2	+	−0.89	2	0	2 ₁₂
1	+	−2.72	*	*	*	2	−	−0.79	2	0	2 ₁₁
1	+	−1.55	2	0	1 ₁₁	2	+	−0.79	*	*	*
1	−	−1.52	2	0	1 ₁₀	2	−	−0.25	*	*	*

comes almost impossible for $J > 4$ as these states get closer to the dissociation limit and reach quickly a chaotic regime already observed for $J = 0$ in the panels 7 and 8 of Figure 4.3.

The rotational constants of the van der Waals complex can also be easily extracted from the rotational splitting of the $J = 1$ vibrational levels reported in Table 4.2, leading to the following values: $A_0 = 56654.61$ MHz, $B_0 = 8979.54$ MHz, $C_0 = 7172.74$ MHz. The corresponding value of the asymmetry parameter is $\kappa = -0.93$, showing that the He–C₃N[−] van der Waals complex is a near prolate asymmetric top.

4.4 Rovibrational spectrum

We neglected the hyperfine structure of C₃N⁻ and calculated the relative absorption intensity for a given rovibrational transition $i'J' \leftarrow iJ$ of the He–C₃N⁻ complex at a temperature T by using the expression:

$$I_{i'J' \leftarrow iJ}(T) \propto \frac{e^{-E_{i,J}/k_B T}}{Z(T)} (E_{i',J'} - E_{i,J}) \sum_{MM'\Omega} \langle iJM | \mu_\Omega | i'J'M' \rangle^2 \quad (4.14)$$

where $Z(T)$ is the partition function, $\langle iJM | \mu_\Omega | i'J'M' \rangle$ are the matrix elements of the dipole matrix defined as

$$\langle iJM | \mu_\Omega | i'J'M' \rangle = \iint \Psi_{i',M'}^{J'}(\mathbf{R}, \hat{\mathbf{r}})^* \mu_\Omega(\mathbf{R}, \hat{\mathbf{r}}) \Psi_i^{JM}(\mathbf{R}, \hat{\mathbf{r}}) d\mathbf{R} d\hat{\mathbf{r}} \quad (4.15)$$

where μ_Ω ($\Omega = 0, \pm 1$) are the components of $\boldsymbol{\mu}$ the dipole moment with origin at the center of mass of the complex and Ψ_i^{JM} is the wave function of the i th bound states. The components of the dipole moment can be expanded in term of $y_{\lambda\nu}^{\Lambda\Omega}(\hat{\mathbf{R}}, \hat{\mathbf{r}})$ functions restricted to terms with $\Lambda = 1$ and as $\boldsymbol{\mu}$ is a first-rank tensor,

$$\mu_\Omega(\mathbf{R}, \hat{\mathbf{r}}) = \sum_{\lambda\nu} \Theta_{\lambda\nu}^\Omega(\mathbf{R}) y_{\lambda\nu}^{1\Omega}(\hat{\mathbf{R}}, \hat{\mathbf{r}}) \quad (4.16)$$

Each term of the summation corresponds to a different multipole contribution in the atom-linear molecule van der Waals complex, such as : dipole moment of the linear molecule ($\lambda = 1, \nu = 0, \Lambda = 1$), charge-induced dipole ($\lambda = 0, \nu = 1, \Lambda = 1$), dipole-induced dipole ($\lambda = 1, \nu = 2, \Lambda = 1$), etc [110]. In the present work we will consider that the major contribution to the dipole of He–C₃N⁻ is the C₃N⁻ dipole moment and we will neglect other contributions.

Expanding the bound states in the usual space-fixed angular basis set

$$\Psi_i^{JM}(\mathbf{R}, \hat{\mathbf{r}}) = R^{-1} \sum_{jl} C_{jl}^{iJM}(\mathbf{R}) y_{jl}^{JM}(\hat{\mathbf{R}}, \hat{\mathbf{r}}), \quad (4.17)$$

one obtains for the dipole moment matrix elements the expression:

$$\begin{aligned} \langle i, J, M | \mu_\Omega | i', J', M' \rangle &= \sum_{l,j,j'} (-1)^{\Delta J' - M + 1 + 1} [(2J + 1)(2J' + 1)(2j + 1)(2j' + 1)]^{1/2} \\ &\times \begin{Bmatrix} j & J & l \\ J' & j' & 1 \end{Bmatrix} \begin{pmatrix} j & 1 & j' \\ 0 & 0 & 0 \end{pmatrix} \begin{pmatrix} J & 1 & J' \\ -M & m & M' \end{pmatrix} \int C_{jl}^{iJM}(\mathbf{R}) C_{j'l}^{i'J'M'}(\mathbf{R}) d\mathbf{R} \end{aligned} \quad (4.18)$$

from which arise the selection rules $\Delta l = 0$, $\Delta j = \pm 1$, and $\Delta J = 0, \pm 1$.

The calculated microwave spectrum represented in Figure 4.4 spans the $3 \times 10^{-4} - 27.602 \text{ cm}^{-1}$ region and contains a total of 1548 transitions among the 134 rovibrational levels of He–C₃N⁻ van der Waals complex. For this simulation, a temperature of 10 K was used and the zero energy was set at the rovibrational ground state. In general, these transitions are characterized by strong R-branches, less intense Q-branches and comparatively very weak P-branches. Based on our previous assignment of the bound states quantum numbers, an attempt to assign quantum numbers to the transitions inside the most intense band is presented in

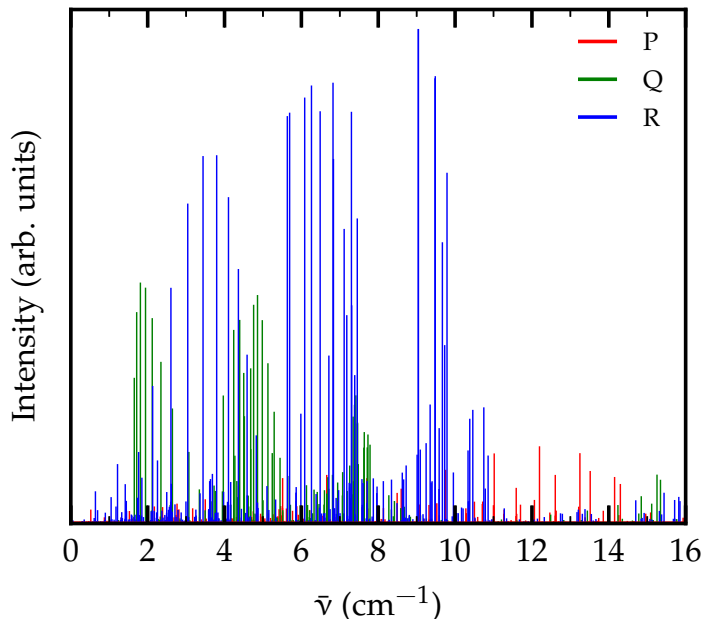


Figure 4.4: Rovibrational spectrum of He-C₃N⁻ at the temperature of 10 K

Table 4.3. As expected at the temperature of 10 K, the calculated transitions do not involve changes in the vibrational levels of the complex and then correspond to an almost pure rotational spectrum. Finally, it can be noted that as the energy increases, R-branches becomes increasingly closer showing the growing effect of centrifugal distortion.

4.5 Conclusion

A 2D analytical PES for collisional (de-)excitation of C₃N⁻ by He has been developed from a large set of high-level ab-initio calculations. Two equilibrium structures of the He-C₃N⁻ van der Waals complex were identified for a near T-shaped and a linear geometry. The corresponding dissociation energies are $D_e = 62.114$ cm⁻¹ and $D_e = 41.384$ cm⁻¹ respectively. Two saddle points connecting these minima were also identified.

The rovibrational energy levels of the complex were computed in the space-fixed frame using a mixed DVR-FBR approach based on a Sturmian DVR for the intermolecular distance and a coupled FBR angular basis set. The zero point level $E_0 = -27.641$ cm⁻¹ lies above the two saddle points of the PES. Consequently, the rovibrational ground state wave function is spread over the two minima. A rovibrational quantum numbers assignment was also attempted for the 134 bound states allowed by the PES by examining the contour plots of the wave functions and the energy levels spacings.

Finally, the He-C₃N⁻ rovibrational spectrum was predicted for a rotational tem-

Table 4.3: Predicted rotational transition frequencies and intensities for He-C₃N⁻ at a temperature of 10K

$J'_{K'_a K'_c} \leftarrow J_{K_a K_c}$	$\bar{\nu}$ (cm ⁻¹)	rel. Intensity	$J'_{K'_a K'_c} \leftarrow J_{K_a K_c}$	$\bar{\nu}$ (cm ⁻¹)	rel. Intensity
1 ₁₀ – 1 ₀₁	1.651	0.294	7 ₂₆ – 7 ₁₇	5.291	0.225
2 ₁₁ – 2 ₀₂	1.713	0.427	2 ₂₁ – 1 ₁₀	5.634	0.823
3 ₁₂ – 3 ₀₃	1.810	0.486	2 ₂₀ – 1 ₁₁	5.694	0.830
4 ₁₃ – 4 ₀₄	1.943	0.476	3 ₂₂ – 2 ₁₁	6.086	0.861
5 ₁₄ – 5 ₀₅	2.118	0.414	3 ₂₁ – 2 ₁₂	6.262	0.885
1 ₁₁ – 0 ₀₀	2.129	0.277	4 ₂₃ – 3 ₁₂	6.489	0.833
6 ₁₅ – 6 ₀₆	2.344	0.326	4 ₂₂ – 3 ₁₃	6.823	0.891
2 ₁₂ – 1 ₀₁	2.605	0.476	5 ₂₄ – 4 ₁₃	6.835	0.737
7 ₁₆ – 7 ₀₇	2.642	0.231	6 ₂₄ – 5 ₁₄	7.114	0.595
3 ₁₃ – 2 ₀₂	3.043	0.646	5 ₂₃ – 4 ₁₄	7.304	0.832
4 ₁₄ – 3 ₀₃	3.441	0.743	7 ₂₆ – 6 ₁₅	7.309	0.440
5 ₁₅ – 4 ₀₄	3.796	0.744	5 ₃₂ – 5 ₂₃	7.345	0.215
5 ₂₃ – 5 ₁₄	3.969	0.259	4 ₃₂ – 4 ₂₃	7.382	0.239
6 ₁₆ – 5 ₀₅	4.103	0.659	4 ₃₁ – 4 ₂₂	7.418	0.258
4 ₂₂ – 4 ₁₃	4.239	0.391	3 ₃₁ – 3 ₂₂	7.457	0.201
7 ₁₇ – 6 ₀₆	4.361	0.514	6 ₂₅ – 5 ₁₅	7.460	0.618
3 ₂₁ – 3 ₁₂	4.394	0.411	3 ₃₀ – 3 ₂₁	7.461	0.203
2 ₂₀ – 2 ₁₁	4.499	0.304	3 ₃₁ – 2 ₂₀	9.044	1.000
8 ₁₈ – 7 ₀₇	4.587	0.341	3 ₃₀ – 2 ₂₁	9.044	1.000
2 ₂₁ – 2 ₁₂	4.680	0.313	4 ₃₂ – 3 ₂₁	9.477	0.900
3 ₂₂ – 3 ₁₃	4.757	0.441	4 ₃₁ – 3 ₂₂	9.484	0.904
4 ₂₃ – 4 ₁₄	4.858	0.461	5 ₃₃ – 4 ₂₂	9.672	0.571
5 ₂₄ – 5 ₁₅	4.982	0.410	5 ₃₂ – 4 ₂₃	9.791	0.710

perature of 10 K. The strongest lines which are associated with almost pure rotational transitions belong to the R-branch.

Chapter 5

Rotational relaxation of C_3N^- by collisions with He

Contents

5.1	Introduction	62
5.2	Methods	63
5.2.1	The atom-linear rigid rotor coupled equations	63
5.2.2	PES and the matrix element of the potential	65
5.2.3	Inelastic boundary conditions and cross sections	66
5.2.4	Scattering calculations and rate coefficients	66
5.3	Results	68
5.4	Conclusions	73

Published

M. Lara-Moreno, T. Stoecklin, and P. Halvick. Rotational (de-)excitation of C_3N^- by collision with He atoms. *MNRAS*, 467(1):4174, 2017

5.1 Introduction

The determination of the anion molecular abundances requires the knowledge of accurate radiative and collisional rates with the most abundant interstellar species. Up to now, there is no experimental data available for these systems and the only theoretical collisional rate coefficients involving anions are those calculated for the $\text{CN}^- + \text{H}_2$ [32], $\text{C}_6\text{H}^- + \text{H}_2$, He [33] and $\text{C}_2\text{H}^- + \text{He}$ [112] collisions, although the latter has not been detected in the ISM yet. New studies dedicated to the collisional excitation and de-excitation of the remaining detected anions are then needed.

In the present study, we focus our interest on the next molecule of the $\text{C}_{2n-1}\text{N}^-$ ($n=1,2,3$) series, namely C_3N^- , which is a linear floppy molecule in its $^1\Sigma$ electronic ground state. C_3N^- has a large dipole moment and is remarkably stable, as the electron affinity of C_3N (4.305 ± 0.001 eV, [113]) is quite large. Because of the small value of its lowest vibrational frequency (203 cm^{-1}) [100], the use of the rigid monomer approximation above this threshold can lead to a 10 to 20 % inaccuracy of the calculated rotational excitation collisional rate coefficients as demonstrated in a recent study dedicated to He- C_3 [101]. This is the reason why the collisional rate coefficients will be given only for temperature below this threshold (330 K). In cold dense cloud where C_3N^- was detected, the most abundant collider is H_2 . However, the small rotational constant of C_3N^- ($B = 4852.8$ MHz) [100] makes the CC calculations with H_2 a very demanding task in terms of computational resources due to a large number of open channels involved. For the sake of simplicity in this chapter dedicated to rotational relaxation of C_3N^- , the H_2 molecule will be here replaced by He which is often used to model collisions with H_2 using a scaling law based on the ratio of the relative masses. This approximation works very well for some systems like $\text{H}_2\text{-CS}$ [114] but was also found to fail in many cases [115–119]. The reliability of this approximation for the case of C_3N^- will be eventually discussed in chapter 7.

Even for collisions involving He, some approximations must be used in order to obtain the collisional rate coefficients for highly excited rotational levels in a reasonable amount of computational time. Two of the most widely used approximations, the infinite order sudden (IOS) approximation [120, 121] and the uniform J-shifting (UJS) [122] will be tested here by comparison with CC results. To our knowledge, the latter approximation which is widely used for reactive collision, is scarcely, if ever, used to treat inelastic collisions. We will see however that it offers a good time saving (the calculation time is approximately divided by ten) while preserving a reasonable accuracy, which is not the case of the IOS approximation at low temperature.

In this chapter, the state-to-state rotational excitation rate coefficients $k_{j \rightarrow j'}$ for C_3N^- in collisions with He have been computed for the rotational levels $j \in [0,30]$ and $j' \in [0,30]$, and temperature ranging in the [1,300] K interval. The next sec-

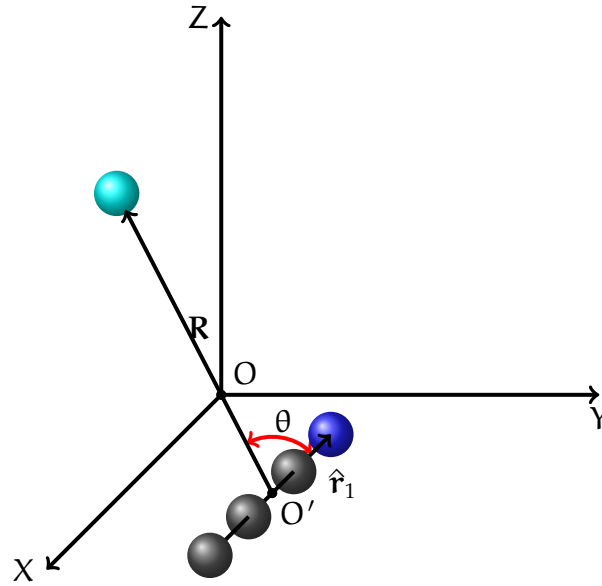


Figure 5.1: Space-fixed axes and Jacobi coordinates used to describe the interaction between He and C_3N^- . O' is the center of mass of C_3N^- and O is the center of mass of the whole system

tion provides a brief description of the methodology employed while the results are discussed in section 5.3 and the conclusions are given in section 5.4.

5.2 Methods

Following the work of Arthurs and Dalgarno [123], we firstly give a brief account of the rigid rotor space-fixed formulation of the time-independent Schrödinger equations for the scattering of a structureless He atom colliding with the C_3N^- molecule in its $^1\Sigma$ electronic ground state. In this section we will also introduce the main notation used throughout the chapter.

5.2.1 The atom–linear rigid rotor coupled equations

The space-fixed axis and the Jacobi coordinates used to describe the interaction between He and C_3N^- are shown in Figure 5.1. The Jacobi coordinates, namely the intermolecular vector \mathbf{R} and $\hat{\mathbf{r}}$ the coordinates of the C_3N^- molecular axis, are defined as follow:

$$\mathbf{R} = \mathbf{r}_{\text{He}} - \mathbf{r}_{O'} \quad (5.1)$$

$$\hat{\mathbf{r}} = \frac{\mathbf{r}_N - \mathbf{r}_C}{|\mathbf{r}_N - \mathbf{r}_C|} \quad (5.2)$$

The angle between them θ is defined as

$$\cos \theta = \hat{\mathbf{R}} \cdot \hat{\mathbf{r}} \quad (5.3)$$

with $\hat{\mathbf{R}} = \mathbf{R}R^{-1}$ where R is the modulus of the vector \mathbf{R} .

After separation of the center of mass motion the nuclear Hamiltonian of the system can be written as:

$$\mathbf{H}(\mathbf{R}, \hat{\mathbf{r}}) = -\frac{\hbar^2}{2\mu} \left[\frac{1}{R} \frac{\partial^2}{\partial R^2} R + \frac{\mathbf{l}^2}{R^2} \right] + \mathbf{H}_{\text{rot}}(\hat{\mathbf{r}}) + \mathbf{V}(\mathbf{R}, \hat{\mathbf{r}}) \quad (5.4)$$

where μ is the reduced mass of the system, $\mathbf{V}(\mathbf{R}, \hat{\mathbf{r}})$ is the BO interaction potential and \mathbf{l} is the orbital angular momentum operator associated with the relative movement of the He atom towards the center of mass of C_3N^- . \mathbf{H}_{rot} is the space-fixed rigid rotor Hamiltonian of C_3N^- whose eigenfunctions satisfy

$$\mathbf{H}_{\text{rot}}(\hat{\mathbf{r}}) Y_{jm_j}(\hat{\mathbf{r}}) = B j(j+1) Y_{jm_j}(\hat{\mathbf{r}}) \quad (5.5)$$

where B is the rotational constant of C_3N^- , $Y_{jm_j}(\hat{\mathbf{r}})$ is a spherical harmonic and j is the rotational quantum number associated with the rotation of C_3N^- . Since the total angular momentum

$$\mathbf{J} = \mathbf{j} + \mathbf{l} \quad (5.6)$$

must be conserved it is convenient to work in the coupled angular momentum representation, equation (4.8). These coupled angular momentum functions are eigenfunctions of not only the j^2 , \mathbf{l}^2 , \mathbf{J}^2 , J_z operators but also the parity operator \mathbf{P} (also called inversion operator) which has the effect of inverting all the coordinates in the center of mass

$$\mathbf{P} y_{jl}^{JM}(\hat{\mathbf{R}}, \hat{\mathbf{r}}) = y_{jl}^{JM}(-\hat{\mathbf{R}}, -\hat{\mathbf{r}}) = (-1)^{j+l} y_{jl}^{JM}(\hat{\mathbf{R}}, \hat{\mathbf{r}}) = \epsilon y_{jl}^{JM}(\hat{\mathbf{R}}, \hat{\mathbf{r}}) \quad (5.7)$$

The parity index $\epsilon = (-1)^{j+l}$ is one of the conserved quantities along with the total energy E , the total angular momentum $J\hbar$ and its space-fixed projection $M\hbar$.

The solution of the nuclear Schrödinger can be expanded as

$$\Psi_{jl}^{JM}(\mathbf{R}, \hat{\mathbf{r}}) = R^{-1} \sum_{j''=0}^{\infty} \sum_{l''=|J-j''|}^{J+j''} y_{j''l''}^{JM}(\hat{\mathbf{R}}, \hat{\mathbf{r}}) G_{j''l''}^{Jj'l}(\mathbf{R}) \quad (5.8)$$

Substituting equation (5.4) and (5.8) into the nuclear Schrödinger equation (1.9) and projecting onto the basis function $y_{j'l'}^{JM}$ we obtain the following set of coupled equations

$$\left[\frac{d^2}{dR^2} - \frac{l'(l'+1)}{R^2} + k_{j'}^2 \right] G_{j'l'}^{Jj'l}(\mathbf{R}) = \frac{2\mu}{\hbar^2} \sum_{j''l''} \langle j'l' | \mathbf{V} | j''l'' \rangle G_{j''l''}^{Jj'l}(\mathbf{R}) \quad (5.9)$$

where $k_{j'}$ is the channel wave number:

$$k_{j'}^2 = \frac{2\mu}{\hbar^2} [E - B j'(j'+1)] \quad (5.10)$$

and the matrix elements of the potential are given by

$$\langle j'l' | \mathbf{V} | j''l'' \rangle = \iint y_{j'l'}^{JM}(\hat{\mathbf{R}}, \hat{\mathbf{r}})^* \mathbf{V}(\mathbf{R}, \hat{\mathbf{r}}) y_{j''l''}^{JM}(\hat{\mathbf{R}}, \hat{\mathbf{r}}) d\hat{\mathbf{R}} d\hat{\mathbf{r}} \quad (5.11)$$

These set of coupled equations can be cast in the form of equation (1.25) by writing

$$\frac{d^2}{dR^2} G_{j'l'}^{Jj'l}(\mathbf{R}) = \sum_{j''l''} W_{j''l''}^{Jj'l'}(\mathbf{R}) G_{j''l''}^{Jj'l}(\mathbf{R}) \quad (5.12)$$

with

$$W_{j''l''}^{j'l'}(\mathbf{R}) = \frac{2\mu}{\hbar^2} \langle j'l' | \mathbf{V} | j''l'' \rangle + \frac{l'(l'+1)}{R^2} \delta_{l'l''} - k_j^2 \delta_{j'j''} \quad (5.13)$$

In the absence of any applied external field, these coupled equations are independent of the M quantum number as a result of the symmetry of the system by rotation of the collision plane.

5.2.2 PES and the matrix element of the potential

The PES used in the present work has been developed in the previous chapter using accurate CCSD(T) calculations. The functional form is defined as a direct product of radial and angular basis sets, the former being a sum of short-range and long-range contributions

$$\mathbf{V}(\mathbf{R}, \theta) = \sum_{\lambda} v_{\lambda}(\mathbf{R}) P_{\lambda}(\cos \theta) \quad (5.14)$$

$$v_{\lambda}(\mathbf{R}) = S(\mathbf{R}) f_{\lambda}^{\text{SR}}(\mathbf{R}) + [1 - S(\mathbf{R})] f_{\lambda}^{\text{LR}}(\mathbf{R}) \quad (5.15)$$

where the P_{λ} are normalized Legendre polynomials and f_{λ}^{SR} , f_{λ}^{LR} , $S(\mathbf{R})$ are respectively the short-range, the long-range and the switching radial functions. For the short-range radial functions, a cubic spline was employed while the long-range part of the PES was fitted to reciprocal power functions. A hyperbolic tangent, equation 4.2, is employed as the switching function $S(\mathbf{R})$. The interaction potential in terms of the space-fixed coordinates is obtained from equation (5.14) by means of the spherical harmonic addition theorem

$$P_{\lambda}(\cos \theta) = \frac{4\pi}{2\lambda + 1} \sum_{\nu=-\lambda}^{\lambda} Y_{\lambda\nu}^*(\hat{\mathbf{R}}) Y_{\lambda\nu}(\hat{\mathbf{r}}) \quad (5.16)$$

Hence

$$\mathbf{V}(\mathbf{R}, \hat{\mathbf{r}}) = 4\pi \sum_{\lambda\nu} \frac{v_{\lambda}(\mathbf{R})}{2\lambda + 1} Y_{\lambda\nu}^*(\hat{\mathbf{R}}) Y_{\lambda\nu}(\hat{\mathbf{r}}) \quad (5.17)$$

From expansion (5.17), the matrix elements of the potential, equation (5.11), are readily obtained using the techniques of angular momentum algebra

$$\langle j'l' | \mathbf{V} | j''l'' \rangle = \sum_{\lambda} v_{\lambda}(\mathbf{R}) f_{\lambda}(j'l'; j''l''; J) \quad (5.18)$$

where

$$\begin{aligned} f_{\lambda}(j'l'; j''l''; J) &= \frac{4\pi}{2\lambda + 1} \sum_{\nu} \int \int y_{j'l'}^{JM}(\hat{\mathbf{R}}, \hat{\mathbf{r}}) Y_{\lambda\nu}^*(\hat{\mathbf{R}}) Y_{\lambda\nu}(\hat{\mathbf{r}}) y_{j''l''}^{JM}(\hat{\mathbf{R}}, \hat{\mathbf{r}}) d\hat{\mathbf{R}} d\hat{\mathbf{r}} \\ &= (-1)^{j''+j'-J} [(2j''+1)(2j'+1)(2l''+1)(2l'+1)]^{1/2} \\ &\quad \times \left\{ \begin{matrix} J & l' & j' \\ \lambda & j'' & l'' \end{matrix} \right\} \begin{pmatrix} l'' & \lambda & l' \\ 0 & 0 & 0 \end{pmatrix} \begin{pmatrix} j'' & \lambda & j' \\ 0 & 0 & 0 \end{pmatrix} \end{aligned} \quad (5.19)$$

are the well-known Percival-Seaton coefficient [124]. Since $P_{\lambda}(\cos \theta)$ is totally symmetric with respect to the coordinate inversion, the integral (5.19) vanishes unless

$y_{j'l'}^{JM}$ and $y_{j''l''}^{JM}$ have the same parity ϵ .

5.2.3 Inelastic boundary conditions and cross sections

Solutions of equation (1.25) subject to the boundary conditions

$$G_{j'l'}^{Jl}(0) = 0$$

and

$$G_{j'l'}^{Jl}(R) \xrightarrow{R \rightarrow \infty} k_j^{-\frac{1}{2}} \left\{ \exp[-i(k_j R - l'\pi/2)] \delta_{jj'} \delta_{ll'} - \exp[i(k_j R - l'\pi/2)] S_{j'l',j'l'}^J \right\} \quad (5.20)$$

defines the matrix element of scattering matrix S^J . This unitary and symmetric matrix contains all the information concerning the contribution of the total angular momentum J to the scattering event. It is also convenient to introduce the transition matrix T^J which is related to S^J by

$$T^J = \mathbb{1} - S^J \quad (5.21)$$

and from which the opacity functions (average transition probabilities) are defined by

$$P_{j \rightarrow j'}^J = \frac{1}{2j+1} \sum_{l=|J-j|}^{J+j} \sum_{l'=|J-j'|}^{J+j'} |T_{j'l',j'l'}^J|^2 \quad (5.22)$$

The state selected integral cross section is then obtained by summing the opacity functions over all possible values of J

$$\sigma_{j \rightarrow j'} = \frac{\pi}{k_j^2} \sum_J (2J+1) P_{j \rightarrow j'}^J \quad (5.23)$$

In practice, the summation (5.23) is truncated at a given value J_{\max} for which the cross section is checked to be converged within a chosen convergence threshold.

5.2.4 Scattering calculations and rate coefficients

The close coupled equations of the He-C₃N⁻ colliding system are solved in the space-fixed frame using the log-derivative propagator [43] implemented in the NEWMAT code [125]. Full CC calculations were performed for collisional energy E_c ranging from 0.1 to 2000 cm⁻¹. All the calculations were made using the rigid monomer approximation and the rotational constant value $B = 0.1618$ cm⁻¹. The convergence of the quenching cross section as a function of both the maximum intermolecular distance and the total angular momentum was checked for each collisional energy. The highest rotational level of C₃N⁻ used in any calculation was $j = 40$. The strong charge-induced dipole and dipole-induced dipole long-range potential required propagating up to relatively large intermolecular distances and the large reduced mass of the system required up to 145 value of J to reach convergence

for the highest collision energies considered in the calculations. The propagation was carried out up to a maximum distance of $150 a_0$ for the lowest energies and the convergence was checked as a function of propagator step size.

The thermally averaged de-excitation rate coefficients are then calculated as follows:

$$k_{j \rightarrow j'} = \sqrt{\frac{8}{\pi \mu k_B^3 T^3}} \int_0^\infty \sigma_{j \rightarrow j'}(E_c) e^{-\left(\frac{E_c}{k_B T}\right)} E_c dE_c, \quad j > j' \quad (5.24)$$

The detailed balance relationship is then used to obtain the excitation rate:

$$k_{j' \rightarrow j}(T) = \frac{2j+1}{2j'+1} e^{-\left(\frac{\epsilon_j - \epsilon_{j'}}{k_B T}\right)} k_{j \rightarrow j'}(T), \quad j > j' \quad (5.25)$$

where ϵ_j and $\epsilon_{j'}$ are respectively the energies of the rotational level j and j' . This straightforward method was used to obtain all the state-to-state rate coefficients $k_{j \rightarrow j'}$ among the first 16 rotational levels of C_3N^- , namely $0 \leq j \leq 15$ and $0 \leq j' \leq 15$.

As mentioned in the introduction, owing to the small value of the rotational constant of C_3N^- , the CC calculations become more and more difficult and computationally demanding for highly excited rotational levels. The introduction of some approximation was necessary.

The rotating C_3N^- molecule, in its ground electronic state, is well described by a Hund's case (b) wave function. When the rotational energy spacing can be neglected compared to the collision energy, the IOS can be safely used. In such a case and for a Hund's case (b) $^1\Sigma$ linear molecule, it was demonstrated by several authors [120, 121] that the rotational rate coefficients $k_{j \rightarrow j'}^{IOS}(T)$ can be extrapolated as follows:

$$k_{j \rightarrow j'}^{IOS}(T) = (2j'+1) \sum_L \begin{pmatrix} j' & j & L \\ 0 & 0 & 0 \end{pmatrix}^2 k_{0 \rightarrow L}(T) \quad (5.26)$$

where $k_{0 \rightarrow L}(T)$ are the rotational excitation rate coefficients previously calculated for the transitions from the fundamental level $j = 0$ to the level $j' = L$. We select for these reference rate coefficients those obtained from equation (5.24) using our accurate CC calculations described above. This approach was recently used by Lique et al. [126] to determine the rotational excitation rate coefficient of OH^+ by collision with H.

Another way to obtain the state-to-state rate coefficients with a reduced computational effort is to perform accurate CC calculations for selected values of the total angular momentum number J and then obtain the missing partial wave contributions using the UJS procedure [122]. This method, which is widely used for computing reactive collision rate coefficients, offers a very good level of accuracy when compared with exact calculations as shown for example in the recent study of the $H + CH^+$ reaction [127]. In the present work, the CC calculations were performed for the following set of values $\{0, 5, 10, 15, 20, 25, 30, 40, 50, 60, 70\}$ of the total angular momentum. The calculation of the UJS rate coefficients was made by

the summation of the partial waves running from $J = 0$ up to 120, see appendix B for more details.

5.3 Results

A few examples of rotational excitation and de-excitation cross sections of C_3N^- colliding with He are represented as a function of collision energy respectively in Figure 5.2 and 5.3.

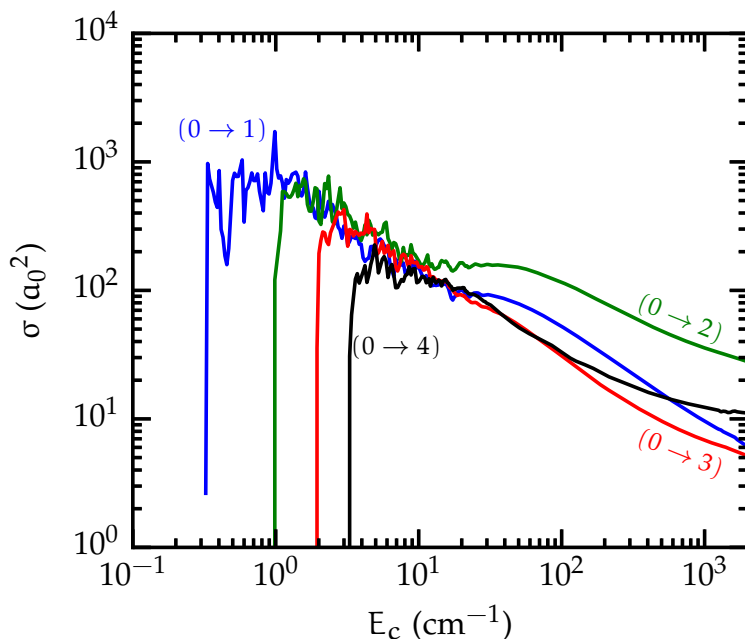


Figure 5.2: Rotational excitation cross section of $\text{C}_3\text{N}^- (j = 0)$ in collisions with He. The curves are labeled by $j \rightarrow j'$.

Many resonances associated with the formation of quasi-bound states of the $\text{He}-\text{C}_3\text{N}^-$ complex can be seen in the lower energy part of these figures. This resonance region extends as usual roughly up to a collision energy equal to the van der Waals well depth (30 cm^{-1}). For higher energies, a propensity to favor $|\Delta j|=2$ is observed. This approximate propensity rule is a common feature of nearly homonuclear molecules for which the parity is weakly broken. Even if the global minimum is close to a T-shape structure, this near symmetry is not obvious when looking at the contour plot of the PES (Figure 4.1) whereas it appears clearly in Figure 4.2 where the Legendre expansion coefficients of the PES associated with even values of l are seen to be always larger than those corresponding to the odd values of l .

An explanation of this propensity rule based on semi-classical theory was proposed long ago by McCurdy and Miller [128]. Within this approach, the cross sections for odd Δj transitions are reduced as a result of destructive interferences. These authors also showed that if the odd anisotropy of the PES is large enough, then

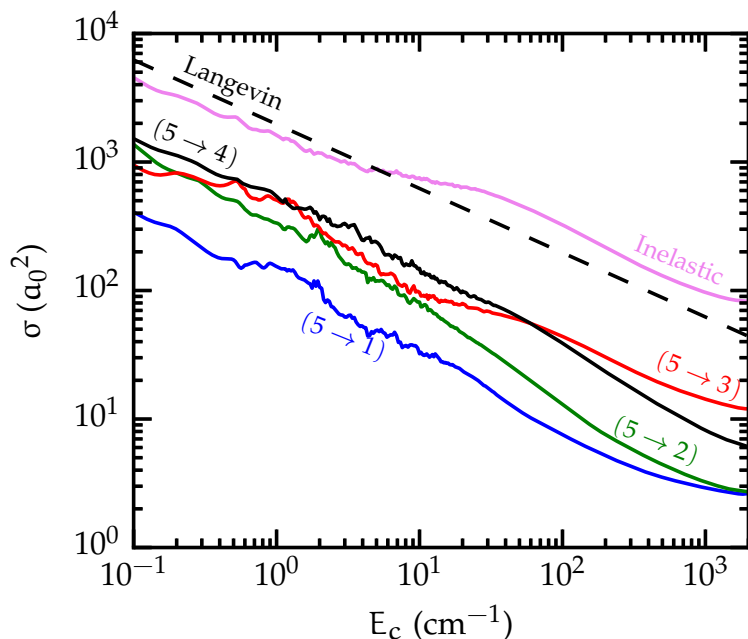


Figure 5.3: Rotational de-excitation cross section of C_3N^- ($j = 5$) in collisions with He. The curves are labeled by $j \rightarrow j'$. The dashed line corresponds to the Langevin cross section.

an inversion of the propensity rule can take place. In the present case this inverse propensity rule can be seen in Figure 5.4, for transitions with the largest $|\Delta j|$. Similar propensity rules have been observed by Wernli et al. [129] for HC_3N in collisions with H_2 . Interestingly, these authors showed that this strong propensity rule can lead to population inversion when LTE conditions are not met, even if hyperfine effects are neglected.

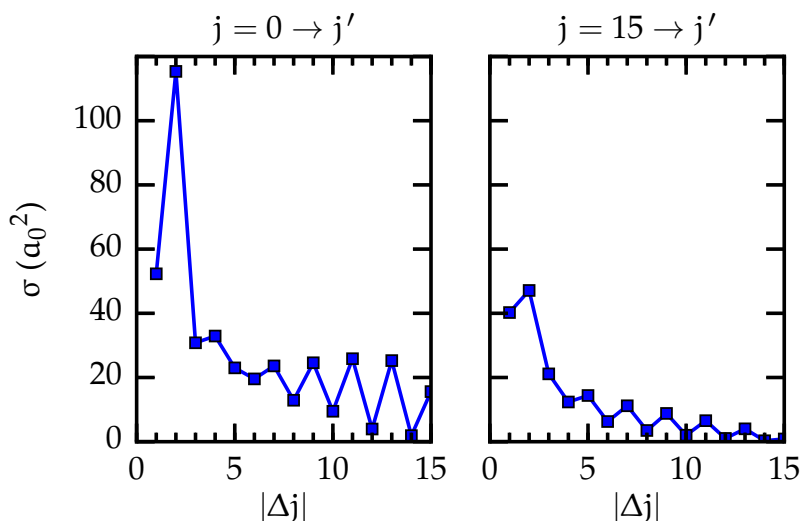


Figure 5.4: Rotational excitation (left panel) and de-excitation (right panel) cross section of C_3N^- in collision with He at $E_c = 100 \text{ cm}^{-1}$ as a function of $\Delta j = j - j'$

For barrierless ion-neutral collisions, the low collision energy de-excitation cross sections can be estimated using Langevin capture theory [130, 131], which predicts that the cross section decays as $E_c^{-1/2}$. Figure 5.3 also shows a comparison between our results to those given by the Langevin capture model, based on the long-range charge-induced dipole interaction:

$$\sigma(E_c) = \pi \left(\frac{2\alpha}{E_c} \right)^{\frac{1}{2}} \quad (5.27)$$

where α is the polarizability of the helium atom. As can be seen in this figure the curves associated with the rotational de-excitation cross sections decrease almost monotonously and clearly follow the Langevin's law at low collision energy.

The calculated CC cross sections were used to obtain rotational excitation and de-excitation rate coefficients for the first sixteen levels of C_3N^- in the temperature interval [1,300] K. Some of these results are shown in Figure 5.5. Apart from the propensity rules discussed before, the de-excitation rate coefficients remain almost constant at low temperature, as predicted by the Langevin's law. On the other hand, the excitation rate coefficients increase monotonically as the temperature increases.

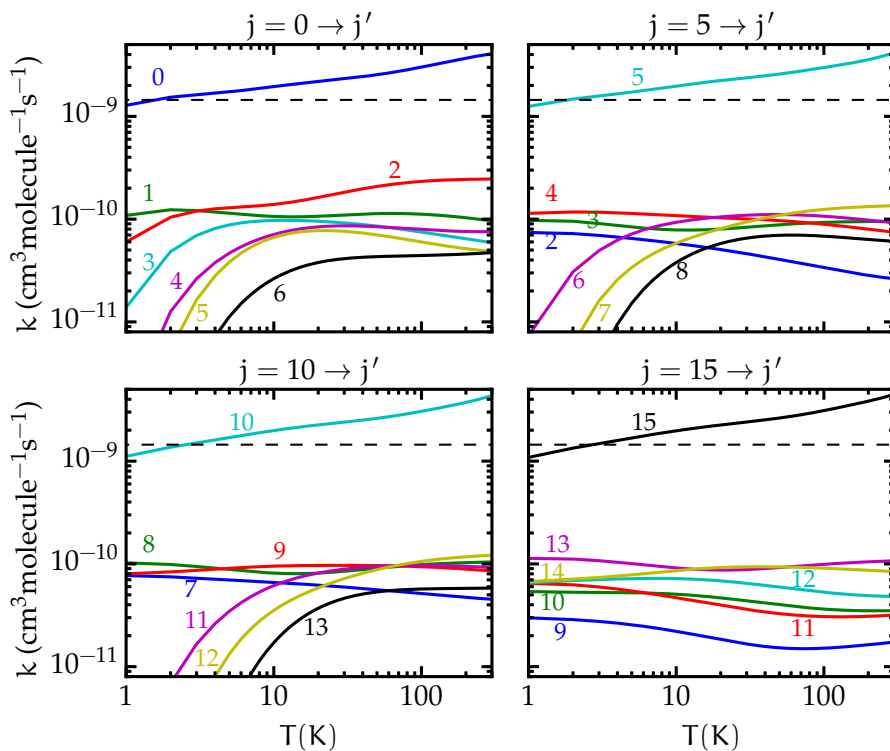


Figure 5.5: Rotational excitation and de-excitation rate coefficients of C_3N^- ($j = 0, 5, 10, 15$) in collision with He as a function of temperature. The curves are labeled by the final state in the transition $j \rightarrow j'$. Dashed lines correspond to the Langevin capture model rate coefficient.

As discussed in section 5.2, two approximations were tested with the aim of obtaining a larger set of the state-to-state rate coefficients. Our results are compared

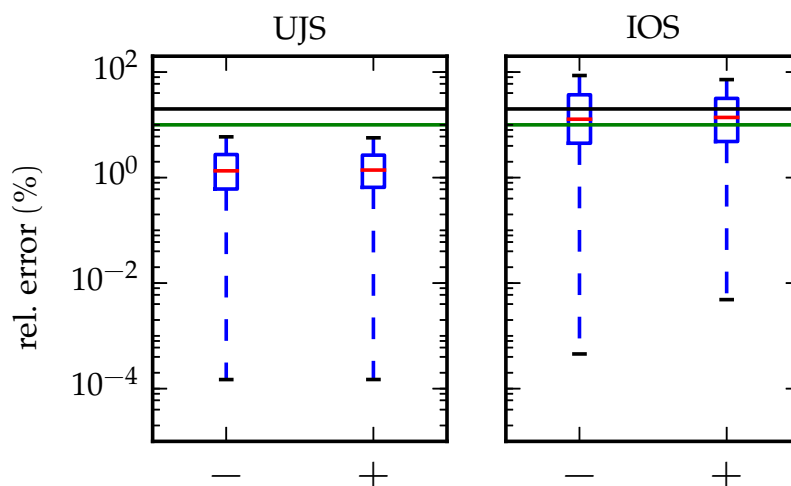


Figure 5.6: IOS and UJS relative errors for the de-excitation (–) and excitation (+) rate coefficients. Solid green and black lines highlight the 10% and 20% relative error respectively. The error populations are depicted by Tukey boxplots [132, 133]. The solid red line indicates the median (i. e. the second quartile) of the error population, the bottom and top of the box are the first and third quartiles respectively, and the end of the dashed lines are distant from the box by 1.5 times the height of the box.

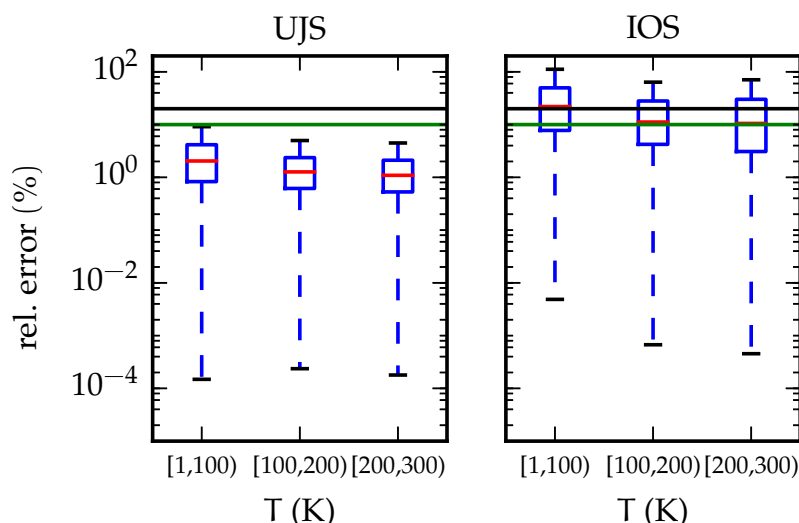


Figure 5.7: IOS and UJS relative error for selected temperature ranges. See the caption of Fig. 5.6 for the details of data representation.

to the CC calculations in Figure 5.6 and 5.7. As can be seen in these figures, the UJS approximation gives always a better agreement than IOS with the CC calculations for both excitations and de-excitation rate coefficients. The UJS relative error for $\sim 99\%$ of the transitions tested is less than 10% while for IOS, $\sim 50\%$ of the transitions tested show relative error ranging between 5% and 30%. Despite these differences in accuracy, it is found that both methods are able to reproduce the propensity rules

mentioned before. The relative errors are seen to be larger at low temperature where resonances play an important role and are the largest for large $|\Delta j|$ transitions which are associated with the smallest rate coefficients. Consequently, the use of one or the other of these two approximations is expected to impact only marginally the calculated molecular abundance of C_3N^- using these rates. The UJS was chosen and used to complement the calculations of the state-to-state set of rate coefficients among the first 31 rotational levels of C_3N^- in the temperature interval [1,300] K. A small set of rate coefficients is provided in Table 5.1.

Table 5.1: He- C_3N^- collisional rate coefficients $k_{j \rightarrow j'}$ in $\text{cm}^3 \text{molecule}^{-1} \text{s}^{-1}$ for various temperature values. Powers of ten are denoted in parenthesis.

j	j'	T = 10 K	T = 50 K	T = 100 K	T = 300 K
0	1	1.06(-10)	1.13(-10)	1.12(-10)	1.07(-10)
0	2	1.39(-10)	2.08(-10)	2.33(-10)	2.40(-10)
0	3	9.69(-11)	8.56(-11)	7.48(-11)	6.83(-11)
0	4	7.04(-11)	8.42(-11)	7.91(-11)	7.67(-11)
0	5	6.60(-11)	7.02(-11)	5.99(-11)	5.45(-11)
5	2	5.80(-11)	4.05(-11)	3.36(-11)	3.03(-11)
5	3	7.85(-11)	8.81(-11)	9.30(-11)	9.43(-11)
5	4	1.08(-10)	9.68(-11)	8.92(-11)	8.38(-11)
5	6	9.30(-11)	1.11(-10)	1.07(-10)	1.02(-10)
10	7	6.61(-11)	5.61(-11)	5.14(-11)	4.88(-11)
10	8	8.13(-11)	9.08(-11)	9.85(-11)	1.01(-10)
10	9	9.51(-11)	9.63(-11)	9.39(-11)	9.13(-11)
10	11	6.14(-11)	9.45(-11)	9.70(-11)	9.61(-11)
10	12	3.51(-11)	8.78(-11)	1.06(-10)	1.13(-10)
15	13	9.14(-11)	9.21(-11)	9.92(-11)	1.03(-10)
15	14	8.61(-11)	9.35(-11)	9.08(-11)	8.84(-11)
15	16	4.33(-11)	8.61(-11)	9.00(-11)	8.98(-11)
15	17	2.22(-11)	7.63(-11)	9.58(-11)	1.04(-10)
20	18	8.48(-11)	9.14(-11)	9.79(-11)	1.01(-10)
20	19	7.62(-11)	8.90(-11)	8.78(-11)	8.60(-11)
20	21	3.12(-11)	7.76(-11)	8.41(-11)	8.48(-11)
20	22	1.33(-11)	6.88(-11)	8.88(-11)	9.81(-11)
25	23	8.45(-11)	8.99(-11)	9.57(-11)	9.98(-11)
25	24	7.04(-11)	8.23(-11)	8.34(-11)	8.27(-11)
25	26	2.20(-11)	6.77(-11)	7.74(-11)	7.98(-11)
25	27	7.26(-12)	5.83(-11)	8.00(-11)	9.12(-11)
30	26	5.24(-11)	3.81(-11)	3.51(-11)	3.53(-11)

Continued on next page

Table 5.1 – *Continued from previous page*

j	j'	T = 10 K	T = 50 K	T = 100 K	T = 300 K
30	27	7.43(-11)	5.88(-11)	5.36(-11)	5.15(-11)
30	28	9.25(-11)	8.90(-11)	9.73(-11)	1.06(-10)
30	29	9.29(-11)	8.88(-11)	8.83(-11)	8.79(-11)

5.4 Conclusions

Full rigid rotor CC calculations were performed for C_3N^- in collisions with He using a two dimensional PES based on supermolecular accurate ab-initio calculations. This first set of calculations was done for the C_3N^- rotational levels $j \in [0, 15]$. A strong $|\Delta j| = 2$ propensity rule was found while for large Δj , the inverse propensity rule was observed, i.e. odd $\Delta j >$ even Δj . Two approximate methods, namely the IOS and UJS approximations, were tested to complement this first set of rate coefficients for higher rotational levels. The UJS was found to give the best agreement with exact calculations while dividing computational time by more than a factor ten. Consequently, the rate coefficients for transitions involving the rotational levels $j \in [16, 30]$ were calculated using this approximation. The relative error obtained for UJS is less than 10% for $\sim 99\%$ of the checked data. In the end, a complete set of state-to-state rate coefficients for rotational excitation and de-excitation among the first 31 rotational levels of C_3N^- was obtained for temperatures $T \in [1, 300]$ by combining CC calculations and the UJS approximation.

Chapter 6

Interaction of rigid C_3N^- with H_2

Contents

6.1	Introduction	76
6.2	Ab-initio calculations	76
6.3	Analytical representation of PES	77
6.3.1	Features of the PES	78
6.3.2	Long-range intermolecular forces	79
6.4	Bound states	82
6.4.1	Vibrational levels and wave functions	83
6.4.2	Para and ortho states	90
6.5	Conclusion	91

6.1 Introduction

Analysis of the C_3N^- astronomical emission spectra requires the knowledge of accurate radiative and collisional rates with the most abundant interstellar species, H_2 . Calculation of such collisional rates relies on accurate PES of the two interacting molecules. For that reason in the present chapter, we will develop a new PES which will be eventually used for determining the rotational excitation and de-excitation rate coefficients of C_3N^- by collisions with H_2 .

in their ground state, both C_3N^- and H_2 are linear closed-shell molecules and are well described by a mono-determinantal electronic wave function. This makes the coupled cluster method a reliable approach for calculating the interaction potential between these two molecules. The explicitly correlated CCSD(T)-F12 has been shown to provide an accurate description of the interaction between charged and neutral molecules [134, 135]. Furthermore, this method have been widely used to map multidimensional PES with a reduced computational cost, since the accuracy of the F12 correction with a triple-zeta basis set is comparable to the accuracy of the quintuple-zeta quality coupled cluster without the F12 correction.

In the second part of this chapter, as the first application of the new PES, we compute the bound states energy levels as well as other spectroscopic constants for the $H_2-C_3N^-$ van der Waals complex.

6.2 Ab-initio calculations

We have used the CCSD(T)-F12 approach and the aug-cc-pVTZ basis set to calculate the $H_2-C_3N^-$ interaction energies on a four dimensional grid of points expressed in the body-fixed Jacobi coordinates, as defined in Figure 6.1. Both monomers are assumed to be linear rigid rotors. Since C_3N^- is a long molecule, the interaction energy is strongly anisotropic for small intermonomer separation. Therefore a large density of ab-initio points was necessary. A total number of 28339 geometries were calculated. In this fine grid, the Jacobi coordinates vary as follow: R goes from 2 to 50 a_0 , θ_1 from 0° to 90° , θ_2 from 0° to 180° , ϕ from 0° to 180° .

For every $H_2 - C_3N^-$ configuration, the H_2 bond length was set to $r_{H-H} = 1.448736 a_0$ which correspond to the vibrationally averaged bond length in the rovibrational ground state. The C_3N^- bond lengths were set to equilibrium values obtained from CCSD(T)/aug-cc-pV5Z calculations [100], namely, $r_{C_1-C_2} = 2.3653 a_0$, $r_{C_2-C_3} = 2.5817 a_0$, and $r_{C_3-N} = 2.2136 a_0$. The BSSE was corrected by means of the counterpoise procedure [104] applied to the rigid monomer case. All calculations have been carried out with the MOLPRO package [34].

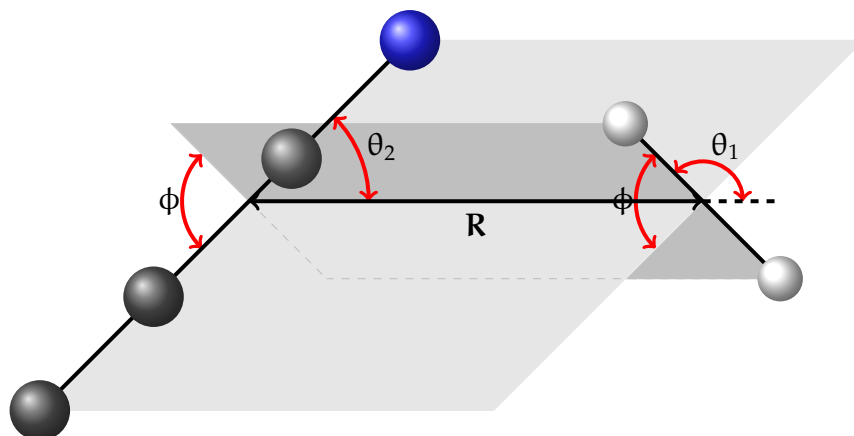


Figure 6.1: Body-fixed Jacobi coordinates used to describe the interaction between H_2 and C_3N^- .

6.3 Analytical representation of PES

The functional form used to fit the ab-initio energy points is defined as the sum of the two terms f_{SR} and f_{LR} associated with the short-range and long-range contributions, respectively.

$$V(R, \theta_1, \theta_2, \phi) = S(R)f_{SR}(R, \theta_1, \theta_2, \phi) + [1 - S(R)]f_{LR}(R, \theta_1, \theta_2, \phi) \quad (6.1)$$

where the switching function $S(R)$ is defined by equation (4.2). Each term in equation (6.1) is expanded over a product of normalized associated Legendre polynomials P_l^m [136] and cosine functions.

$$f(R, \theta_1, \theta_2, \phi) = \sum_{l_1 l_2 m} v_{l_1, l_2}^m(R) P_{l_1}^m(\cos \theta_1) P_{l_2}^m(\cos \theta_2) \cos(m\phi) \quad (6.2)$$

In the latter expression, only even values of l_1 must be included because the interaction potential is symmetric with respect to the permutation of the two H atoms.

For each point R_i of the radial grid, the short-range coefficients $[v_{l_1, l_2}^m(R_i)]_{SR}$ are obtained through a weighted linear least squares fit of equation (6.2) to the ab-initio data. In this step, we use an energy dependent hyperbolic tangent weighting function $w(E)$, see equation (4.6), in order to obtain the smallest fitting errors in the low energy region of the PES. Additionally, an energy cut-off was set at $40\,000\text{ cm}^{-1}$ in order to discard the extremely large energies arising from the overlap between monomers at short distances for θ_2 close to 0° or 180° . Then a cubic spline interpolation was used to obtain the short-range radial functions $[v_{l_1, l_2}^m(R)]_{SR}$.

The long-range coefficients $[v_{l_1, l_2}^m(R_i)]_{LR}$ are obtained by the same process, but using only the energy points with $R_i \geq 15\ a_0$. The long-range radial functions are then obtained by a linear least squares fitting of the following expression

$$[v_{l_1, l_2}^m(R)]_{LR} = \sum_{k=3}^8 \frac{t_k(\beta R)}{R^k} C_{lk} \quad (6.3)$$

where t_k is the Tang-Toennies damping function, equation (4.5)

A total of 243 angular functions $\{l_1 \in [0, 6], l_2 \in [0, 18], m \in [0, 4]\}$ were needed to describe the strong anisotropy of the short range contribution. But only 25 angular functions $\{l_1 \in [0, 2], l_2 \in [0, 6], m \in [0, 2]\}$ were needed for the accurate description of the long range part. The non-linear parameters as well as those of the weighting function, equation (4.6), were determined by the trial and error method, leading to the following values: $A_0 = 1.8 a_0^{-1}$, $R_0 = 20 a_0$, $\beta = 6.0 a_0^{-1}$, $w_{\min} = 0.001$, $w_{\max} = 200$, $E_0 = 4000 \text{ cm}^{-1}$, and $\alpha = 1.73 \times 10^{-3} \text{ cm}^{-1}$.

The quality of the fitting procedure was checked by means of the RMS error. The RMS error for negative energies is 0.01 cm^{-1} while for energies in the range $0 \leq E \leq 5000 \text{ cm}^{-1}$ it is 0.06 cm^{-1} . For energies above 5000 cm^{-1} the RMS error increases more or less linearly with the energy. For instance, for energies in the range $5000 \leq E \leq 10000 \text{ cm}^{-1}$ the RMS error is 59.6 cm^{-1} while the relative RMS error is 0.66 %. We would like to point out that these larger errors are located at high energy in the short-range repulsive region of the PES and are expected to have no consequences on the collisional dynamics at low temperatures which is the main purpose of the present PES.

6.3.1 Features of the PES

Four types of stationary points have been found in the PES of the $\text{H}_2\text{-C}_3\text{N}^-$ system. These are the global minima MIN1, the secondary minima MIN2, and the submerged saddle points SP1 and SP2. All minima have a colinear structure and all saddle points have a planar structure, as shown in Table 6.1. In the MIN1 minima, the C-end of the C_3N^- molecule is pointing towards the H_2 molecule, while it is the N-end in the case of the MIN2 minima.

Table 6.1: Stationary points of the $\text{H}_2\text{-C}_3\text{N}^-$ 4D PES. The angle ϕ is not defined (ND) for the colinear structures.

Point	R (a_0)	θ_1 (deg.)	θ_2 (deg.)	ϕ (deg.)	D_e (cm^{-1})
MIN1	9.39	0 or 180	180	ND	769.75
MIN2	8.89	0 or 180	0	ND	561.77
SP1	6.42	173.11	77.81	0	348.93
SP2	6.00	97.65	81.14	0	249.52

Since the potential energy is symmetric under the exchange of the two H atoms, there are two equivalent stationary points for each type. For the MIN1 and the MIN2 types, the two equivalent stationary points are related by the symmetry operation $\theta_1 \mapsto \theta_1 \pm \pi$. For the SP1 and SP2 types, the two equivalent stationary points are related by the symmetry operation $\theta_1 \mapsto \pi - \theta_1$ and $\phi \mapsto \phi \pm \pi$. Both types of saddle points correspond to the transition states for the interconversion between a MIN1 and a MIN2 minima. In the case of the SP2 points, this interconversion is

accompanied by a permutation of H atoms. There is no saddle point allowing a direct path from a MIN1 minimum to the other MIN1 minimum since the rotation of H_2 is blocked by a large potential barrier. The same holds true for the MIN2 minima. The important feature of the PES is thus the strong anisotropy with respect to the orientation of both monomers. The mentioned features of the present PES are depicted in Figure 6.2.

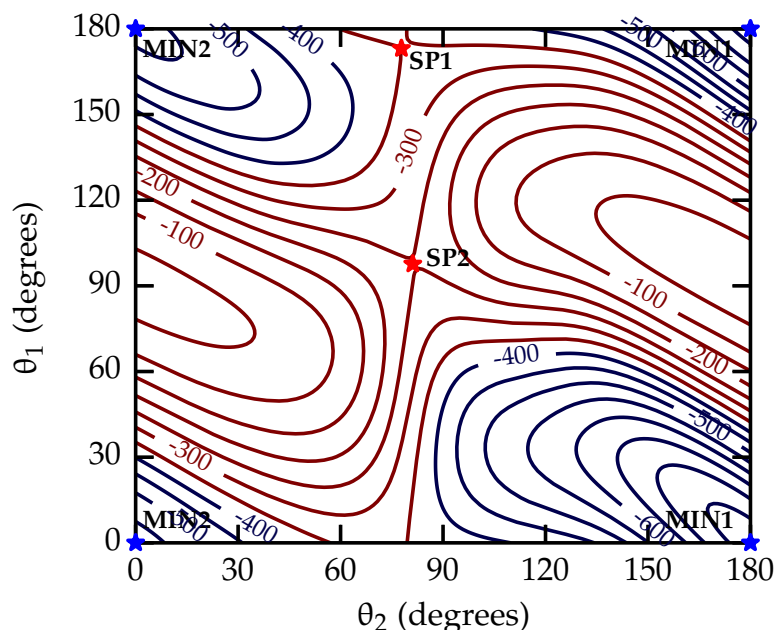


Figure 6.2: 2D contour plot of the $H_2-C_3N^-$ PES for $\phi = 0^\circ$ and R relaxed. Contour lines are equally spaced by 50 cm^{-1}

6.3.2 Long-range intermolecular forces

The contributions to the long-range interaction potential have been investigated in order to get a better understating of the nature of the interaction in the asymptotic region as well as to validate the extrapolation capabilities of the present PES. In this approach the potential energy is defined as the sum of three contributions: electrostatic, induction and dispersion,

$$V = V_{\text{elec}} + V_{\text{ind}} + V_{\text{disp}} \quad (6.4)$$

where each term is expanded as in equation (6.2). Expressions for the leading expansion coefficients are shown in Table 6.2. These expressions have been obtained through the application of the intermolecular forces theory developed by Buckingham [137].

Table 6.2: Asymptotic form of the leading expansion coefficients as defined in equation (6.2) for long-range interaction contributions. q is the charge, μ and Θ are the dipole and quadrupole moment respectively. $\alpha = (\alpha_{\parallel} + 2\alpha_{\perp})$ and $\Delta\alpha = (\alpha_{\parallel} - \alpha_{\perp})$ are the isotropic and anisotropic polarizabilities where α_{\parallel} and α_{\perp} are the dipole polarizabilities. A_{\parallel} and A_{\perp} are the dipole-quadrupole polarizabilities and U the ionization energies. Subscripts a and b refer to the molecules H_2 and C_3N^- respectively.

v_{l_1, l_2}^m	Electrostatic	Induction	Dispersion
v_{00}^0		$-\frac{\alpha^a q_b^2}{R^4} - \frac{1}{3} \frac{\mu_b^2 \Delta\alpha_a}{R^6} - \frac{\mu_b^2 \alpha_a}{R^6} + \dots$	$-\frac{3}{U_a + U_b} \frac{U_a U_b}{R^6} \frac{\alpha_a \alpha_b}{R^6} + \dots$
v_{01}^0		$-\frac{4\sqrt{3}}{3} \frac{\alpha_a \mu_b q_b}{R^5} - \frac{12\sqrt{3}}{5} \frac{\alpha_a \mu_b \Theta_b}{R^7} + \dots$	$-\frac{6\sqrt{3}}{5} \frac{U_a U_b}{U_a + U_b} \frac{\alpha_a (A_{\parallel} + 2A_{\perp})_b}{R^7} + \dots$
v_{02}^0		$-\frac{6\sqrt{5}}{5} \frac{\alpha_a q_b \Theta_b}{R^6} - \frac{2\sqrt{5}}{5} \frac{\alpha_a \mu_b^2}{R^6} - \frac{\sqrt{5}}{5} \frac{\Delta\alpha_a \mu_b^2}{R^6} + \dots$	$-\frac{\sqrt{5}}{5} \frac{U_a U_b}{U_a + U_b} \frac{\alpha_a \Delta\alpha_b}{R^6} + \dots$
v_{20}^0	$\frac{2\sqrt{5}}{5} \frac{q_b \Theta_a}{R^3}$	$-\frac{2\sqrt{5}}{15} \frac{\alpha_a q_b^2}{R^4} - \frac{4\sqrt{5}}{15} \frac{\alpha_a q_b \mu_b}{R^5} - \frac{\sqrt{5}}{15} \frac{\Delta\alpha_a \mu_b^2}{R^6} + \dots$	$-\frac{\sqrt{5}}{5} \frac{U_a U_b}{U_a + U_b} \frac{\alpha_b \Delta\alpha_a}{R^6} + \dots$
v_{21}^0	$\frac{2\sqrt{15}}{5} \frac{\Theta_a \mu_b}{R^4}$	$-\frac{4\sqrt{15}}{45} \frac{\Delta\alpha_a q_b \mu_b}{R^5} + \dots$	
v_{21}^1	$-\frac{4\sqrt{5}}{5} \frac{\Theta_a \mu_b}{R^4}$	$-\frac{2\sqrt{15}}{15} \frac{\Delta\alpha_a q_b \mu_b}{R^5} + \dots$	
v_{22}^0	$\frac{15 \Theta_a \Theta_b}{5 R^5}$	$-\frac{2}{5} \frac{\Delta\alpha_a \mu_b^2}{R^6} - \frac{4}{5} \frac{\Delta\alpha_a q_b \Theta_b}{R^6} + \dots$	
v_{22}^1	$-\frac{16 \Theta_a \Theta_b}{5 R^5}$	$\frac{8}{15} \frac{\Delta\alpha_a \mu_b^2}{R^6} + \frac{12}{5} \frac{\Delta\alpha_a q_b \Theta_b}{R^6} + \dots$	
v_{22}^2	$\frac{4 \Theta_a \Theta_b}{5 R^5}$	$-\frac{4}{15} \frac{\Delta\alpha_a \mu_b^2}{R^6} + \dots$	

Multipole moments and polarizabilities needed in the analytic formulation of the long-range interactions are shown in Table 6.3. They were calculated using the finite field method implemented in MOLPRO [34] at the CCSD(T)/aug-cc-pVQZ level. Also shown in Table 6.3 are the ionization energies of H_2 and C_3N^- . The ionization energy of C_3N^- was considered equal to the electron affinity of its neutral counterpart.

Table 6.3: Molecular properties of H_2 and C_3N^- needed in the calculation of long range interactions, see Table 6.2. The multipole moments and polarizabilities values have been calculated with the origin at the center of mass. All values are in atomic units

	μ	Θ	α_{\parallel}	α_{\perp}	A_{\parallel}	A_{\perp}	U
H_2	0	0.48	6.72	4.74	0	0	0.64 ^a
C_3N^-	1.38	-19.09	83.93	38.1	115.97	79.29	0.16 ^b

a. Shiner et al. [138]
b. Yen et al. [113]

Figure 6.3 shows a comparison between the long-range fitted coefficients of the PES equation (6.3) and the same coefficients obtained by the formulas of Table 6.2.

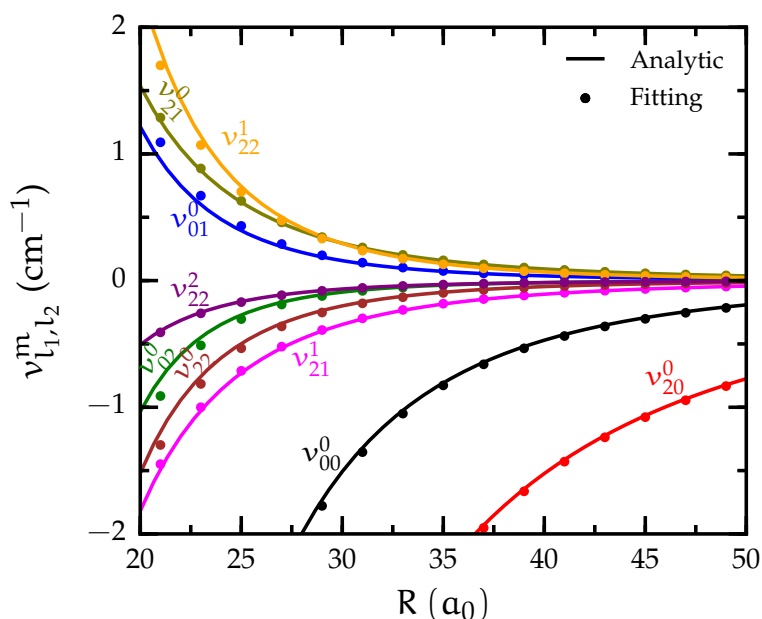


Figure 6.3: Comparison between the expansion coefficients, equation (6.2), obtained from the fitting of the ab-initio points (solid circles) and those obtained analytically (solid lines), using the expressions in Table 6.2.

A very good agreement is observed, although there are small differences at short distances. The source for such differences might correspond to higher order induction and dispersion terms which were excluded from the analytic formulation. Another source of error is the London approximation for the dispersion interaction.

The good agreement between both results confirms that the present PES has the proper physical behavior at the asymptotic limit. Therefore it is suitable for describing cold molecular collisions.

The asymptotic regions of the potential are mainly dominated by the electrostatic charge-quadrupole interaction ($\propto R^{-3}$), see Figure 6.3. However due to the anisotropic character of this interaction, the charge-induced dipole interaction ($\propto R^{-4}$) becomes the major contribution in the θ_1 angular range where $P_2^0(\cos \theta_1)$ is equal or close to zero.

6.4 Bound states

The rovibrational energy levels E_i have been obtained by solving variationally the space-fixed rigid rotor Schrödinger equation:

$$[\mathbf{H}(\mathbf{R}, \hat{\mathbf{r}}_1, \hat{\mathbf{r}}_2) - E_i] \Psi_i^{JM}(\mathbf{R}, \hat{\mathbf{r}}_1, \hat{\mathbf{r}}_2) = 0 \quad (6.5)$$

where the rovibrational wave functions Ψ_i^{JM} are expanded over a product of radial and symmetry-adapted angular functions.

$$\Psi_{j_1 j_2 j_{12} l}^{JM}(\mathbf{R}, \hat{\mathbf{r}}_1, \hat{\mathbf{r}}_2) = R^{-1} \sum_i^{i_{\max}} \sum_{j_1}^{j_{1\max}} \sum_{j_2}^{j_{2\max}} \sum_{j_{12}=|j_1-j_2|}^{j_1+j_2} \sum_{l=|J-j_{12}|}^{J+j_{12}} c_{j_1 j_2 j_{12} l}^{iJM} G_i(R) y_{j_1 j_2 j_{12} l}^{JM}(\hat{\mathbf{R}}, \hat{\mathbf{r}}_1, \hat{\mathbf{r}}_2) \quad (6.6)$$

where J and M are the quantum number of the total angular momentum and its projection onto the space-fixed z -axis, j_1 and j_2 are respectively the rotational angular momentum quantum number of H_2 and C_3N^- . The Sturmian functions $G_i(R)$ are used to obtain a discrete variable representation (DVR) of the radial part of these wave functions (see section 4.3) while the $y_{j_1 j_2 j_{12} l}^{JM}(\hat{\mathbf{R}}, \hat{\mathbf{r}}_1, \hat{\mathbf{r}}_2)$ are the coupled spherical harmonics defined by

$$y_{j_1 j_2 j_{12} l}^{JM}(\hat{\mathbf{R}}, \hat{\mathbf{r}}_1, \hat{\mathbf{r}}_2) = \sum_{\text{all } m} \langle j_1 m_1 j_2 m_2 | j_{12} m_{12} \rangle \langle j_{12} m_{12} l m_l | JM \rangle \times Y_{j_1 m_1}(\hat{\mathbf{r}}_1) Y_{j_2 m_2}(\hat{\mathbf{r}}_2) Y_{l m_l}(\hat{\mathbf{R}}) \quad (6.7)$$

The symmetry-adapted angular functions $y_{j_1 j_2 j_{12} l}^{JM}$ span the irreducible representations (see Table 6.4) of the group G_4 [139] which is the complete permutation inversion group that characterizes $\text{H}_2\text{--C}_3\text{N}^-$ system. As the $G_i(R)$ radial functions belong to the totally symmetric representation A_1 (i.e they remain unaltered under group's operations), the rovibrational wave function belongs to the same representation that the functions $y_{j_1 j_2 j_{12} l}^{JM}$ over which it is expanded.

The final energies are obtained by a sequential diagonalization-truncation procedure [140]. First, for each point of the radial DVR, the angular dependent part of the Hamiltonian is diagonalized in the angular basis defined by equation (6.7), and then truncated by retaining only the eigenfunctions whose eigenvalues are smaller than $E_{\text{cut}} = 2000 \text{ cm}^{-1}$. Secondly, the direct product of the truncated angular basis set by

Table 6.4: Classification of the symmetry-adapted angular basis set according to G_4 irreducible representations as a function of the parity, even (e) or odd (o), of j_1 and $j_2 + l$.

j_1	$j_2 + l$	Γ_i
e	e	A_1
e	o	A_2
o	e	B_1
o	o	B_2

the radial DVR is used to represent the full Hamiltonian which is then diagonalized.

Due to the variational nature of our approach, we have checked the convergence of the rovibrational energies with respect to the size of the basis set. Setting the convergence criterion at 0.001 cm^{-1} , we found that for each symmetry 30 and 4 rotational states of C_3N^- and H_2 , respectively, together with a 50 point radial DVR grid in the range $5\text{--}20 a_0$ are required to converge.

6.4.1 Vibrational levels and wave functions

The bound states energies for $J = 0$ are shown in Tables 6.5 and 6.6. The rovibrational ground state is largely above the SP1 saddle points and slightly lower than the SP2 saddle points by 7.7 cm^{-1} . All other bound states are above all the saddle points, therefore the rovibrational wave functions are expected to be delocalized over all minima.

Table 6.5: Lowest A_1 energy levels for $J = 0$, $l_v = 0$, and $v_3 = 0$, with their assigned vibrational quantum numbers v_1 and v_2 . The wave functions can be localized in MIN1 minima or in MIN2 minima or delocalized over all minima. Energy is given in cm^{-1} .

Level	MIN1		MIN2		Global		Energy
	v_1	v_2	v_1	v_2	v_1	v_2	
0	0	0			0	0	-257.22
1	2	0			2	0	-232.95
2	4	0			4	0	-216.34
3	6	0			6	0	-203.00
4	8	0			8	0	-189.93
5	10	0	0	0	10	0	-174.95
6	10	0	0	0	12	0	-174.76
7	12	0	2	0	14	0	-160.57
8	12	0	2	0	16	0	-157.08
9	0	1			0	1	-153.89

Continued on next page

Table 6.5 – *Continued from previous page*

Level	MIN1		MIN2		Global		Energy
	ν_1	ν_2	ν_1	ν_2	ν_1	ν_2	
10					18	0	-146.80
11					20	0	-137.43
12	2	1			2	1	-134.08
13					22	0	-125.76
14	4	1			4	1	-120.79
15					24	0	-113.17
16	6	1			6	1	-109.80
17	8	1			8	1	-99.17
18					26	0	-98.14
21	0	2			0	2	-83.73
22					28	0	-80.74

Table 6.6: Lowest B_2 energy levels for $J = 0$, $l_v = 0$, and $\nu_3 = 0$, with their assigned vibrational quantum numbers ν_1 and ν_2 . The wave functions can be localized in MIN1 minima or in MIN2 minima or delocalized over all minima. Energy is given in cm^{-1} .

Level	MIN1		MIN2		Global		Energy
	ν_1	ν_2	ν_1	ν_2	ν_1	ν_2	
0	0	0			0	0	-242.50
1	2	0			2	0	-214.84
2	4	0			4	0	-193.29
3	6	0			6	0	-174.67
4	8	0			8	0	-156.44
5			0	0	[10]	0	-141.71
6	10	0			[12]	0	-137.29
7	0	1			0	1	-125.74
8			2	0	[14]	0	-120.00
9	12	0			[16]	0	-116.38
10			4	0	[18]	0	-101.76
11	2	1			2	1	-101.45
12	14	0	6	0	20	0	-95.02
13	14	0	6	0	22	0	-84.47
14	4	1			4	1	-82.69

Continued on next page

Table 6.6 – Continued from previous page

Level	MIN1		MIN2		Global		Energy
	ν_1	ν_2	ν_1	ν_2	ν_1	ν_2	
15					24	0	-71.89
16	6	1			6	1	-66.53
17					26	0	-59.89
20	0	2			0	2	-39.41
22			0	1		1	-33.47

Some physical insight on the nature of the vibrational wave functions can be extracted from a normal mode analysis based on the Jacobi coordinates defined in Figure 6.1. The coordinate ϕ is however not defined for all the minima which have a linear geometry. Therefore the harmonics frequencies and normal modes of the minima have been obtained using the Wilson's FG method[141] restricted to the 3D space spanned by the coordinates R , θ_1 and θ_2 . The results are given in Table 6.7. Since the PES is highly anharmonic, the FG harmonic frequencies are significantly different from the accurate fundamental frequencies. However, it is still possible to establish a correspondence between both types of frequencies and therefore to associate the normal mode displacements to the fundamental frequencies, except for the ν_3 mode for which the harmonic frequency is larger than the dissociation energy. The high frequency of the ν_3 mode can be understood if we observe the Figure 6.2. Indeed, for $\theta_2 = 0^\circ$ or $\theta_2 = 180^\circ$, the motion along θ_1 is blocked by a large potential barrier. We furthermore note that the bending modes ν_1 and ν_3 are doubly degenerate as a result of the linear geometry of the equilibrium structures.

Table 6.7: Frequencies and normal modes coordinates for the global (MIN1) and secondary (MIN2) minima of $H_2-C_3N^-$.

Mode	Displacement	MIN1		MIN2	
		Harmonic	Fundamental	Harmonic	Fundamental
ν_1	$\Delta\theta_2$	49.9	14.4	44.8	8.8
ν_2	ΔR	196.8	103.3	201.5	–
ν_3	$\Delta\theta_1$	540.5	–	420.7	–

The molecular symmetry group[139] for linear molecules without a center of symmetry is called $C_{\infty v}(M)$ and is made of the two elements E and E^* . The harmonic vibrational wave functions, which are localized in a single potential well, can be classified according to the $C_{\infty v}(M)$ group irreducible representations as Σ^+ or Σ^- if they are symmetric or antisymmetric with respect to the inversion operation E^* .

The connection between the harmonic model and the full variational calculation can be deduced by invoking the permutation between the two identical H atoms. This operation transforms a minimum structure associated with $\theta_1 = 0^\circ$ into another equivalent one with $\theta_1 = 180^\circ$ or inversely. Therefore, the global wave functions can be expressed as linear combinations of two equivalent local wave functions:

$$\Psi_1 = \frac{1}{\sqrt{2}}(\varphi_{0^\circ} + \varphi_{180^\circ}) \quad (6.8)$$

$$\Psi_2 = \frac{1}{\sqrt{2}}(\varphi_{0^\circ} - \varphi_{180^\circ}) \quad (6.9)$$

These combinations lead to the following correspondence between the irreducible representations of the $C_{\infty v}(M)$ and G_4 groups:

$$\begin{aligned} 2\Sigma^+ &= A_1 \oplus B_2 \\ 2\Sigma^- &= A_2 \oplus B_1 \end{aligned} \quad (6.10)$$

In our case, the normal modes coordinates and the harmonic vibrational wave functions are invariant with respect to inversion. Thus they belong to the Σ^+ irreducible representation. Hence, for $J = 0$, we can obtain only global vibrational wave functions belonging to the A_1 and B_2 irreducible representations. In the harmonic approximation, vibrational energies level belonging to A_1 are degenerate with those of the B_2 . In the variational approach, which is based on a realistic PES, these levels are no longer degenerate since they are coupled by the PES. For instance, the energy splitting is about 15 cm^{-1} between the ground state of the symmetry A_1 (denoted by $A_{1,0}$) and the corresponding ground state of the symmetry B_2 (denoted by $B_{2,0}$). Hereinafter, the levels are denoted by the symbol of the irreducible representation followed by the number of the state in the series of states belonging to the same irreducible representation, ordered by increasing energy.

Contour plots of selected wave functions for $J = 0$ are shown in Figure 6.4. Let us remind that the two equivalent global minima MIN1 are located at $\theta_2 = 180^\circ$ while the two equivalent secondary minima MIN2 are at $\theta_2 = 0^\circ$. The panels (a) and (b) of Figure 6.4 show the ground state of each symmetry, A_1 and B_2 . Although their energies are above the saddle points, these wave functions are noticeably localized in the MIN1 region. In the panels (c) and (d) are shown the wave functions which can be described as the ground states of the secondary minima since they are the lowest levels clearly localized in the MIN2 region. These levels are labeled as $A_{1,5}$ and $B_{2,5}$. Again, although their energies are significantly above the MIN1 \leftrightarrow MIN2 interconversion barriers, these wave functions remain mostly localized in the MIN2 region. One can however observe in Figure 6.4 (c) a mixing with a ν_1 overtone localized in the global minimum MIN1. Such anharmonic resonances can be seen in many A_1 rovibrational levels, while in contrast they have a low occurrence for

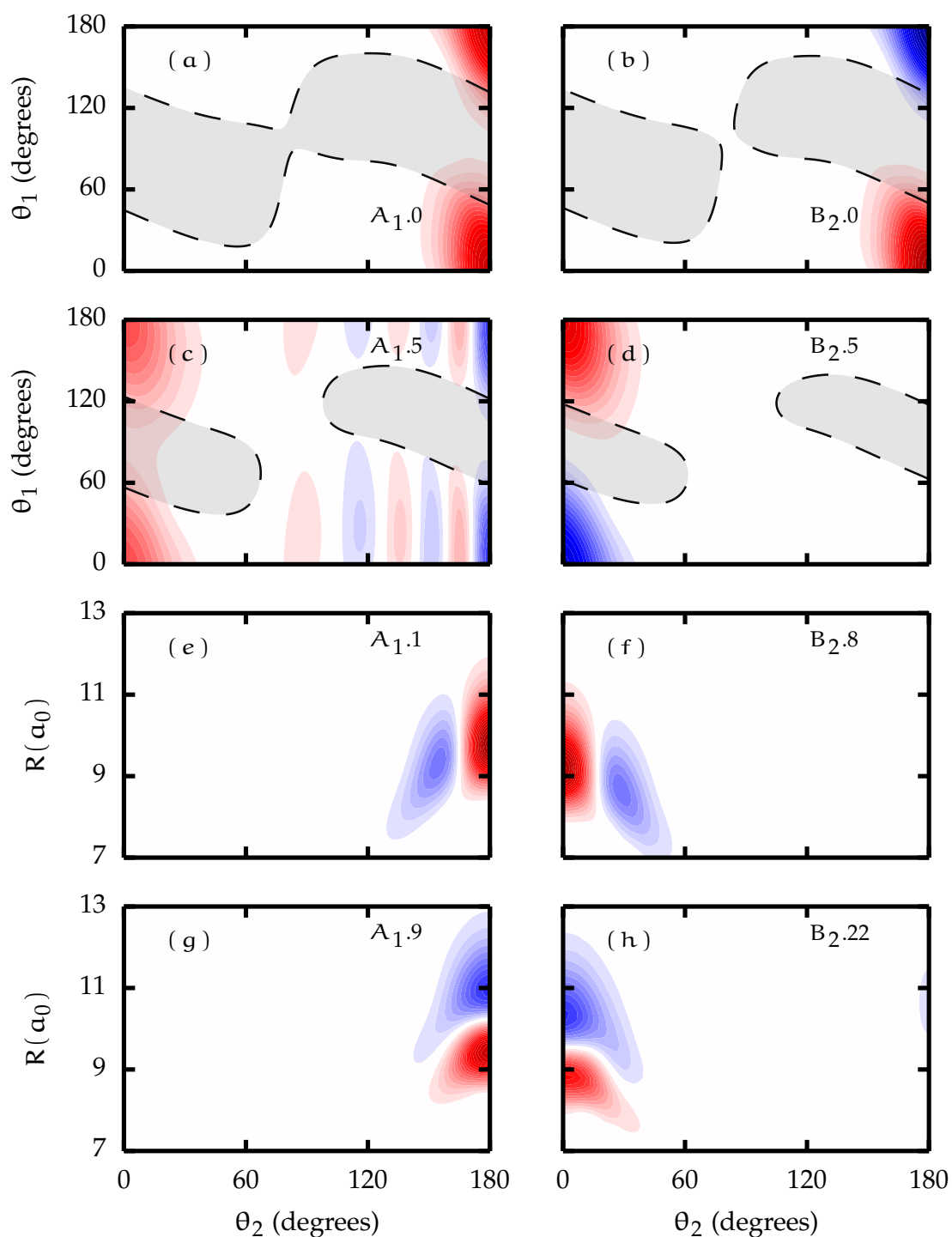


Figure 6.4: 2D contour plots for selected $J = 0$ rovibrational wave functions. Red contours correspond to positive amplitude and blue contours to negative amplitude. a–d) R is relaxed and $\phi = 0^\circ$; The shaded areas show the classically forbidden regions at the energy of the vibrational level. e–h) $\theta_1 = 0^\circ$, and $\phi = 0^\circ$.

the B_2 states. Figure 6.4 (c) shows also that the $A_{1.5}$ wave function span the whole range of variation of θ_1 , thus revealing a strong tunneling effect between the two equivalent MIN2 minima, even though the potential barrier is higher by about 125 cm^{-1} than the vibrational level $A_{1.5}$.

The first excited levels localized around the global minima MIN1, labeled by $A_{1.1}$ and $B_{2.1}$, correspond to a vibrational excitation in the mode ν_1 . The corresponding levels for the secondary minima MIN2 are $A_{1.7}$ and $B_{2.8}$. The levels $A_{1.1}$ and $B_{2.8}$ are shown in Figure 6.4 (e) and (f), respectively. Because of the small value of the ν_1 frequency for both MIN1 and MIN2 minima, many of the rovibrational levels are either pure or mixed ν_1 overtones.

The fundamental stretching mode is identified in levels $A_{1.9}$ and $B_{2.7}$ for the global minima MIN1, while for the secondary minima MIN2, it appears in levels $A_{1.20}$ and $B_{2.22}$. The levels $A_{1.9}$ and $B_{2.22}$ are shown in Figure 6.4 (g) and (h), respectively. Overtones and combination tones of the stretching mode ν_2 also occur although in a minor extent because of the high frequency of this mode.

The list of the lowest levels for which it is possible to assign vibrational quantum numbers is shown in Tables 6.5 and 6.6. Only levels with $J = 0$ are shown, and therefore the vibrational angular momentum l_ν associated to each doubly degenerate bending motion is also equal to zero. This imply an equal number of quanta in both states of each doubly degenerate bending motions. Only the ν_1 and ν_2 quantum numbers are reported in Tables 6.5 and 6.6 since no excited state was found for the ν_3 bending motion. As a matter of fact, this mode has a very large harmonic vibrational frequency, much larger than the dissociation energy.

Four cases appear when we examine the nodal pattern of the wave functions with respect to the rotation of C_3N^- , i.e. the coordinate θ_2 . In case 1 or 2, the wave function is localized in MIN1 or in MIN2 minima respectively, as shown in panels (a) and (d) of Figure 6.4. In case 3, the wave function is a combination of two local wave functions in MIN1 and MIN2 minima as for example shown in panel (c) of Figure 6.4. In case 4, the wave function is spanning the whole range of variation of θ_2 , as shown in Figure 6.5. In order to distinguish between these cases, three different lists of quantum numbers ν_1 and ν_2 are reported in Tables 6.5 and 6.6. When the vibrational wave function is clearly localized in the MIN1 minima, or in the MIN2 minima, or in both, then we assign quantum numbers to these local wave functions. The third list of quantum numbers is associated to the global wave function, which can be a wave function belonging to any of the four cases.

Table 6.5 shows that levels 0–4 are localized only in MIN1 while levels 5–8 are localized in MIN1 and MIN2 and are associated in symmetric or antisymmetric combinations, the antisymmetric combination adding one nodal plane in both degenerate states of the bending motion ν_1 . Some higher levels, such as levels 10, 11 and 13 for

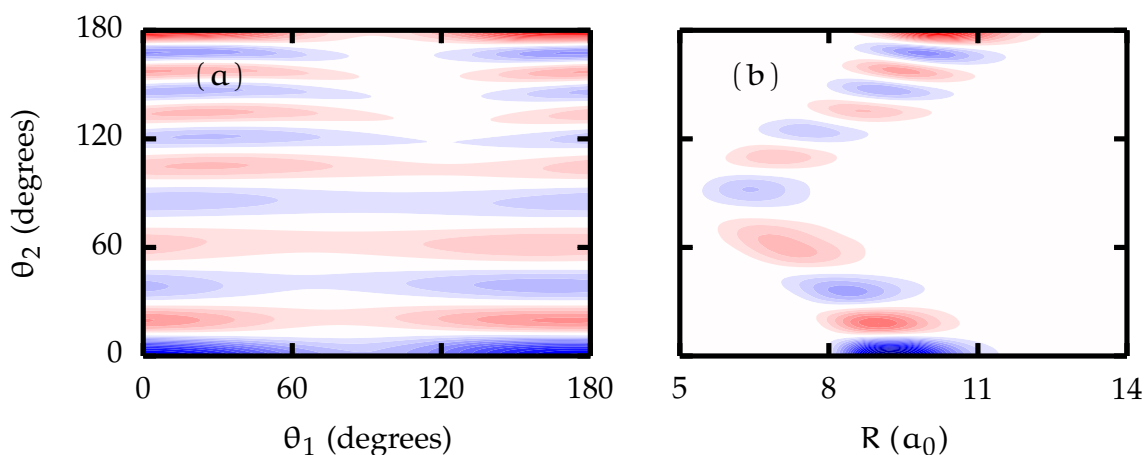


Figure 6.5: 2D contour plots of the $A_1.13$ rovibrational wave function for $J = 0$. Red contours correspond to positive amplitude and blue contours to negative amplitude.

example, are fully delocalized (see Figure 6.5) and therefore only global quantum numbers can be assigned to these levels. Whereas global quantum numbers can be assigned to all the A_1 levels listed in Table 6.5, such an assignment does not appear to be possible for all the B_2 levels listed in Table 6.6 as the wave functions of these levels which are localized in the MIN2 minima are not mixed with those localized in the MIN1 minima or vice versa. This is the case of the $B_2.5$, $B_2.6$, $B_2.8$, $B_2.9$, and $B_2.10$ levels. However, if we assume that the states are mixed, for example $B_2.5$ and $B_2.6$, then symmetric and antisymmetric combinations can be done and a hypothetical ν_1 global quantum number can be defined. In Table 6.6, the hypothetical quantum numbers are marked with square bracket.

Another important feature of this system is that a significant fraction of the vibrational wave functions are localized in small regions of the coordinate space although they could be delocalized over large regions since their energy is well above the interconversion barriers. This can be understood by analyzing the distribution of the vibrational energy among the mode of motions. The vibrational stretching motion frequency ν_2 is relatively large, around 103 cm^{-1} , while the frequency ν_3 which corresponds to the hindered rotation of H_2 , is even larger. Therefore, these two modes of motion withhold a large part of the vibrational energy, but they are not efficient for triggering the MIN1 \leftrightarrow MIN2 interconversion since this needs a rotation of C_3N^- . It is mainly the bending mode ν_1 which triggers the interconversion. Only the levels with enough energy in this last mode of motion are delocalized over both minima, MIN1 and MIN2, such as, for instance, the level $A_1.5$ shown in Figure 6.4 (c).

6.4.1.1 Vibrational frequencies

The ν_2 fundamental frequency associated with the MIN1 minima can be extracted from Table 6.5, but not the ν_1 fundamental frequency since the level $\nu_1 = 1$ is not allowed for $J = 0$. Indeed, $\nu_1 = 1$ implies $l_\nu = \pm 1$, which in turn implies $J \geq 1$. We have thus computed the $J = 1$ bound states and obtained the ν_1 fundamental frequency for both MIN1 and MIN2 minima. These results are shown in Table 6.7 along with the harmonic frequencies. The differences between both sets of data reveal the strong anharmonicities of the vibrational motions. A rough estimate of the ν_3 fundamental frequency can also be obtained from the equation $\nu_3 = \text{ZPE} - \nu_1 - \nu_2/2$. This gives a frequency value of 446 cm^{-1} , which is much larger than the dissociation energy, 257 cm^{-1} .

6.4.1.2 Rotational Constants

Since the MIN1 and MIN2 equilibrium structures of $\text{H}_2\text{-C}_3\text{N}^-$ are linear, there are only two equal rotational constants for each structure which can be calculated either by diagonalizing the inertia tensor or from the evaluation of the energy differences between the $J = 0$ and $J = 1$ ground levels. In the first case, we obtain 0.111 cm^{-1} and 0.115 cm^{-1} for the MIN1 and MIN2 equilibrium structures, respectively while in the second case, we obtain 0.165 cm^{-1} and 0.265 cm^{-1} . However for the MIN2 structure, the energy difference between the $J = 0$ and $J = 1$ levels involve mixed states, i.e. states which are not fully localized in the MIN2 potential wells, as shown in panel (c) of Figure 6.4.

6.4.2 Para and ortho states

Since the nuclear spin of hydrogen atom is $I_{\text{H}} = \frac{1}{2}$, the wave function of H_2 must be antisymmetric under the exchange of the two nuclei, as required by the Pauli's principle. Therefore, the total wave function of $\text{H}_2\text{-C}_3\text{N}^-$ which is given by the product $\Psi_{\text{elec}} \times \Psi_{\text{rovib}} \times \Psi_{\text{spin}}$ must belong to the irreducible representations B_1 or B_2 of the group G_4 . The electronic ground state wave function Ψ_{elec} belongs to the totally symmetric representation. The rovibrational wave functions Ψ_{rovib} can belong to any of the G_4 irreducible representations for $J \geq 1$ and only to A_1 and B_2 for $J = 0$.

We can obtain the symmetry representation of the spin wave functions Ψ_{spin} by considering the most abundant isotopes ^1H , ^{12}C , ^{14}N whose nuclear spin are $I_{\text{H}} = \frac{1}{2}$, $I_{\text{C}} = 0$, $I_{\text{N}} = 1$. Hence, the C_3N^- nuclear spin is $I = 1$ while the nuclear spin of H_2 can be $I = 0$ for (*para*- H_2) or $I = 1$ for (*ortho*- H_2). The coupling of the singlet spin state of H_2 , which is antisymmetric under the exchange of nucleus, with the triplet spin state of C_3N^- gives an antisymmetric triplet spin state for $\text{H}_2\text{-C}_3\text{N}^-$. On the other side, the coupling of the triplet spin state of H_2 , which is symmetric under the exchange of nucleus, with the triplet spin state of C_3N^- gives a singlet, a triplet,

and a quintet spin states for $H_2-C_3N^-$ which are all symmetric under H exchange. Using now the table of characters of the G_4 group and noting that all spin functions are symmetric under the inversion operator E^* , we see that the symmetric (under exchange) spin functions of $H_2-C_3N^-$ belong to the A_1 irreducible representation, while the antisymmetric spin functions belong to the B_2 irreducible representation.

Therefore, the spin states with symmetry A_1 ($I = 0, 1, 2$) are combined with the B_1 and B_2 rovibrational states to give the *ortho* states of $H_2-C_3N^-$ while the B_2 spin states ($I = 1$) are combined with the A_1 and A_2 rovibrational states to give the *para* states. The name *ortho(para)* is given to the states of the complex that asymptotically correlate with the dissociation limit *ortho*- H_2 (*para*- H_2) + C_3N^- . Since transitions between *ortho* and *para* states are forbidden one can consider them as two different species of the $H_2-C_3N^-$ complex. The rovibrational ground state of the *para* form is more stable than the *ortho* one by approximately 15 cm^{-1} .

6.5 Conclusion

A new 4D PES which accounts for the interaction between H_2 and the rigid C_3N^- has been presented. This PES has been designed for the study of collisional dynamics at low temperatures. We carefully checked the accuracy of the PES taking a peculiar care of the long-range interactions which accurately describe the asymptotic limit of dissociation. Two different linear equilibrium structures have been found, one with the C end of C_3N^- pointing towards H_2 which is the global minimum, and the other one with the N end of C_3N^- pointing towards H_2 which is the secondary minimum. Since the PES is symmetric under the exchange of the two H atoms, there is a total a four minima in the PES.

The rovibrational dynamics of the $H_2-C_3N^-$ van der Waals complex has been investigated, considering H_2 and C_3N^- as linear rigid rotors. The rovibrational wave functions have been developed over products of spaced-fixed coupled angular functions and radial functions obtained from a Sturmian DVR.

The examination of the rovibrational wave functions has revealed some quantum features such as unexpected wavefunction localization, tunneling effect and anharmonic resonances. The $H_2-C_3N^-$ system exhibits two doubly degenerate bending modes. One corresponds mainly to the hindered rotation of C_3N^- and the other mainly to the hindered rotation of H_2 . The vibrational dynamics of $H_2-C_3N^-$ is principally controlled by the considerable difference between the two bending frequencies. This difference results on one side from the large difference in mass between H_2 and C_3N^- and on the other side from the potential which is soft for the rotation of C_3N^- and stiff for the rotation of H_2 . The bending/rotation of C_3N^- , which triggers the interconversion $MIN1 \leftrightarrow MIN2$, is largely allowed since the saddle points energies are below those of almost all vibrational levels. But since much of the avail-

6.5. CONCLUSION

able vibrational energy is withheld by the bending/rotation motion of H_2 and also by the stretching motion, the wave functions remain localized in the MIN1 minima or in the MIN2 minima. In contrast, the bending/rotation of H_2 , which should allow transforming one MIN1 minimum into the other or one MIN2 minimum into the other, is blocked by a high potential barrier. But since H_2 is light, a significant tunneling effect is observed which causes a lifting of the degeneracy between symmetric and antisymmetric wave functions localized in equivalent potential wells by about 15 cm^{-1} .

Fundamental frequencies and rotational constants have been determined for both type of minima of the complex. We found that a full quantum treatment of the nuclei is required in order to obtain rotational constants and fundamental frequencies of such weakly bound van der Waals complexes with a good accuracy.

Chapter 7

Rotational relaxation of C_3N^- by collision with H_2

Contents

7.1	Introduction	94
7.2	Method	94
7.2.1	The two linear rigid rotors coupled equations	94
7.2.2	PES and the coupling matrix elements	96
7.2.3	Boundary conditions and cross sections	98
7.2.4	Parameters of the calculations	98
7.2.5	Computational methodology	99
7.3	Results	100
7.4	Conclusions	104

7.1 Introduction

The abundances of the molecules detected in the interstellar medium are extracted from the spectroscopic observations through radiative transfer calculations. This last step requires the detailed knowledge of the radiative and collisional rates. However rate coefficients for excitation and de-excitation induced by collision with H_2 , the most abundant interstellar molecule, are scarce especially for the recently detected anions. The only available data are limited to the collisions of H_2 with the CN^- [32] and C_6H^- [33] anions.

In chapter 5, we determined the rotational excitation and de-excitation rates of the C_3N^- anion in collisions with He. Such collisional rates are often used to estimate those for *para*- H_2 using a scaling law based on the ratio of the reduced masses. This approximation has however been widely criticized due to its lack of physical meaning and because it fails reproducing known collisional rates with *para*- H_2 for a few systems [117, 119].

In this chapter we focus on the calculation of the rotational relaxation rates of C_3N^- in collisions with both *ortho*- and *para*- H_2 for temperatures ranging from 10 to 300 K. While the CC method offers the highest level of accuracy for the calculation of the collisional rates its application to the $\text{H}_2 + \text{C}_3\text{N}^-$ collision is quite challenging because of the very small value of the rotational constant of C_3N^- , the large reduced mass of the system and the strong long-ranged anisotropic potential. Therefore, a few numerical and theoretical tricks are needed to make the calculations possible. The detail of these necessary adaptations of the CC method is provided in the following section while the results are discussed in section 7.3. The conclusions are eventually presented in section 7.4.

7.2 Method

In this section we give a brief account for the formalism of the quantum scattering theory of two colliding linear rigid rotors as described by Englot and Rabitz [142], Green [143].

7.2.1 The two linear rigid rotors coupled equations

The space-fixed axis and the Jacobi coordinates used to describe the interaction between H_2 and C_3N^- are shown in Figure 7.1. The Jacobi coordinates, namely the intermolecular vector \mathbf{R} and the angular coordinates of the molecular axis $\hat{\mathbf{r}}_2$ and $\hat{\mathbf{r}}_2$,

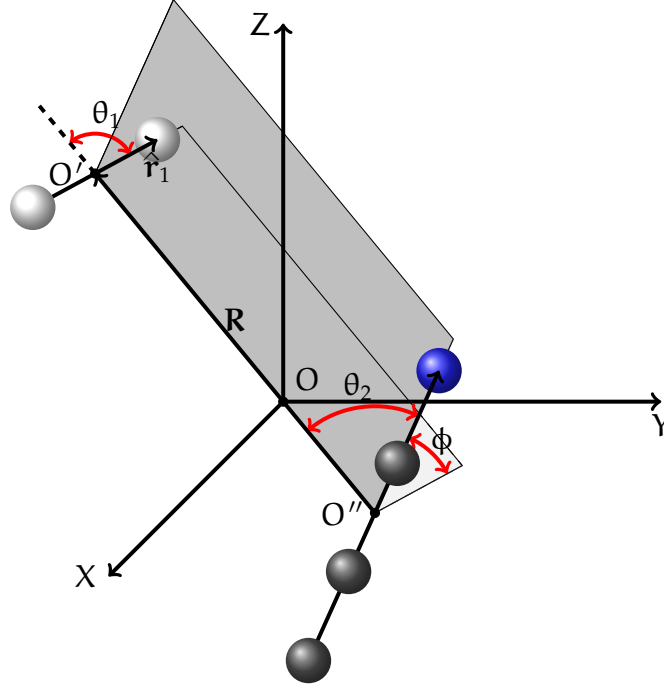


Figure 7.1: Space-fixed axes and Jacobi coordinates used to describe the interaction between H_2 and C_3N^- . O'' is the center of mass of C_3N^- , O' is the center of mass of H_2 and O is the center of mass of the whole system

are defined as follow:

$$\mathbf{R} = \mathbf{r}_{O'} - \mathbf{r}_{O''} \quad (7.1)$$

$$\hat{\mathbf{r}}_1 = \frac{\mathbf{r}_{H_a} - \mathbf{r}_{H_b}}{|\mathbf{r}_{H_a} - \mathbf{r}_{H_b}|} \quad (7.2)$$

$$\hat{\mathbf{r}}_2 = \frac{\mathbf{r}_N - \mathbf{r}_C}{|\mathbf{r}_N - \mathbf{r}_C|} \quad (7.3)$$

The orientation angle θ_1 , θ_2 , ϕ , are defined as

$$\cos \theta_1 = \hat{\mathbf{R}} \cdot \hat{\mathbf{r}}_1 \quad (7.4)$$

$$\cos \theta_2 = \hat{\mathbf{R}} \cdot \hat{\mathbf{r}}_2 \quad (7.5)$$

$$\cos \phi = \frac{(\mathbf{R} \times \hat{\mathbf{r}}_1) \cdot (\mathbf{R} \times \hat{\mathbf{r}}_2)}{|\mathbf{R} \times \hat{\mathbf{r}}_1| |\mathbf{R} \times \hat{\mathbf{r}}_2|} \quad (7.6)$$

whit $\hat{\mathbf{R}} = \mathbf{R}R^{-1}$ where R is the module of the vector \mathbf{R} .

The rigid rotor Hamiltonian in Jacobi coordinates takes the usual form

$$\mathbf{H}(\mathbf{R}, \hat{\mathbf{r}}_1, \hat{\mathbf{r}}_2) = -\frac{\hbar^2}{2\mu} \left[\frac{1}{R} \frac{\partial^2}{\partial R^2} R + \frac{\mathbf{l}^2}{R^2} \right] + \mathbf{H}_1(\hat{\mathbf{r}}_1) + \mathbf{H}_2(\hat{\mathbf{r}}_2) + \mathbf{V}(\mathbf{R}, \hat{\mathbf{r}}_1, \hat{\mathbf{r}}_2) \quad (7.7)$$

where μ is the reduced mass of the system, $\mathbf{V}(\mathbf{R}, \hat{\mathbf{r}}_1, \hat{\mathbf{r}}_2)$ is the interaction potential, \mathbf{l} is the relative angular momentum operator while \mathbf{H}_1 and \mathbf{H}_2 are respectively the space-fixed rigid-rotor Hamiltonian of H_2 and C_3N^- whose eigenfunctions satisfy:

$$\mathbf{H}_i(\hat{\mathbf{r}}_i) Y_{j_i m_i}(\hat{\mathbf{r}}_i) = B_i j_i(j_i + 1) Y_{j_i m_i}(\hat{\mathbf{r}}_i) \quad (7.8)$$

where B_i are the rotational constants.

It is convenient to work in the coupled representations thus combining the angular momentum of the two rigid rotors \mathbf{j}_1 , \mathbf{j}_2 and the orbital angular momentum \mathbf{l} to give the total angular \mathbf{J}

$$\begin{aligned}\mathbf{j}_1 + \mathbf{j}_2 &= \mathbf{j}_{12} \\ \mathbf{j}_{12} + \mathbf{l} &= \mathbf{J}\end{aligned}\quad (7.9)$$

In this representation, the angular functions are those defined in equation (6.7). The eigenfunctions of the total Hamiltonian (7.7) are then expanded in this basis set:

$$\Psi_{j_1 j_2 j_{12} l}^{JM}(\mathbf{R}, \hat{\mathbf{r}}_1, \hat{\mathbf{r}}_2) = R^{-1} \sum_{j_1}^{\infty} \sum_{j_2}^{\infty} \sum_{j_{12}=|j_1-j_2|}^{j_1+j_2} \sum_{l=|J-j_{12}|}^{J+j_{12}} G_{j_1 j_2 j_{12} l}^{J_1 J_2 J_3}(\mathbf{R}) y_{j_1 j_2 j_{12} l}^{JM}(\hat{\mathbf{R}}, \hat{\mathbf{r}}_1, \hat{\mathbf{r}}_2) \quad (7.10)$$

Substituting expansion (7.10) and (7.7), multiplying on the left by $y_{j_1 j_2 j_{12} l'}^{JM}{}^*$ and then integrating over all angular coordinates one obtains the following radial coupled equations

$$\left[\frac{d^2}{dR^2} - \frac{l'(l'+1)}{R^2} + k_{\gamma'}^2 \right] G_{\gamma'}^{J\gamma}(\mathbf{R}) = \frac{2\mu}{\hbar^2} \sum_{\gamma''} V_{\gamma'\gamma''}^J(\mathbf{R}) G_{\gamma''}^{J\gamma}(\mathbf{R}) \quad (7.11)$$

where $\gamma \equiv \{j_1, j_2, j_{12}, l\}$ and k_{γ} is the channel wave number defined as

$$k_{\gamma}^2 = \frac{2\mu}{\hbar} [E - B_1 j_1(j_1 + 1) - B_2 j_2(j_2 + 1)] \quad (7.12)$$

and $V_{\gamma'\gamma''}^J$ are the matrix elements of the potential in the coupled angular basis set:

$$V_{\gamma'\gamma''}^J(\mathbf{R}) = \iiint y_{\gamma'}^{JM}(\hat{\mathbf{R}}, \hat{\mathbf{r}}_1, \hat{\mathbf{r}}_2)^* \mathbf{V}(\mathbf{R}, \hat{\mathbf{r}}_1, \hat{\mathbf{r}}_2) y_{\gamma''}^{JM}(\hat{\mathbf{R}}, \hat{\mathbf{r}}_1, \hat{\mathbf{r}}_2) d\hat{\mathbf{R}} d\hat{\mathbf{r}}_1 d\hat{\mathbf{r}}_2 \quad (7.13)$$

This set of coupled equations can be cast in the form of equation (1.25)

$$\frac{d^2}{dR^2} G_{\gamma'}^{J\gamma}(\mathbf{R}) = \sum_{\gamma''} W_{\gamma'\gamma''}^J(\mathbf{R}) G_{\gamma''}^{J\gamma}(\mathbf{R}) \quad (7.14)$$

by defining

$$W_{\gamma'\gamma''}^J(\mathbf{R}) = \frac{2\mu}{\hbar^2} V_{\gamma'\gamma''}^J(\mathbf{R}) + \frac{l'(l'+1)}{R^2} \delta_{l'l''} - k_{\gamma'}^2 \delta_{\gamma'\gamma''} \quad (7.15)$$

7.2.2 PES and the coupling matrix elements

The potential energy surface used in this work was developed in the previous chapter. The 4D PES was expressed in body-fixed Jacobi coordinates, namely R the intermolecular distance, θ_1 and θ_2 the rotation angle of H_2 and C_3N^- , respectively, and ϕ the torsion angle between the two molecules, see Figure 7.1. The functional form of the PES is defined as the product of a radial and an angular part, the latter being a product of associated normalized Legendre polynomials $P_l^m(x)$ and cosine functions:

$$V(\mathbf{R}, \theta_1, \theta_2, \phi) = \sum_{\lambda_1 \lambda_2 \mu} v_{\lambda_1 \lambda_2}^{\mu}(\mathbf{R}) P_{\lambda_1}^{\mu}(\cos \theta_1) P_{\lambda_2}^{\mu}(\cos \theta_2) \cos \mu \phi \quad (7.16)$$

The radial part is defined as the summation of two terms associated with the short-range and long-range contributions.

$$v_{\lambda_1\lambda_2}^\mu(\mathbf{R}) = S(\mathbf{R})f_{SR}(\mathbf{R}) + [1 - S(\mathbf{R})]f_{LR}(\mathbf{R}) \quad (7.17)$$

while the switching function $S(\mathbf{R})$ is an hyperbolic tangent. The short-range contribution $f_{SR}(\mathbf{R})$ was interpolated using a cubic spline method, whereas the long-range part $f_{LR}(\mathbf{R})$ was fitted to reciprocal power functions. In order to calculate the matrix elements (7.13) it is however easier to expand the interaction potential as a function of the space-fixed Jacobi coordinates \mathbf{R} , $\hat{\mathbf{r}}_1$, $\hat{\mathbf{r}}_2$. To this end, one uses the following space-fixed expansion of the interaction potential:

$$\mathbf{V}(\mathbf{R}, \hat{\mathbf{r}}_1, \hat{\mathbf{r}}_2) = \sum_{\lambda_1\lambda_2\lambda} A_{\lambda_1\lambda_2}^\lambda(\mathbf{R}) \mathcal{J}_{\lambda_1\lambda_2\lambda}(\hat{\mathbf{R}}, \hat{\mathbf{r}}_1, \hat{\mathbf{r}}_2) \quad (7.18)$$

where $\mathcal{J}_{\lambda_1\lambda_2\lambda}$ are linear combinations of product of spherical harmonics

$$\mathcal{J}_{\lambda_1\lambda_2\lambda}(\hat{\mathbf{R}}, \hat{\mathbf{r}}_1, \hat{\mathbf{r}}_2) = \sum_{\mu_1\mu_2\mu} \langle \lambda_1\mu_1\lambda_2\mu_2 | \lambda\mu \rangle Y_{\lambda_1\mu_1}(\hat{\mathbf{r}}_1) Y_{\lambda_2\mu_2}(\hat{\mathbf{r}}_2) Y_{\lambda\mu}^*(\hat{\mathbf{R}}) \quad (7.19)$$

Green [143] showed that the relation between the representations (7.16) and (7.19) is simply given by:

$$\begin{aligned} \mathcal{J}_{\lambda_1\lambda_2\lambda}(\hat{\mathbf{R}}, \hat{\mathbf{r}}_1, \hat{\mathbf{r}}_2) &= \left(\frac{2\lambda + 1}{4\pi} \right)^{\frac{1}{2}} \sum_{\mu=0}^{\lambda_{\min}} (-1)^\mu (2 - \delta_{\mu 0}) \langle \lambda_1\mu\lambda_2 - \mu | \lambda 0 \rangle \\ &\quad \times P_{\lambda_1}^\mu(\cos \theta_1) P_{\lambda_2}^\mu(\cos \theta_2) \cos \mu\phi \end{aligned} \quad (7.20)$$

from which one can obtain the following relationships between the space-fixed and body-fixed radial coefficients:

$$v_{\lambda_1\lambda_2}^\mu(\mathbf{R}) = (-1)^\mu (2 - \delta_{\mu 0}) \sum_{\lambda=|\lambda_1-\lambda_2|}^{\lambda_1+\lambda_2} \left(\frac{2\lambda + 1}{16\pi^3} \right)^{\frac{1}{2}} \langle \lambda_1\mu\lambda_2 - \mu | \lambda 0 \rangle A_{\lambda_1\lambda_2}^\lambda(\mathbf{R}) \quad (7.21)$$

and

$$A_{\lambda_1\lambda_2}^\lambda(\mathbf{R}) = \left(\frac{2\lambda + 1}{16\pi^3} \right)^{-\frac{1}{2}} \sum_{\mu=0}^{\lambda_{\min}} (-1)^\mu \langle \lambda_1\mu\lambda_2 - \mu | \lambda 0 \rangle v_{\lambda_1\lambda_2}^\mu \quad (7.22)$$

with the restriction that $\lambda + \lambda_1 + \lambda_2$ must be even. λ_{\min} is the minimum value between λ_1 and λ_2 .

Using expansion (7.18), one can readily obtain the coupling matrix elements:

$$\begin{aligned} V_{\gamma\gamma'}^J &= (4\pi)^{-3/2} \sum_{\lambda_1\lambda_2\lambda} (-1)^{J+j_1+j_2+j'_2} A_{\lambda_1\lambda_2}^\lambda(\mathbf{R}) ([\lambda^2][\lambda_1][\lambda_2][j_1][j_2][j_{12}][l])^{1/2} \\ &\quad \times ([j'_1][j'_2][j'_{12}][l'])^{1/2} \begin{pmatrix} \lambda & l' & l \\ 0 & 0 & 0 \end{pmatrix} \begin{pmatrix} \lambda_1 & j'_1 & j_1 \\ 0 & 0 & 0 \end{pmatrix} \\ &\quad \times \begin{pmatrix} \lambda_2 & j'_2 & j_2 \\ 0 & 0 & 0 \end{pmatrix} \left\{ \begin{matrix} l & l' & \lambda \\ j_{12} & j'_{12} & J \end{matrix} \right\} \left\{ \begin{matrix} j'_{12} & j'_2 & j'_1 \\ j_{12} & j_2 & j_1 \\ \lambda & \lambda_2 & \lambda_1 \end{matrix} \right\} \end{aligned} \quad (7.23)$$

where $[j] \equiv 2j + 1$

7.2.3 Boundary conditions and cross sections

The coupled radial equations for the collision of C_3N^- and H_2 are solved using an improved version of the code DIDIMAT [115] which uses the log-derivative propagator developed by Manolopoulos [43]. By choosing the following boundary conditions for the radial part of the scattering wave function:

$$\mathbb{G}^J(0) = 0$$

and

$$\mathbb{G}^J(R) \xrightarrow{R \rightarrow \infty} \mathbb{J}^J(R)\mathbb{A}^J - \mathbb{N}^J(R)\mathbb{B}^J \quad (7.24)$$

and defining the \mathbb{K}^J and \mathbb{T}^J matrices

$$\begin{aligned} \mathbb{K}^J &= \mathbb{B}^J (\mathbb{A}^J)^{-1} \\ \mathbb{T}^J &= -2i\mathbb{K}^J (\mathbb{I} - i\mathbb{K}^J)^{-1} \end{aligned} \quad (7.25)$$

where $\mathbb{N}^J(R)$ and $\mathbb{J}^J(R)$ are diagonal matrices of spherical Ricatti-Bessel functions of the first \tilde{j}_l and second \tilde{n}_l kinds. We can calculate the averaged transition probabilities as a function of the matrix elements of the \mathbb{T}^J matrix,

$$\begin{aligned} P_{j_1 j_2 \rightarrow j_1' j_2'}^J &= \frac{1}{(2j_1 + 1)(2j_2 + 1)} \sum_{j_{12}=|j_1-j_2|}^{j_1+j_2} \sum_{j_{12}'=|j_1'-j_2'|}^{j_1'+j_2'} \\ &\times \sum_{l=|J-j_{12}|}^{J+j_{12}} \sum_{l'=|J-j_{12}'|}^{J+j_{12}'} T_{j_1, j_2, j_{12}, l, j_1', j_2', j_{12}', l'}^J \end{aligned} \quad (7.26)$$

and consequently the inelastic cross sections:

$$\sigma_{j_1 j_2 \rightarrow j_1' j_2'} = \frac{\pi}{k_\gamma^2} \sum_{J=0}^{\infty} (2J+1) P_{j_1 j_2 \rightarrow j_1' j_2'}^J \quad (7.27)$$

Finally, the rotational relaxation rates of C_3N^- in collisions with H_2 can be obtained by thermally averaging the inelastic cross sections $\sigma_{j_1 j_2 \rightarrow j_1' j_2'}$ over a Boltzmann distribution of the collision energy E_c , equation 5.24. The rate coefficient for the reverse process $k_{j_1' j_2' \rightarrow j_1 j_2}$ is obtained from detailed balance:

$$\frac{k_{j_1' j_2' \rightarrow j_1 j_2}}{k_{j_1 j_2 \rightarrow j_1' j_2'}} = \frac{(2j_1 + 1)(2j_2 + 1)}{(2j_1' + 1)(2j_2' + 1)} \exp\left(-\frac{\epsilon_{j_2} - \epsilon_{j_2'} + \epsilon_{j_1} - \epsilon_{j_1'}}{k_B T}\right) \quad (7.28)$$

where ϵ_j are the rigid rotor energies of the two linear molecules

7.2.4 Parameters of the calculations

In the present calculation we neglect the vibration of both H_2 and C_3N^- , thus considering both molecules as rigid rotors whose rotational constant are set to their experimental values $B_1 = 60.853 \text{ cm}^{-1}$ [144] and $B_2 = 0.1618 \text{ cm}^{-1}$ [100]. The small value of the rotational constant in the case of C_3N^- requires using a large number of rotational levels to build the rotational basis set for the dynamics. The highest rotational level of C_3N^- used in any calculation was $j_2 = 30$ while for H_2 it was $j_1 = 2$

for *para*- H_2 and $j_1 = 3$ for *ortho*- H_2 .

The calculations are performed for a grid of collision energies E_c ranging from 0.1 to 2000 cm^{-1} . For each collision energy, we checked the convergence of the total quenching cross section as a function of the total angular momentum quantum number J and the maximum distance in the propagation of the radial wave function. A large reduced mass implies that many values of the total angular momentum quantum number J are needed to obtain converged cross sections. Up to 157 values of J were required for the highest energies. Because of the long-range potential strength, the propagation of the radial wave functions needed to be carried out up to a maximum value of 200 a_0 .

7.2.5 Computational methodology

The aforementioned requirements make the CC calculation prohibitively expensive even at very low collision energy. Hence, we developed a MPI version of the DIDIMAT code using an asynchronous task parallelization scheme. The MPI code distributes N tasks over M processor where each task corresponds to a propagation of the wave function for a given collision energy and a given value of J .

We also used the UJS method developed by Zhang and Zhang [122] in order to reduce the CPU time while keeping a good accuracy of the state-to-state rate coefficients. As a matter of fact, we showed in our study dedicated to the rotational excitation of C_3N^- in collisions with He (chapter 5) that this method offers a very good level of accuracy when compared with exact calculations. The strategy of this method is to compute the transition probabilities for selected values of J and then implicitly interpolate the missing probabilities in such a way that they reproduce as accurately as possible the rate coefficient at a given temperature. In the present case we computed the transition probabilities for the following values of $J \in \{0, 5, 10, 15, 20, 25, 30, 40, 60, 80\}$ using CC calculations. We then interpolate or extrapolate the missing contributions and sum them from $J = 0$ up to 200, see appendix B. In order to check the accuracy of the method we also performed exact CC calculations for the collisions involving *para*- H_2 and compared our results with those obtained using the UJS procedure as represented in Figure 7.2.

As can be seen on this figure the agreement between the two kinds of calculation is remarkably good especially for the higher temperatures. While the mean relative error is smaller than 3% for the whole temperature range, the largest relative error, $\sim 10\%$, is reached at low temperature [10 – 50] K. In this range of low temperatures the magnitude of the rate coefficients are anyway very small and the origin of the error is essentially numerical.

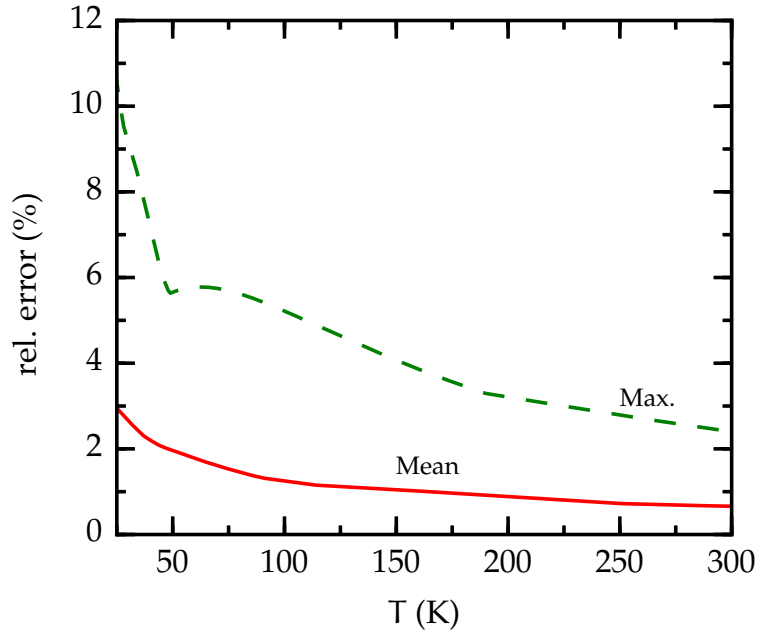


Figure 7.2: Error on the calculation of *para*-H₂ rate coefficients by using the UJS procedure as a function of temperature.

7.3 Results

Selected state-to-state rate coefficients for rotational excitation and de-excitation of C₃N⁻ by collisions with *ortho* and *para*-H₂ are shown in Table 7.1 and Figure 7.3.

Table 7.1: State to state rate coefficients $k_{j_1, j_2 \rightarrow j_1', j_2'}$ (cm³molecule⁻¹s⁻¹) for the rotational excitation of C₃N⁻ in collision with *para*($j_1 = 0$) and *ortho*($j_1 = 1$) H₂ for various temperature values. Powers of 10 are denoted in parenthesis.

j_1	j_2	j_1'	j_2'	T = 10 K	T = 100 K	T = 300 K
0	0	0	1	2.16(-10)	3.95(-10)	4.73(-10)
1	0	1	1	4.28(-10)	3.99(-10)	4.69(-10)
0	0	0	2	2.94(-10)	3.65(-10)	4.85(-10)
1	0	1	2	2.70(-10)	3.68(-10)	5.41(-10)
0	0	0	3	1.92(-10)	2.97(-10)	3.62(-10)
1	0	1	3	2.22(-10)	2.64(-10)	3.35(-10)
0	0	0	4	1.15(-10)	1.84(-10)	2.24(-10)
1	0	1	4	1.46(-10)	2.00(-10)	2.38(-10)
0	5	0	6	2.09(-10)	3.51(-10)	4.20(-10)
1	5	1	6	2.83(-10)	3.32(-10)	3.94(-10)
0	5	0	7	1.33(-10)	2.46(-10)	3.30(-10)
1	5	1	7	1.46(-10)	2.74(-10)	3.57(-10)

Continued on next page

Table 7.1 – Continued from previous page

j_1	j_2	j_1'	j_2'	$T = 10$ K	$T = 100$ K	$T = 300$ K
0	5	0	8	7.06(-11)	1.97(-10)	2.43(-10)
1	5	1	8	8.13(-11)	1.73(-10)	2.15(-10)
0	5	0	9	3.36(-11)	1.27(-10)	1.73(-10)
1	5	1	9	4.46(-11)	1.49(-10)	1.73(-10)
0	10	0	11	1.69(-10)	3.27(-10)	3.89(-10)
1	10	1	11	1.80(-10)	2.96(-10)	3.65(-10)
0	10	0	12	8.30(-11)	2.07(-10)	2.93(-10)
1	10	1	12	8.78(-11)	2.35(-10)	3.21(-10)
0	10	0	13	3.43(-11)	1.70(-10)	2.11(-10)
1	10	1	13	3.41(-11)	1.45(-10)	1.88(-10)
0	10	0	14	1.17(-11)	9.98(-11)	1.43(-10)
1	10	1	14	1.49(-11)	1.15(-10)	1.43(-10)

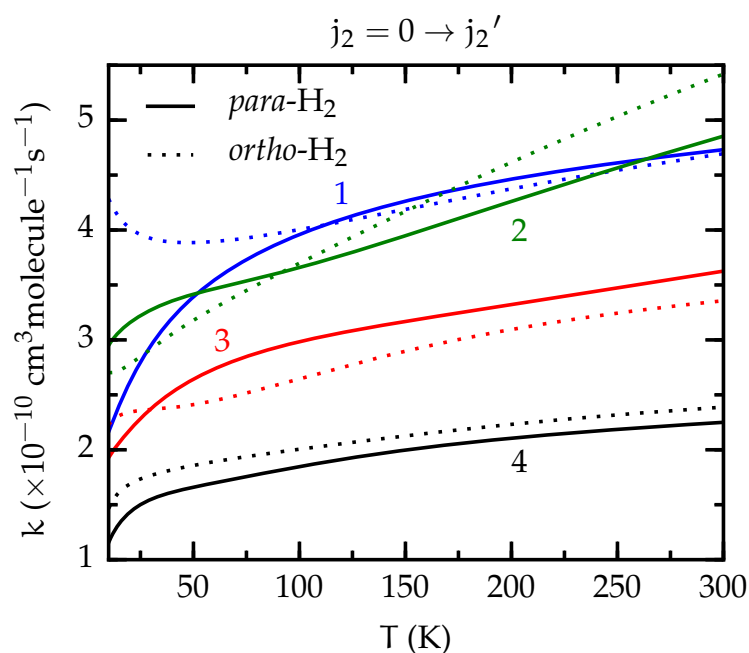


Figure 7.3: Rotational excitation rate coefficients of C_3N^- in collision with *ortho*- (dotted lines) and *para*- H_2 (full lines). The curves are labeled by the final state of the transition $j_2 \rightarrow j_2'$

As can be seen in this figure, the rate coefficients increase slowly as a function of temperature while they monotonously decrease when the transferred angular momentum Δj_2 of C_3N^- increases. Another important result for this system lies in the close resemblance between *ortho*- and *para*- H_2 rates, especially at higher temperatures.

Similarities between *ortho* and *para* rates have also been observed for the collision of H_2 with other anions such as CN^- (Kłos and Lique 2011) and C_6H^- (Walker et al. 2017). These authors suggested that the observed likeness could arise from the strength of the charge-quadrupole or charge-induced dipole long-range potentials. This explanation however does not seem to hold as the highest level of similarity is observed at higher temperature for which only the short range potential is important. Furthermore, the same similarities have been also found for the collisions of H_2 with HC_3N [129]. Therefore the resemblance between *ortho* and *para* rates seems to be rather a consequence of the angular anisotropy and of the strength of the short-range interaction.

In order to find out a possible origin of the resemblance between *ortho* and *para* results we need to analyze the matrix elements of the potential which are directly related to the space-fixed expansion coefficients $A_{\lambda_1\lambda_2}^\lambda(R)$ depicted in Figure 7.4. For collisions involving *para*- H_2 ($j_1 = 0$), the coupling matrix elements, (7.23), are non zero only if $\lambda_1 = 0$ while for those of *ortho*- H_2 ($j_1 = 1$) both $\lambda_1 = 0$ and 2 are possible.

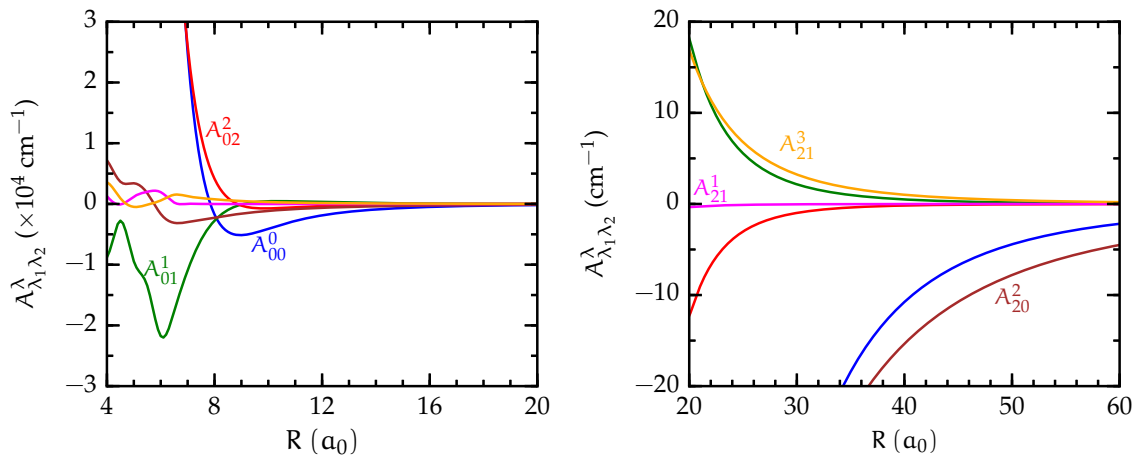


Figure 7.4: First six expansion coefficients $A_{\lambda_1\lambda_2}^\lambda$ as a function of the intermolecular distance. The curves are labeled by their corresponding indexes.

Figure 7.4 shows that the interaction at short-range distances is dominated by the attractive $\lambda_1 = 0$ term which gives non zero contributions for collisions involving both *ortho*- and *para*- H_2 . Conversely, the strongest contribution to the long-range part of the potential is associated with the charge-quadrupole A_{20}^2 term which gives non zero potential matrix elements only for the *ortho* states of H_2 . This is indeed what can be seen in Figure 7.3 where the difference between *para* and *ortho* rates are seen to be larger at low temperatures, while decreasing at higher temperature. Calculations for the higher rotational states of *ortho*- H_2 ($j_1 = 3, 4 \dots$) and *para*- H_2 ($j_1 = 2, 4 \dots$) are however needed to check if these similarities can be extended to these higher rotational states.

Because the rotational relaxation rates of the three anions (CN^- , C_3N^- and C_6H^-)

show the same likeness between *ortho* and *para* rates, it may be tempting to test if any simple rule could allow deducing C_3N^- rates from those of C_6H^- and CN^- . In Figure 7.5 we show the rate coefficient at 100 K for the de-excitation transition of C_3N^- ($j_2 = 10$) through collision with H_2 , along with the corresponding rates for CN^- and C_6H^- .

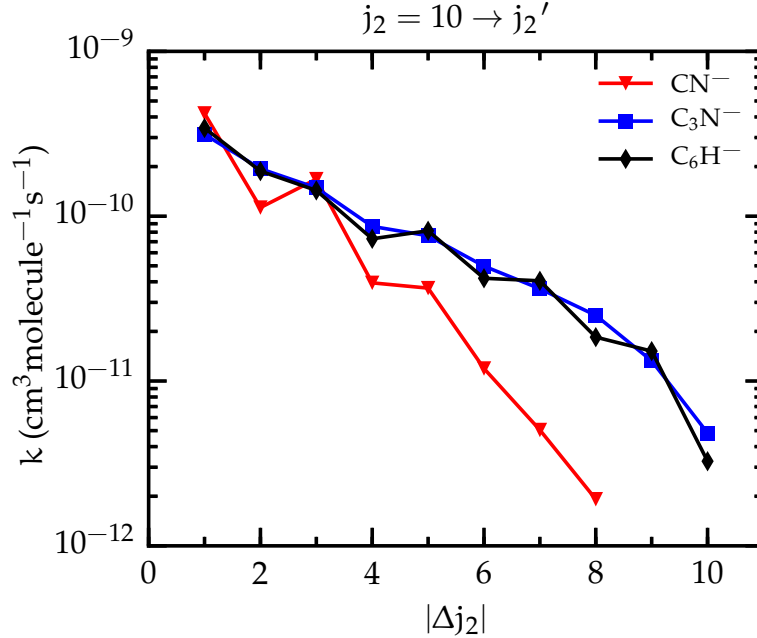


Figure 7.5: De-excitation rate coefficients of CN^- , C_3N^- , C_6H^- by collision with *para*- H_2 at 100 K as a function of the magnitude of the transferred angular momentum $|\Delta j_2|$.

As can be seen the agreement between the CN^- and C_3N^- rates is relatively good only for transitions with small $|\Delta j_2|$ while for larger values of $|\Delta j_2|$ CN^- rates are smaller than the C_3N^- ones. We think that these differences come from the size difference of the CN^- and C_3N^- molecules. The bigger the molecule the more repulsive the short-range potential will be thus enhancing transition with large transferred angular momentum $|\Delta j_2|$. The results for C_6H^- , are seen to be in remarkably good agreement with those for C_3N^- for all the transitions. We then suggest that similar effect to those found for C_3N^- and C_6H^- could also be seen for larger chains of their respective families $C_{2n+1}N^-$ and $C_{2n}H^-$ for which rotational relaxation rates could be estimated from the former ones.

A common stereotype in collisional rates calculations of *para*- H_2 ($j_1 = 0$) with any molecule is to approximate them using those for collision with He via the following scaling law

$$r = \frac{k_{0,j \rightarrow 0,j'}(H_2)}{k_{j \rightarrow j'}(He)} = \sqrt{\frac{\mu_{He-X}}{\mu_{H_2-X}}} \approx \sqrt{2} \quad (7.29)$$

where μ are the corresponding reduced masses. In order to test the validity of this

approximation in the case of C_3N^- we computed the ratio between our previously obtained rates for the collisions with He and those we calculated for *para*- H_2 . We found that this ratio can reach values as large as 6 at low temperature while it is in average equal to $r \approx 3$. Even this averaged value is already more than the double of the scaling value (7.29), thus leading to relatively large average error ($< 50\%$) for the scaled *para*- H_2 rate coefficients. In addition, the use of the scaled He rates would introduce a spurious propensity rule $\Delta j_2 = 2$ which is not obtained when performing exact calculations.

In order to try to better understand the origin of this scaling law failure, we averaged the $H_2-C_3N^-$ PES over the ($j_1 = 0$) rotational state of *para*- H_2 and compared it with the He- C_3N^- potential in Figure 7.6.

We see at first that the long-range potential is stronger in the case of *para*- H_2 . This is mainly due to the large difference between the isotropic polarizabilities¹, of He ($\alpha(\text{He}) = 1.38 a_0^3$) and H_2 ($\alpha(H_2) = 5.4 a_0^3$) as the charge induced dipole $-\frac{\alpha}{R^4}$ is the leading contribution to both interaction potentials at large distance. As a result, the long range interaction of C_3N^- with H_2 is almost five times bigger than its He counterpart. This may explain the quite large ratio of 6 found at low collision energy. A second important feature of the comparison between the two systems can be seen when comparing the two potential wells which are both found to be associated with a distorted T-shape geometry while the *para*- H_2-C_3N well is slightly deeper than the He- C_3N^- by a few cm^{-1} . If we now compare the symmetry of the two PES with respect to the inversion of the C_3N molecule, we found that both PES are far from being symmetric with respect to the inversion of C_3N^- while the interaction with He is clearly more symmetrical than the one with H_2 . This last point may explain the differences observed in the propensity rules.

7.4 Conclusions

State-to-state rotational excitation and de-excitation rates of C_3N^- in collisions with *ortho*- and *para*- H_2 in the temperature interval [10, 300] K were obtained by combining CC calculations and the UJS procedure. The strongly repulsive nature of the $H_2-C_3N^-$ interaction at short range leads to close similarities between *ortho* and *para* rates and enhances transitions associated with large transferred angular momentum.

We found that the application of the scaling law to the He- C_3N^- rates would lead to relatively large errors ($< 50\%$) on the estimation of *para*- H_2 rates. We also evaluate the possibility of using the available rates for CN^- and C_6N^- to obtain those of C_3N^- . We find that using the CN^- rates gives relatively good results but only for transitions associated with small $|\Delta j_2|$. On the other side, a remarkably good

¹Calculated using finite field method at CCSD(T)/aug-cc-pVQZ level

7.4. CONCLUSIONS

agreement is found between the C_3N^- and C_6H^- rates. We also find that the relative error related to the UJS method is always less than 10% demonstrating once again that the UJS procedure is a very good approximation which reduces computational cost without losing much accuracy.

Chapter 8

Quantum tunneling in weakly bound complexes: the case of the CO₂-N₂ dimer

Contents

8.1	Introduction	108
8.2	Variational bound states calculations	109
8.2.1	The CO ₂ -N ₂ PES	109
8.2.2	Symmetry of the CO ₂ -N ₂ vibrational wave functions	111
8.3	Vibrational normal modes – asymmetric top model	111
8.3.1	Symmetry considerations	113
8.4	Rovibrational bound states	115
8.5	Rovibrational spectrum	122
8.5.1	Dipole moment operator and selection rules	123
8.5.2	Nuclear spin wave function and spin statistic	123
8.5.3	Comparison with experiments	124
8.6	Conclusion	125

Published

M. Lara-Moreno, T. Stoecklin, P. Halvick, and M. Hochlaf. Quantum tunneling dynamical behaviour on weakly bound complexes: the case of a CO₂-N₂ dimer. *Phys. Chem. Chem. Phys.*, doi:10.1039/C8CP04465A, 2018

8.1 Introduction

Weakly bonded molecular clusters formed by abundant molecular species (e.g., H_2 , CO , N_2 , O_2 , CO_2) can be produced in laboratories. The $\text{CO}_2\text{-N}_2$ complex is formed through favorable interactions between CO_2 and N_2 , which are important constituents of the Earth atmosphere. Upon complexation, the infrared inactive vibrational modes of CO_2 and N_2 become slightly allowed and therefore may participate in the energy redistribution and transfer in the atmosphere (e.g., greenhouse effect). This occurs after elastic and inelastic collisions, where rotational and/or vibrational and/or electronic (de-) excitation processes may take place. In addition, trapping of the complex in the potential wells should lead to unexpected quantum effects which influence the outcomes of these collisions. $\text{CO}_2\text{-N}_2$ complex can be studied in extraordinary detail by high-resolution spectroscopic techniques in the frequency or time domains.

To the date, several experimental works have treated the rotational and rovibrational spectroscopy of the $\text{CO}_2\text{-N}_2$ cluster [146–149]. The ground state of the complex has been characterized using infrared and Fourier transform microwave (FTMW) spectroscopies. Accurate structural and spectroscopic data for the ground state of the complex and its isotopologues are available in the spectral region around the ν_3 band of the isolated CO_2 . These studies proposed a distorted T-shape structure, hereafter referred as the R_0 structure, with $\text{O}=\text{C}=\text{O}$ as the cross of the T and the $\text{N}\equiv\text{N}$ axis pointing toward the carbon atom. The N_2 and CO_2 monomers internuclear axis deviates by some degrees ($5^\circ\text{--}20^\circ$) from those of a pure C_{2v} molecule. In contrast, theoretical investigations [147, 150–153] at several levels of theory showed that the equilibrium structure of the most stable form, hereafter referred as R_e , is of C_{2v} symmetry. In 2015, Nasri et al. [153] proposed that the deviation between R_0 and R_e structures may be due to the complex dynamics of the weakly bound complex.

In this chapter, we use a variational approach that fully accounts for all angular momenta coupling. Our treatment provides the energy levels and their 4D rovibrational wave functions for the most abundant isotopologue $^{12}\text{C}^{16}\text{O}_2\text{-}^{14}\text{N}_2$. We analyzed both the pattern of the rovibrational levels and the corresponding wave functions. A further complication comes from the permutation of identical nuclei which is solved here by finding the correspondence between the C_{2v} point group (which characterizes the $\text{CO}_2\text{-N}_2$ complex at equilibrium geometry) and the G_8 permutation group. This study shows that the analysis of these wave functions allows full understanding of the complex dynamics of this dimer.

8.2 Variational bound states calculations

The calculations were performed in the space-fixed coordinates $\mathbf{R}(R, \theta, \phi)$, $\hat{\mathbf{r}}_1(\theta_1, \phi_1)$, $\hat{\mathbf{r}}_2(\theta_2, \phi_2)$, where \mathbf{R} stands for the intermolecular vector, $\hat{\mathbf{r}}_1$ and $\hat{\mathbf{r}}_2$ are the molecular axes vectors of CO_2 and N_2 respectively. The variational Schrödinger equation is solved using as a basis set the products of one-dimensional radial functions and angular functions. The most suitable angular functions are the coupled angular momentum functions, equation (6.7), which describe both the global rotation and the internal bending modes of motion of the complex.

A DVR based on the Coulomb Sturmian functions has been employed for describing the stretching motion along the \mathbf{R} vector. These functions are very efficient for reproducing the stretching motion of weakly bonded van der Waals systems as they not only have the proper anharmonic behavior but also provide a sparse DVR grid in the long-range. The matrix elements of the kinetic energy operator in this DVR have been described in detail in chapter 4.

8.2.1 The $\text{CO}_2\text{-N}_2$ PES

Recently, Nasri et al. [153] developed an accurate multi-dimensional interaction potential of the $\text{CO}_2\text{-N}_2$ electronic ground state. The PES was mapped along the four intermonomer Jacobi coordinates, namely the distance R connecting the CO_2 and N_2 centers of mass, the polar angles θ_1 and θ_2 of the rigid rotors CO_2 and N_2 respectively, and the torsional angle ϕ . This 4D-PES was generated at the CCSD(T)-F12/aug-cc-pVTZ level. Its main characteristics are depicted in Figure 8.1.

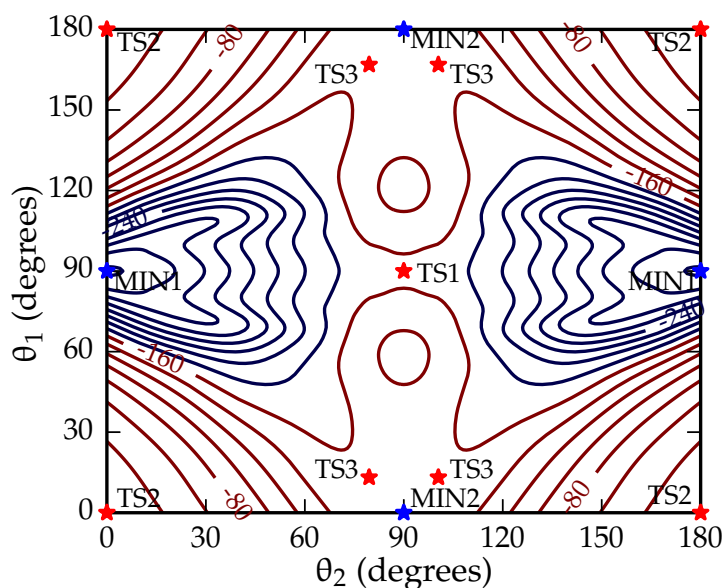


Figure 8.1: 2D contour plot of the PES for ϕ and R relaxed. The contour lines are equally spaced by 20 cm^{-1} .

Two types of minima (denoted as MIN1 and MIN2) and three types of saddle points (denoted as TS1, TS2 and TS3) can be located on this PES. TS1 and TS3 points are first-order saddle points while TS2 points are second-order saddle points (i.e. stationary points with two imaginary frequencies). Let us note that TS3 is determined in the present study and was not previously noticed by Nasri et al. [153]. TS1 connects the two equivalent MIN1 structures, while TS3 connects MIN1 and MIN2 structures. The transformation from one MIN1 structure to the other one is obtained by an out-of-plane rotation of N₂ within the complex. Similarly, upon inversion of the two oxygen atoms, there are two equivalent MIN2 structures and four equivalent TS3 saddle points. Geometrical data of the stationary points are collected in Table 8.1.

Table 8.1: Structural parameters of the CO₂-N₂ complex as deduced from the 4D-PES and experimentally [148]. See text for the definition of coordinates. For some points, ϕ is not defined (ND). MIN1, MIN2, TS2 and TS3 have two or four equivalent geometries. Only one is reported in this table. Other geometries can be obtained by symmetry operations.

	R (a ₀)	θ_1 (deg.)	θ_2 (deg.)	ϕ (deg.)	Energy (cm ⁻¹)
R _e /MIN1	6.98	90.0	0	ND	-321.24
R ₀	7.04	92.0	19.2	0	-
MIN2	8.47	0	90.0	ND	-158.90
TS1	6.42	90.0	90.0	90.0	-163.59
TS2	9.93	0	0	ND	-30.56
TS3	8.41	13.2	79.5	180.0	-158.12

The depths of the potential wells are D_e (MIN1) = 321.24 cm⁻¹ and D_e (MIN2) = 158.90 cm⁻¹ (with respect to separated CO₂ and N₂ monomers). TS1 is located at -163.58 cm⁻¹, TS2 at -30.56 cm⁻¹ and TS3 at -158.12 cm⁻¹. Since a potential energy barrier of 157.7 cm⁻¹ separates the two equivalent potential wells MIN1, bound states with localized wave functions in each potential well are expected. Systematic lifting of degeneracy due to tunneling effect (as in NH₃) should be observed. A splitting of $\sim 2 \times 10^{-4}$ cm⁻¹ has been predicted by a crude 1D model [148]. In contrast, the MIN2 potential well is so shallow that localized bound states cannot *a priori* be expected.

The CO₂-N₂ interaction potential is expanded in term of products of spherical harmonics, equation (7.18), where the summation is restricted to even values of $\lambda_1, \lambda_2, \lambda$. This form is less efficient to visualize and compute the angular dependence of the interaction, however it is more convenient for obtaining the mathematical expressions of the potential matrix elements in the angular basis set, as we have shown in chapter 7.

8.2.2 Symmetry of the CO₂-N₂ vibrational wave functions

The symmetry properties of the CO₂-N₂ system are characterized by the G₈ complete nuclear permutation inversion group [139] which results from the direct product of the permutation group of the indistinguishable oxygen atoms $S_2^{(O)} = \{E, (12)\}$, the permutation group of the indistinguishable N atoms $S_2^{(N)} = \{E, (34)\}$ and the inversion group $\mathcal{E} = \{E, E^*\}$. The resulting 8 operations $\{E, (12), (34), (12)(34), E^*, (12)^*, (34)^*, (12)(34)^*\}$ compose the G₈ group. The interaction potential and the total Hamiltonian are totally symmetric under all the operations of this group.

Consequently, every rovibrational wave function belongs to one of the 8 irreducible representations of the G₈ group. It can be noted that all stretching functions belong to the totally symmetric representation. Therefore, the symmetry of the rovibrational wave functions is directly obtained from the irreducible representations to which belong the functions of the rotational basis set. This requires the knowledge of the transformations of the space-fixed coordinates under the G₈ group operations. These transformations are given in Table 8.2.

Table 8.2: Transformations of the space-fixed Jacobi coordinates and parity of the angular functions defined by equation (6.7) under the operations of the G₈ group

	θ_1	φ_1	θ_2	φ	θ	φ	R	parity
E	θ_1	φ_1	θ_2	φ	θ	φ	R	1
(12)	$\pi - \theta_1$	$\pi + \varphi_1$	θ_2	φ	θ	φ	R	$(-1)^{j_1}$
(34)	θ_1	φ_1	$\pi - \theta_2$	$\pi + \varphi$	θ	φ	R	$(-1)^{j_2}$
(12)(34)	$\pi - \theta_1$	$\pi + \varphi_1$	$\pi - \theta_2$	$\pi + \varphi$	θ	φ	R	$(-1)^{j_1+j_2}$
E*	$\pi - \theta_1$	$\pi + \varphi_1$	$\pi - \theta_2$	$\pi + \varphi$	$\pi - \theta$	$\pi + \varphi$	R	$(-1)^{j_1+j_2+l}$
(12)*	θ_1	φ_1	$\pi - \theta_2$	$\pi + \varphi_2$	$\pi - \theta$	$\pi + \varphi$	R	$(-1)^{j_2+l}$
(34)*	$\pi - \theta_1$	$\pi + \varphi_1$	θ_2	φ_2	$\pi - \theta$	$\pi + \varphi$	R	$(-1)^{j_1+l}$
(12)(34)*	θ_1	φ_1	θ_2	φ_2	$\pi - \theta$	$\pi + \varphi$	R	$(-1)^l$

The transformations of the angular basis set, also shown in Table 8.2, are easily derived by making use of the spherical harmonics properties. The classification of the rovibrational wave functions according to the irreducible representations of G₈ are then obtained as a function of the parity of j_1 , j_2 , and l as shown in Table 8.3. These properties can be used to define a symmetry adapted basis set and lead to a considerable reduction of the size of the Hamiltonian matrices to be diagonalized.

8.3 Vibrational normal modes – asymmetric top model

The rovibrational states of a molecular system can be calculated with the combination of two approximate methods. First, with the harmonic approximation of the PES, reliable for small displacements around the equilibrium geometry, the internal vibrational motions are approximated by the normal modes of motion. Second, if

Table 8.3: Classification of the angular basis set functions according to the irreducible representation Γ_i of the G_8 group as a function of the parity, even (e) or odd (o), of j_1 , j_2 , and l .

j_1	j_2	l	Γ_i	j_1	j_2	l	Γ_i
e	e	e	A'_1	o	e	e	B''_1
e	e	o	A'_2	o	e	o	B''_2
e	o	e	B'_1	o	o	e	A''_1
e	o	o	B'_2	o	o	o	A''_2

we consider the molecule as a rigid body, the rotational states are easily calculated. The combination of these two approximations has shown to be a very useful tool to better understand the results of accurate calculations of fully coupled rovibrational motions [154, 155]. In this approach, the rovibrational wave functions of $\text{CO}_2\text{-N}_2$ are defined by a direct product of harmonic oscillator functions and asymmetric top rotational functions,

$$\Psi_{v_1, v_2, v_3, v_4}^{J_{K_a K_c}} = \prod_i^4 H_{v_i}(\chi_i) \sum_K A_K D_{MK}^J(\alpha, \beta, \gamma) \quad (8.1)$$

were $J_{K_a K_c}$ are the asymmetric top quantum numbers, v_i the vibrational quantum numbers, H_{v_i} the harmonic oscillator functions, χ_i the normal mode coordinates, and D_{MK}^J the symmetric top functions. The energy level are obtained as

$$E_{v_1, v_2, v_3, v_4}^{J_{K_a K_c}} = hc \sum_i^4 \nu_i \left(v_i + \frac{1}{2} \right) + E_{J_{K_a K_c}}(A, B, C) \quad (8.2)$$

with ν_i as the normal modes harmonic frequencies given in cm^{-1} , h and c are the Planck and speed of light constants respectively. $E_{J_{K_a K_c}}(A, B, C)$ is the energy of the $J_{K_a K_c}$ level of the asymmetric top as a function of the rotational constants. Analytical expressions for $E_{J_{K_a K_c}}(A, B, C)$ can be found elsewhere, for instance see reference [156].

The use of the latter formula requires the knowledge of the harmonic vibrational frequencies and the rotational constants. Harmonic frequencies are easily calculated within the normal mode analysis which is generally performed with the cartesian coordinates. In the case of the rigid rotor approximation, since some internal coordinates are replaced by constants, the cartesian coordinates cannot be used. Therefore we used the Wilson's FG method [141] which is based on internal coordinates.

The elements of the \mathbb{G} matrix have been determined following the methodology described by Wilson et al. [141]. The elements of the force constant matrix \mathbb{F} have been obtained by numerical differentiation. Diagonalization of the $\mathbb{G} \times \mathbb{F}$ leads to the harmonic frequencies and normal modes. On the other hand, the rotational constants can be obtained by the diagonalization of the inertia tensor for each equilibrium geometry.

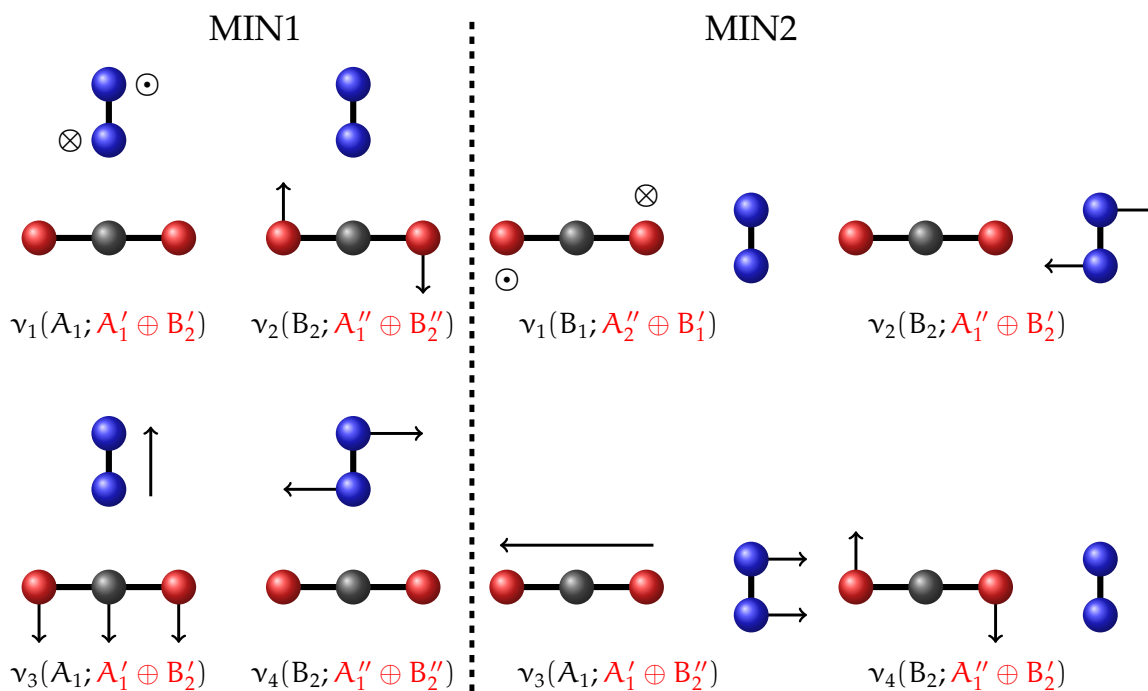


Figure 8.2: Intermonomer vibrational modes of the MIN1 and MIN2 structures. The representations to which each mode belongs are given for the C_{2v} (in black) and the G_8 (in red) groups.

Figure 8.2 depicts the vibrational normal modes of $\text{CO}_2\text{-N}_2$ for the MIN1 and MIN2 equilibrium structures determined with the Wilson's FG method. They correspond to the intermonomer stretching, the out-of-plane inversion of N_2 around its center of mass and the two in-plane bending motions

8.3.1 Symmetry considerations

The normal coordinates belong to the representations of the C_{2v} group. It is important to note that the C_{2v} group operations $\{E, C_2(\alpha), \sigma_{ab}, \sigma_{ac}\}$ operates on the vibrational displacements conversely to G_8 operation which permute identical nuclei and has no effect on vibrational displacement. The irreducible representations of C_{2v} to which belong the normal mode coordinates are given in Figure 8.2.

The representation to which belongs the total vibrational function is obtained from the direct product of the representations to which belong each of the four normal mode vibrational functions, as shown in Table 8.4.

The analysis of the asymmetric top wave functions requires the transformation of the Euler angles (α, β, γ) under the element group operations. To determine such transformations we replace each group element of C_{2v} by their equivalent rotation in the D_2 rotation group as shown in Table 8.5. The symmetry of the rotational wave function for a given state $J_{K_a K_c}$ is then determined using the asymmetric top symmetry rules [139]. The rovibrational wave functions are a direct product of the vi-

Table 8.4: Classification of the vibrational functions according to the irreducible representation of C_{2v} as a function of the parity, even (e) or odd (o), of the quantum numbers $\nu_1, \nu_2, \nu_3, \nu_4$.

ν_1	ν_2	ν_3	ν_4	Γ_{vib}	ν_1	ν_2	ν_3	ν_4	Γ_{vib}
e	e	e	e	A_1	o	e	e	e	B_1
e	e	e	o	B_2	o	e	e	o	A_2
e	e	o	e	A_1	o	e	o	e	B_1
e	e	o	o	B_2	o	e	o	o	A_2
e	o	e	e	B_2	o	o	e	e	A_2
e	o	e	o	A_1	o	o	e	o	B_1
e	o	o	e	B_2	o	o	o	e	A_2
e	o	o	o	A_1	o	o	o	o	B_1

 Table 8.5: Correspondences between the elements of the C_{2v}, D_2 groups and the subgroups of G_8 restricted to the global (MIN1) or the secondary minimum (MIN2). All these groups have the same character table. The representations to which belong the asymmetric top rotational functions are indicated in the last column, depending on the parity of K_a and K_c .

G_8	(MIN1) (MIN2)	E	(12) (34)	E^*	(12)* (34)*	Γ_{rot}
C_{2v}		E	$C_2(a)$	σ_{ab}	σ_{ac}	
D_2		R^0	R_a^π	R_c^π	R_b^π	$J_{K_a K_c}$
Γ_i :	A_1	1	1	1	1	e e
	A_2	1	1	-1	-1	e o
	B_1	1	-1	-1	1	o o
	B_2	1	-1	1	-1	o e

brational and rotational functions hence they belong to the representations $\Gamma_{\text{vib}} \times \Gamma_{\text{rot}}$.

We have now determined to which representations belong the vibrational functions in the limit of small displacements around the equilibrium geometry of the two structures MIN1 and MIN2. Applying the symmetry operation (34) on the structure MIN1, i.e. the permutation of the identical N atoms, we see there is two equivalent structures MIN1. Similarly, with the symmetry operation (12) which permutes identical O atoms, we have also two equivalent structures MIN2. Therefore, the global vibrational wave functions are obtained by the combinations of the doubly degenerate local wave functions pertaining to the MIN1 or MIN2 structures. The correspondences between the C_{2v} and G_8 irreducible representations are given in the Table 8.6. These correspondences are determined with the help of the character tables shown in Table 8.5 and in the appendix C

Table 8.6: Correspondences between the C_{2v} and G_8 irreducible representations for the two minima.

C_{2v}	$G_8(\text{MIN1})$	$G_8(\text{MIN2})$
$A_1 \oplus A_1$	$A'_1 \oplus B'_2$	$A'_1 \oplus B''_2$
$A_2 \oplus A_2$	$A'_2 \oplus B'_1$	$A'_2 \oplus B''_1$
$B_1 \oplus B_1$	$A''_2 \oplus B''_1$	$A''_2 \oplus B'_1$
$B_2 \oplus B_2$	$A''_1 \oplus B''_2$	$A''_1 \oplus B'_2$

8.4 Rovibrational bound states

Variationally, a total of 1091 bound states were found for $J = 0$. For the levels up to $\sim -83 \text{ cm}^{-1}$, Table 8.7 lists their energy, symmetry and parity. An attempt to assign vibrational quantum numbers to these levels was made, based not only on the vibrational normal modes-rigid rotor model but also through the examination of their 4D rovibrational wave functions.

Table 8.7: Lowest energy levels for $J = 0$ with their assigned vibrational quantum numbers $\nu_1, \nu_2, \nu_3, \nu_4$ whenever possible, parity ϵ , representation Γ_i of the group G_8 as well as the number of the level in a given representation. Energies are given in cm^{-1} with respect to the energy of separated monomers. Levels identified as the two components of a quasi-degenerate pair are listed on the same line. $|\Delta E|$ is the energy splitting due to tunneling. When possible, it is also indicated if the vibrational wave functions are mainly localized in MIN1 or MIN2 potential wells.

ν_1	ν_2	ν_3	ν_4	ϵ	Energy		Γ_i		$ \Delta E $	MIN
0	0	0	0	+	-224.68	-224.68	$A'_1.0$	$B'_2.0$	< 0.01	1
1	0	0	0	-	-192.44	-192.44	$A''_2.0$	$B''_1.0$	< 0.01	1
0	1	0	0	+	-178.79	-178.79	$B''_2.0$	$A''_1.0$	< 0.01	1
0	0	1	0	+	-178.36	-178.36	$A'_1.1$	$B'_2.1$	< 0.01	1
0	0	0	1	+	-173.53	-173.53	$B''_2.1$	$A''_1.1$	< 0.01	1
2	0	0	0	+	-164.00	-163.86	$A'_1.2$	$B'_2.2$	0.14	1
1	1	0	0	-	-150.52	-150.49	$B'_1.0$	$A'_2.0$	0.03	1
1	0	1	0	-	-149.78	-149.57	$A''_2.1$	$B''_1.1$	0.21	1
1	0	0	1	-	-143.49	-143.41	$A'_2.1$	$B'_1.1$	0.08	1
3	0	0	0	-	-139.97	-138.44	$A''_2.2$	$B''_1.2$	1.53	1
0	1	1	0	+	-138.79	-138.78	$B''_2.2$	$A''_1.2$	0.01	1
0	2	0	0	+	-138.21	-138.20	$A'_1.3$	$B'_2.3$	0.01	1
0	0	2	0	+	-136.72	-136.70	$A'_1.4$	$B'_2.4$	0.02	1
0	0	0	2	+	-132.95	-130.13	$A'_1.5$	$B'_2.5$	2.82	1
0	1	0	1	+	-132.93	-130.19	$B'_2.6$	$A'_1.6$	2.74	1

Continued on next page

8.4. ROVIBRATIONAL BOUND STATES

Table 8.7 – Continued from previous page

ν_1	ν_2	ν_3	ν_4	ϵ	Energy		Γ_i		$ \Delta E $	MIN
0	0	1	1	+	-130.94	-130.90	A_1'' .3	B_2'' .3	0.04	1
				+	-129.38		A_1' .7			1
				+	-125.38		B_2' .7			1
2	1	0	0	+	-127.74	-127.14	B_2'' .4	A_1'' .4	0.60	1
2	0	0	1	+	-120.71	-119.26	A_1'' .5	B_2'' .5	1.45	1
2	0	1	0	+	-119.7	-115.11	A_1' .8	B_2' .8	4.59	1
				-	-116.69		A_2'' .3			
0	0	0	0	+	-116.11	-116.11	B_2'' .6	A_1' .9	< 0.01	2
1	1	1	0	-	-114.82	-113.96	B_1' .2	A_2' .2	0.86	1
1	2	0	0	-	-113.73	-113.26	B_1'' .3	A_2'' .4	0.47	1
3	1	0	0	-	-111.76	-109.03	B_1' .3	A_2' .3	2.73	1
1	0	2	0	-	-110.38	-110.23	A_2'' .5	B_1'' .4	0.15	1
1	0	0	2	-	-107.84	-107.36	B_1'' .5	A_2'' .6	0.48	1
1	0	0	0	-	-107.69	-107.49	A_2'' .7	B_1' .4	0.2	2
3	0	0	1	-	-107.28	-97.83	A_2' .4	B_1' .6	9.45	1
0	3	0	0	+	-104.98	-104.79	B_2'' .7	A_1'' .6	0.19	1
0	2	1	0	+	-104.97	-104.81	A_1' .10	B_2' .9	0.16	1
1	0	1	1	-	-104.87	-101.54	B_1' .5	A_2' .5	3.33	1
0	1	0	0	+	-104.62	-104.62	B_2' .10	A_1'' .7	< 0.01	1
				+	-104.47		B_2'' .8			
				+	-104.19		A_1' .11			
				-	-103.39		A_2'' .8			
				-	-102.93		B_1'' .6			
0	1	2	0	+	-102.58	-101.97	B_2'' .9	A_1'' .8	0.61	1
2	0	0	0	+	-101.51	-101.26	B_2'' .10	A_1' .12	0.25	2
				-	-101.29		A_2'' .9			
0	0	3	0	+	-100.69	-100.66	B_2' .11	A_1' .13	0.03	1
0	2	0	1	+	-98.93	-98.68	A_1'' .9	B_2'' .11	0.25	1
				+	-98.46		A_1'' .10			
0	0	1	2	+	-97.57	-97.52	B_2' .12	A_1' .14	0.05	1
				+	-97.17		A_1' .15			
3	0	0	0	-	-96.94	-96.44	B_1' .7	A_2'' .10	0.5	2
				+	-96.42		B_2' .13			
				+	-95.2		A_1' .16			
0	1	0	2	+	-95.68	-95.68	B_2'' .12	A_1'' .11	< 0.01	1
				+	-95.06		B_2'' .13			
0	0	0	3	+	-94.86	-94.4	A_1'' .12	B_2'' .14	0.46	1

Continued on next page

Table 8.7 – *Continued from previous page*

ν_1	ν_2	ν_3	ν_4	ϵ	Energy	Γ_i	$ \Delta E $	MIN	
				+	-94.83	$B'_2.14$			
				-	-93.27	$B''_1.8$			
0	0	2	1	+	-93.13	$A''_1.13$	$B''_2.15$	0.34	1
2	1	1	0	+	-92.41	$A''_1.14$	$B''_2.16$	3.78	1
				+	-92.01	$B'_2.15$			
1	0	0	1	-	-91.91	$B''_1.9$	$A'_2.6$	0.04	2
				+	-91.62	$A'_1.17$			
0	2	0	0	+	-91.2	$A'_1.18$	$B''_2.17$	0.15	2
				+	-91.04	$A''_1.15$			
				+	-90.95	$A'_1.19$			
				-	-90.47	$A''_2.11$			
				+	-90.31	$B'_2.16$			
				+	-90.12	$A''_1.16$			
				-	-89.96	$B'_1.8$			
				+	-89.95	$A'_1.20$			
1	3	0	0	-	-89	$B'_1.9$	$A'_2.7$	2.72	1
				+	-88.7	$A'_1.21$			
				+	-88.18	$B'_2.17$			
0	0	0	1	+	-86.61	$B'_2.18$	$A''_1.14$	0.06	2
				-	-86.53	$B''_1.10$			
1	2	1	0	-	-86.24	$A''_2.12$	$B''_1.11$	0.81	1
				+	-84.99	$A''_1.18$			
				+	-84.75	$B'_2.19$			
				-	-84.71	$A'_2.8$			
				+	-84.32	$B''_2.18$			
0	0	1	0	+	-83.92	$A'_1.22$	$B''_2.19$	0.09	2
				+	-83.21	$A'_1.23$			

Systematic tunneling effects through the potential barrier connecting two equivalent structures are expected, where the global wave functions are no longer doubly degenerate. The splittings of the energy levels are listed in Table 8.7. For the lowest levels, we do not observe the corresponding splitting on the calculated energies. Since the numerical accuracy of our calculations is limited to 0.01 cm^{-1} , any splitting smaller than this limit cannot be calculated. Indeed, energy splitting could be as small as $\sim 2 \times 10^{-4} \text{ cm}^{-1}$, as shown by a simple 1D model [148]. For higher energy levels, the splitting is larger and can reach a few cm^{-1} . For instance, the excitation

8.4. ROVIBRATIONAL BOUND STATES

of the ν_1 mode of motion produces most of the largest energy splittings. Indeed, the ν_1 mode corresponds to an out-of-plane rotation of N_2 , it is thus strongly associated with the MIN1 \leftrightarrow MIN1 interconversion, as shown in Figure 8.2. Table 8.7 shows that this splitting goes from less than 0.01 cm^{-1} for MIN1 (0,0,0,0) level to more than 4 cm^{-1} for levels above the barrier, e.g. for MIN1 (3,0,0,0) level. For MIN2, since the barrier is very low, this effect is more pronounced when ν_1 is excited, for instance an appreciable splitting (of 0.2 cm^{-1}) is computed for MIN2 (1,0,0,0) state. In sum, we observe splittings for all the levels of this complex but in less extent (of few tenths of cm^{-1}) for ν_2, ν_3, ν_4 modes. This is due to the couplings between the ν_1 coordinate and the other vibrational modes coordinates as observed for NH_3 .

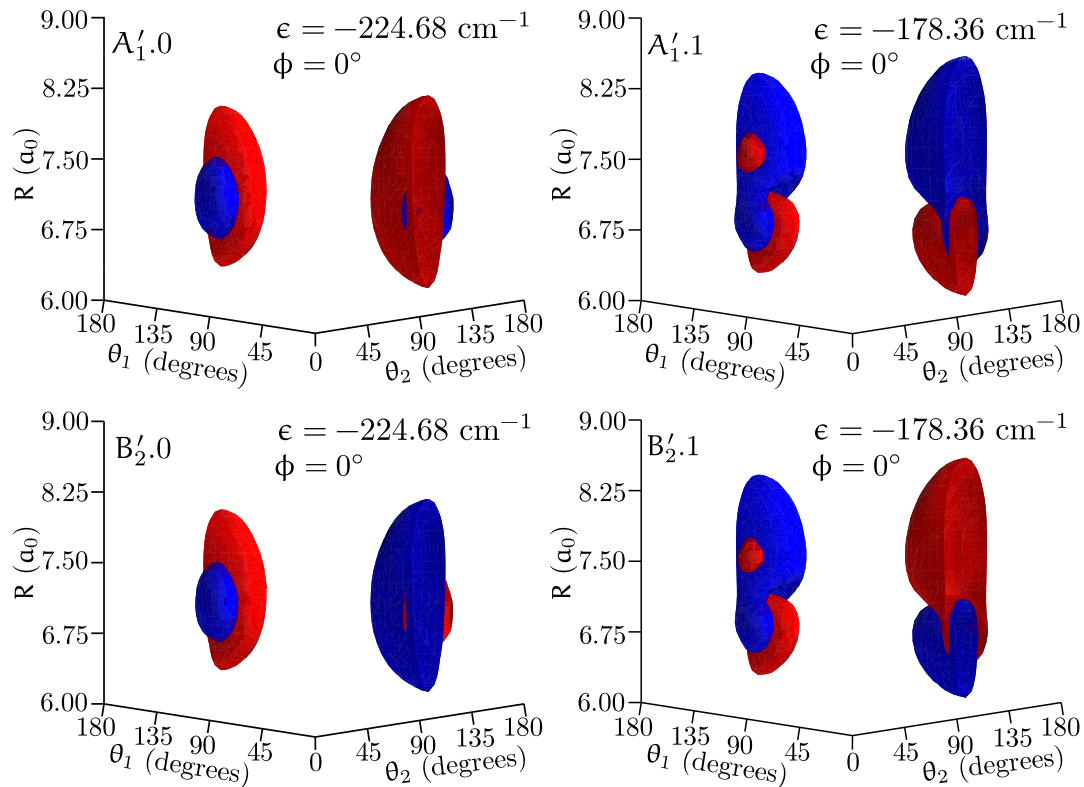


Figure 8.3: *Left panel:* 3D plot of the ground state quasi-degenerate wave functions. *Right panel:* 3D plot of the quasi-degenerate vibrational wave function of MIN1 (0,0,1,0) level. The A'_1 wave function is the symmetrical combination of the two wave functions localized in the equivalent MIN1 structures. The B'_2 wave function is the corresponding antisymmetrical combination.

Figure 8.3 displays the 3D contour plots of the quasi-degenerate ground state wave functions A'_1 and B'_2 . By definition, the B'_2 wave function has a nodal plane at $\theta_2 = 90^\circ$. However, Figure 8.3 reveals two additional and unexpected nodal planes (schematized by the change from blue to red). This is uncommon for a ground state wave function which is usually nodeless. Both wave functions are spread out across a large range of the R coordinate. This distance deviates greatly from the equilibrium

value of the global minimum MIN1, reflecting the occurrence of large amplitude motions and zero point vibrational energy effect. Furthermore, both polar angles θ_1 and θ_2 deviate significantly from their values at MIN1 equilibrium. This most likely induces distortions from the T-shape C_{2v} configuration as observed experimentally. Note that our A_0 , B_0 and C_0 rotational constants are in close agreement with those deduced by microwave spectroscopy [148] (Table 8.8). Such dynamical behaviors were proposed to explain the distorted C_{2v} planar structure of the H_2 - CO_2 complex [157]. Our work suggests to examine the corresponding vibrational wave functions for confirmation.

Table 8.8: Spectroscopic constants

Vibrational frequencies (cm^{-1})	MIN1			MIN2		
	Variational	Harmonic	Ref. [153]	Variational	Harmonic	Ref. [153]
ν_1	32.2	36.9	46	8.4	6.0	10
ν_2	45.9	50.7	32	29.5	30.8	42
ν_3	46.3	58.2	61	32.3	40.3	44
ν_4	51.2	60.5	88	11.5	10.8	17
Rotational constant (MHz)	Inertia			Inertia		
	Variational	tensor	Exp.[148]	Variational	tensor	Exp
A_0	11861.37	11702.98	11885.3	41500.51	60313.50	—
B_0	2087.97	2089.74	2062.88	1440.98	1306.05	—
C_0	1780.38	1773.12	1743.86	1240.81	1278.37	—
Rotation-vibration coupling constant (MHz)	α	β	γ	α	β	γ
	ν_1	807.29	20.65	6.01	—	—

The variationally determined fundamental frequencies and their harmonic counterpart are given in Table 8.8. For a given isomer, the differences between both sets of data evidence the strongly anisotropic character of the PES and the obvious importance of anharmonicities in the vibrational motions for this van der Waals complex. Table 8.7 reveals a high density of vibrational levels. This favors anharmonic resonances to take place between levels belonging to the same representation of G_8 group. Both the mixing of their unperturbed wave functions and the displacement of their energies are expected. For illustration, we display in Figure 8.3 the wave functions of the (0,0,1,0) levels. Figure 8.3 shows that the nodal planes are not parallel to the coordinate axes. Note that these levels belong to the same G_8 irreducible representation (A'_1 and B'_2) as the ground state. Both levels are close in energy, thus we expect a mixing among the A'_1 levels as well as among the B'_2 levels. More generally, these anharmonic resonances make difficult the assignment of quantum numbers to the levels of this complex, which should be viewed as tentative for some of the levels listed in Table 8.7.

Above the potential barrier of $MIN1 \leftrightarrow MIN1$ interconversion, several phenomena are taking place: vibrational quantum localization, anharmonic resonances and mixing of the wave functions pertaining to the non-equivalent MIN1 and MIN2

potential wells. For illustration, Figure 8.4 displays the wave functions of the $A'_1.0$, $A'_1.10$, $B''_2.6$, $B''_2.7$ levels. The wave function $B''_2.6$ is located significantly above TS3, but remains remarkably localized in the region of the MIN2 potential well. The $A'_1.10$ and $B''_2.7$ wave functions are also lying well above TS3. They are mainly localized in the MIN1 potential well with a small component in the MIN2 potential well. The right panel of Figure 8.4 provides some insight into the surprising localization of the wave functions. This figure shows the potential energy curve obtained by varying θ_1 while $\theta_2 = 0^\circ$ (the curve between MIN1 and TS2) and the potential energy curve obtained by varying θ_2 while $\theta_1 = 0^\circ$ (the curve between TS2 and MIN2). The extent of the wave functions is clearly limited by the potential energy curves resulting from these cuts of the 4D-PES, in spite that in some other directions the wave functions are free to extend as shown by the left panel of Figure 8.4. In fact, this vibrational memory effect can be observed for several wave functions regardless whether or not the corresponding rovibrational state energy is below or above the interconversion barriers $\text{MIN1} \leftrightarrow \text{MIN1}$ or $\text{MIN1} \leftrightarrow \text{MIN2}$. As a consequence, the assignment of these levels is relatively straightforward. As demonstrated for the $[\text{H,S,N}]^-$ system [105], these states conserve the memory of the equilibrium structure in the respective potential well above which they are located.

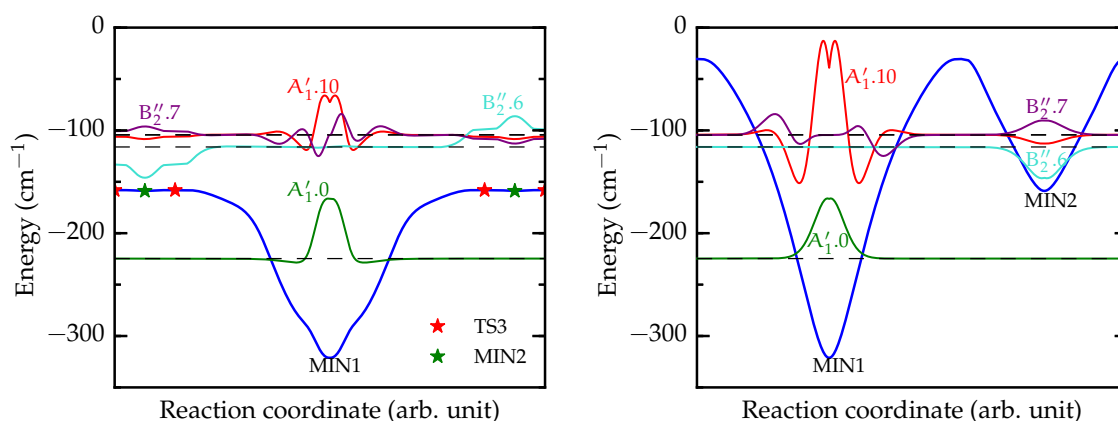


Figure 8.4: *Left panel*: Minimum energy path (blue line) between MIN1 and MIN2 minima and selected vibrational wave functions computed at the points of the minimum energy path. *Right panel*: Minimum energy path (blue line) between MIN1 and TS2 and between TS2 and MIN2 as well as selected vibrational wave functions computed at the points of the minimum energy path.

Localized vibrational states with an energy above the barrier separating two isomers have been observed previously in other molecular systems. This is the case for HCN and its isomer HNC, for which it was observed that a significant fraction of vibrational wave functions with energies above the isomerization barrier remains completely localized on one or the other side of the barrier [158]. These wave

functions are highly excited in one or both stretching motions with little excitation of the bending motion. In contrast, for the delocalized wave functions, the bending motion is highly excited. Indeed, the isomerization of HCN into HNC implies a rotation of H around CN, which is essentially triggered by the bending motion while the stretching motions have no effect on this rotation. A more complicated dynamics occurs in the $[\text{H,S,N}]^-$ system [105] which has two weakly bound isomeric complexes, namely $\text{SH}\cdots\text{N}^-$ and $\text{SN}\cdots\text{H}^-$. The rotation of H^- around SN produces three equilibrium configurations. Localized rovibrational wave functions with energy above the isomerization barriers have been observed. Again, excitation of the bending motion triggers isomerization while excitation of the stretching motions prevent isomerization. Let us note that the $\text{HCN} \leftrightarrow \text{HNC}$ and $[\text{H,S,N}]^-$ systems have two or more isomers separated by significant barriers. This means that every isomer corresponds to a potential well deep enough to support one or several bound states with energies below the corresponding barriers. A second class of systems is defined by the case where one isomer has one (or more) very low vibrational frequency and a very low energy barrier, significantly lower than the harmonic zero-point energy. In such case, the potential well is not deep enough to support even one localized vibrational level. The acetylene \leftrightarrow vinylidene isomerization and the MIN1 \leftrightarrow MIN2 isomerization of $\text{CO}_2\text{-N}_2$ belong to this second class. Vibrational states localized in the vicinity of the vinylidene minima have been obtained by accurate quantum calculations [159]. The acetylene \leftrightarrow vinylidene isomerization is triggered by the rotation of H atoms around the C_2 core, while the stretching and torsional motions have no effect on isomerization. The separation of the vibrational modes in two groups was recently illustrated by Baraban et al. [160]. The first group contains the active modes which trigger the isomerization process, while the modes of the second group are inactive (or spectator) modes. Inactive modes withhold vibrational energy in motions which cannot allow isomerization. Figure 8.1 suggests that the stretching motion along R or the torsional motion along ϕ are inactive modes for the MIN1 \leftrightarrow MIN2 isomerization. Rotation of N_2 or CO_2 appears to be the active modes. An investigation of the $\text{CO}_2\text{-N}_2$ PES in the vicinity of the MIN2 point shows, however, that the potential energy is repulsive when N_2 or CO_2 are rotated. This is in agreement with the harmonic vibrational modes depicted in Figure 8.2. A pure rotation of N_2 or CO_2 alone cannot lead to isomerization. Only a concerted rotation of N_2 and CO_2 , or in other words, only a particular combination of the two rotational motions, can lead to isomerization. Therefore, we may assume that the MIN2 localized states exist because the isomerization process is hindered.

The A_1' ground state wave function represented in Figure 8.4 has two nodes. These nodes are also observed in Figure 8.3. The PES along the minimum energy path is also plotted in Figure 8.4 and it can be seen that the nodal structure of the

wave function reflects the ripples of the PES. Let us note that the corrugated nature of the PES in the region of MIN1 potential well has been already observed by Nasri et al. [153]. More physical insight on this effect is provided by Figure 8.5. The two nodal planes are clearly related to the wavy PES.

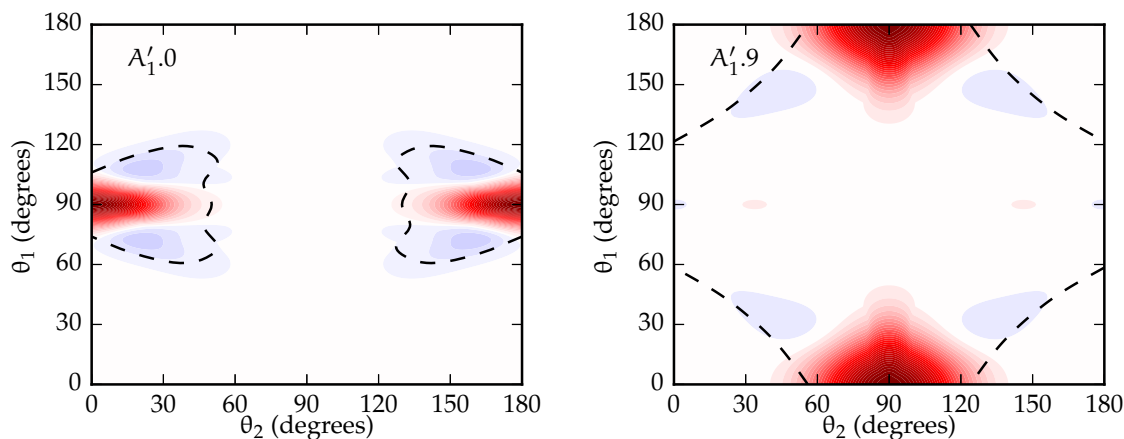


Figure 8.5: *Left panel*: 2D contour plot for the ground state wave function of MIN1. The black dashed line is the potential isoline equal to the energy of the ground state. *Right panel*: 2D contour plot for the ground state wave function of MIN2. For each point (θ_1, θ_2) , both the wave function and the potential energy have been calculated with the values of ϕ and R which minimize the potential energy. The black dashed line is the potential isoline equal to the energy of the bound state.

The localization of the $B_2'' .6$ wave function in the region of the MIN2 potential well is really surprising, since the energy of this vibrational state is about 42 cm^{-1} above the TS3 saddle point. This wave function corresponds to the ground state of the MIN2 potential well and is quasi-degenerate with the $A_1' .9$ wave function. Figure 8.5 gives a more detailed view of the latter wave function, along with a cut of the PES at the energy of this state. The $A_1' .9$ wave function is clearly the symmetric combination of two local wave functions pertaining to the MIN2 potential wells and do not spread out across the whole coordinate space energetically allowed. The small energy splitting between the $B_2'' .6$ and $A_1' .9$ is also an evidence of the localization of these wave functions. These levels are unusual and they are pointed out for the first time for a molecular system.

8.5 Rovibrational spectrum

A given rovibrational transition $i'J' \leftarrow ij$ of the complex will occur with the absorption or emission of a photon only if the matrix elements of the dipole moment operator $\hat{\mu}$ does not vanish and then the relative absorption coefficients at the tem-

perature T are proportional to:

$$\frac{g_I e^{-E_{i,J}/kT}}{Z(T)} (E_{i',J'} - E_{i,J}) \times \sum_{M,M',\Omega} |\langle i, J, M | \mu_\Omega | i', J', M' \rangle|^2 \quad (8.3)$$

where $Z(T)$ is the partition function, g_I is the spin-statistical weight and $|i, J, M\rangle$ is the wave function for the i th bound states. Symmetry consideration can be used to obtain some useful information such as selection rules and spin-statistical weight.

8.5.1 Dipole moment operator and selection rules

The dipole moment operator can be expressed in term of the space-fixed coordinates by expanding it in term of angular momentum functions, equation (6.7)

$$\hat{\mu} = \sum_{\Lambda, \Omega} \sum_{\text{all } \lambda} C_{\lambda_1 \lambda_2 \lambda_{12} \lambda_R}^{\Lambda, \Omega}(\mathbf{R}) y_{\lambda_1 \lambda_2 \lambda_{12} \lambda}^{\Lambda, \Omega}(\hat{\mathbf{R}}, \hat{\mathbf{r}}_1, \hat{\mathbf{r}}_2) \quad (8.4)$$

As the dipole moment operator is a first-rank tensor, the latter expansion is restricted to $\Lambda = 1$ and $\Omega = 0, \pm 1$. Additional restrictions in the expansion coefficients are deduced from the symmetry in the G_8 permutation-inversion group. First the dipole moment operator must be invariant to any permutation of equivalent nuclei and antisymmetric with respect to inversion. From Table 8.2 one can easily note that the only non-vanishing terms are those with λ_1, λ_2 even and λ odd. Using the classification given in Table 8.3 we can conclude that all the components of dipole moment operator belong to A'_2 representation and the only allowed transition are those whose rovibrational states are connected by A'_2 : $A'_1 \leftrightarrow A'_2$ and $B'_1 \leftrightarrow B'_2$. Besides the usual $\Delta J = 0, \pm 1$, the following symmetry imposed selection rules must also be satisfied : Δj_1 even, Δj_2 even, Δl even.

8.5.2 Nuclear spin wave function and spin statistic

Although the hyperfine structure has been neglected in the present study, the nuclear spins and the consequences of the spin statistics on the rovibrational spectra are of great importance. According to Bose-Einstein statistics, the total wave function must be symmetric under any permutation of identical nuclei. Since the electronic wave function is fully symmetric, the total wave function can be restricted here to the product of the rovibrational and nuclear spin wave functions. The CO_2 molecule ($I_O = 0, I_C = 0$) has only one nuclear spin state $I_{\text{CO}_2} = 0$ while in the case of N_2 molecule ($I_N = 1$) three nuclear spin states are possible $I_{\text{N}_2} = 0, 1, 2$. As a result of the coupling, the spin states of the complex are $I = 0, 1, 2$. Following the same convention as Frohman et al. [148] we denote *ortho* to the nuclear spin species with $I = 0, 2$ and *para* those with nuclear spin $I = 1$. The representation of G_8 generated by the spin function is $6A'_1 \oplus 3B'_2$ where the A'_1 correspond to the five components of the quintet ($I = 2$) and the singlet ($I = 0$) of complex while the B'_1 species correspond to the three components of the triplet ($I = 1$). Based on the

previous statement, the ro-vibrational states with symmetry A'_1 and A'_2 can only be combined with A'_1 nuclear spin state (*para*) while those with symmetry B'_1 and B'_2 can only be combined with B'_2 spin states (*ortho*). Rovibrational states of symmetry A''_1 , A''_2 , B''_1 , and B''_2 are, however, forbidden by Bose-Einstein statistics. These restrictions are the origin of the statistical weights shown in Table 8.9. Furthermore, the *ortho* intensities are expected to be twice the *para* intensities.

Table 8.9: The statistical weight (Stat. wt) of the rovibrational states of $\text{CO}_2\text{-N}_2$ in the G_8 group.

Γ_{rovib}	Stat. wt	Γ_{rovib}	Stat. wt
A'_1	6	B'_1	3
A''_1	0	B''_1	0
A'_2	6	B'_2	3
A''_2	0	B''_2	0

8.5.3 Comparison with experiments

A way to estimate the accuracy of not only the present variational calculations but also the PES itself, is to compare the calculated frequencies with the experimental determinations. The FTMW spectra of the $\text{CO}_2\text{-N}_2$ complex have been recently measured by Frohman et al. [148]. The reported frequencies correspond to pure rotational transitions with $K_a = 0$ and $\Delta K_a = 0$ as well as hyperfine transitions. The lack of transitions with $\Delta K_a \neq 0$ is well explained by symmetry imposed selection rules $A'_1 \leftrightarrow A'_2$ and $B'_1 \leftrightarrow B'_2$ which, for the ground state, correspond to transitions of type $J_{e'o} - J'_{ee}$. A comparison of the aforementioned results (neglecting hyperfine structure) with those obtained from our variational approach is shown in Table 8.10.

Table 8.10: Calculated and experimental frequencies (MHz) for the transitions $J_{K'_a K'_c} - J_{K_a K_c}$. Relative errors from experimental data are given in percent.

$J_{K'_a K'_c} - J_{K_a K_c}$	This work	Exp. [148]	rel. error %
$1_{01} - 0_{00}$	3880.484	—	—
$2_{02} - 1_{01}$	7527.429	7608.377	1.06
$3_{03} - 2_{02}$	11277.417	11388.436	0.97
$4_{04} - 3_{03}$	15003.717	15148.195	0.95
$5_{05} - 4_{04}$	18698.230	18877.125	0.95

The experimental frequencies are reported for transitions between rotational and hyperfine levels. Since the hyperfine structure has been neglected in the present calculations, we have selected the experimental transitions with $I = I' = 0$ (which happen only for *ortho* states) for comparison with the calculated frequencies. The agreement between the calculated and experimental frequencies is quite good, within

approximately 1 %, which represents a maximum deviation of 0.006 cm^{-1} . This allows us to conclude that the 4D-PES model provides an accurate description of the interaction energy of the $\text{CO}_2\text{-N}_2$ van der Waals complex.

8.6 Conclusion

Accurate calculations of the intermonomer vibrational bound states of the $\text{CO}_2\text{-N}_2$ van der Waals system have been presented. The effects of the permutations of indistinguishable atoms have been considered and investigated. The most notable effect is the existence of symmetrically equivalent potential wells leading to systematic lifting of degeneracy induced by tunneling effects. The examination of wave functions has revealed unexpected features: the ground state wave function has several nodal planes and the wave functions of highly excited states remain localized in small regions of the coordinate space. A good agreement with the experimental rotational transition energies has been obtained, thus demonstrating the accuracy of the 4D-PES model and validating the nuclear motion treatment.

In spite of its importance for atmospheric chemistry, our work reveals that the structure and the spectroscopy of the $\text{CO}_2\text{-N}_2$ complex are governed by full quantum effects, including tunneling, large amplitude motions, anharmonic resonances and vibrational quantum localization. Their spectroscopic signatures were already observed experimentally and are explained here for the first time. The plural potential induced complex dynamics could be found in several organic and inorganic molecules such as those presenting several conformers (e.g., *cis-trans*), isomers and tautomers (enol-keto) interacting mutually on the same PES. The present work suggests that their spectroscopy and dynamics cannot be fully understood without considering quantum tunneling.

General conclusions

In the first part of this thesis dedicated to the possible mechanisms of formation and destruction of anions, a new method based on a body fixed single-center approach and the use of Dyson orbitals was developed for the calculation of REA and PD cross sections. The accuracy of this method was successfully benchmarked against previously reported experimental and theoretical data for O_2^- , OH^- , CN^- . It was however not tested for strongly polar molecules and we recommend to test it beforehand in this case as our approach is based on a body fixed approach which could not be appropriate. We also found that the FBA gives good results for these three systems studied. In other words a plane wave is a good approximation of the scattering wave of the ejected electron in the case of the PD of an anion or for the impinging electron in the case of the REA by a non strongly polar neutral molecule. In this case the long-range interaction potential between the leaving or impinging electron and the neutral molecule is relatively low. Owing to its simplicity, the use of the FBA drastically reduces the computation time. It is expected to work well for REA when the kinetic energy of the electron is large compared to the electron affinity of the target molecule. We then suggest that the scattered wave should be preferred for REA calculations at very low energy.

Two approaches were also tested for simplifying the calculation of the Dyson orbital: namely KS and HF frozen-core orbitals. They were tested against the exact CASSCF results. We found that KS orbitals reproduce the right energy dependence of the cross sections but fail to estimate their absolute magnitudes. The HF frozen-core approximation moderately underestimates the cross sections as it neglects the electron-correlation. Therefore we conclude that the HFFC approach may provide a reasonable first estimate of the Dyson orbital when the size of the system prohibits the use of exact CASSCF calculations.

The effects of the size and the type of the basis set used to calculate the Dyson orbital were also investigated. We found that the basis set must include very diffuse functions in order to properly describe the Dyson orbitals. Consequently we recommend using STO basis sets as the best one for performing REA or PD calculations. Unfortunately these basis sets are not currently included in the most widely used electronic structure software. A good accuracy may alternatively be reached

by using GTO basis set approaching the complete basis set limit.

Taking advantage of the reduced computation time offered by the FBA, we calculated the REA and PD cross sections for the six detected anion and other potential candidates belonging to the families C_n^- , C_nH^- , C_nN^- and HC_nO^- . These cross sections were then used to calculate the corresponding PD and REA rates. We find that the calculated rates are very small suggesting that the inclusion of these calculated PD rates in the astrochemical model will decrease the fractional abundance of these anions, thus deteriorating the current agreement between models and observations. We furthermore conclude that the values of the calculated REA rates are too small to explain the formation of anions in the interstellar medium suggesting that other mechanisms have to be considered. We also expect that the method developed here for the study of REA and PD could be straightforwardly extended to the study of electron recombination with a cationic molecule and to the photo-ionization of neutral molecules, these two processes being of great interest for both astrochemistry and plasma physics.

The second part of this thesis was dedicated to the rotational excitation and de-excitation of C_3N^- by collision with He and H_2 . Two analytical models of the corresponding PES has been developed from a large set of high-level ab-initio calculations. We took a special care in describing the analytical long-range interactions which were found to be in excellent agreement with the ab-initio results.

The bound states of the $He-C_3N^-$ and $H_2-C_3N^-$ complexes were then variationally calculated using these PESs and a Sturmian DVR. The detailed analysis of the bound states wave functions for these two systems revealed some interesting features such as vibrational quantum memory, tunneling splitting as well as anharmonic resonances. Tunneling splitting for example leads to the lifting of the degeneracy of bound states belonging to equivalent potential wells in the $H_2-C_3N^-$ van der Waals complex. Vibrational frequencies and rotational constant for both complexes have also been computed. These results show that a full quantum treatment of the nuclei movement is required to obtain accurate bound state energies for these anionic van der Waals complexes.

State to state rotational excitation and de-excitation rates of C_3N^- by collision with H_2 and He in the temperature interval [10, 300] K were then obtained by combining CC calculations and the UJS procedure. In the case of collision with He a strong propensity rule to favor $|\Delta j_{C_3N^-}| = 2$ was found while for large $\Delta j_{C_3N^-}$, odd $\Delta j_{C_3N^-}$ are favored. Conversely, for collision with both *ortho*- and *para*- H_2 a propensity to favor $|\Delta j_{C_3N^-}| = 1$ is clearly at work. Another important result for this system lies in the close resemblance, especially at higher temperatures, between *ortho*- and *para*- H_2 rates which is attributed to the angular anisotropy and to the strength of the short-range interaction. We also explore the validity of scaling the He rate co-

efficients by using the ratio of the reduced masses in order to estimate the *para*-H₂ rates. We found that the use of this approximation leads to relatively large error (< 50%) and to false propensity rules.

We also evaluated the accuracy of the estimation of the rate coefficient for rotational relaxation of C₃N⁻ by collision with H₂ from the available rates for CN⁻ and C₆H⁻. We found that the agreement between the CN⁻ and C₃N⁻ rates is relatively good only for transitions with small $|\Delta j|$ while for larger values of $|\Delta j|$ CN⁻ rates are smaller than the C₃N⁻ ones. We think that these differences come from the difference of size of the CN⁻ and C₃N⁻ molecules. The bigger the molecule the most repulsive will be the short-range potential thus enhancing transition with large transferred angular momentum $|\Delta j|$. The results for C₆H⁻, are conversely in remarkably good agreement with those for C₃N⁻ for all the transitions. We then suggest that similar effect to those found for C₃N⁻ and C₆H⁻ could also be seen for larger chains of their respective families C_{2n+1}N⁻ and C_{2n}H⁻ for which rotational relaxation rates could be estimated from the former ones.

Appendix A

Dyson orbital calculation

Let us consider a N-electrons molecular system, neutral or anionic. After ionization or electron detachment, this system has lost one electron. If the electronic wavefunctions are expanded over a set of determinants, such as CASSCF or CI wavefunctions,

$$\Phi^N(x_1, x_2, \dots, x_N) = \sum_{k=1}^{k_{\max}} C_k^N \Psi_k^N(x_1, x_2, \dots, x_N) \quad (\text{A.1})$$

$$\begin{aligned} \Phi^{N-1}(x_1, x_2, \dots, x_{N-1}) = \\ \sum_{l=1}^{l_{\max}} C_l^{N-1} \Psi_l^{N-1}(x_1, x_2, \dots, x_{N-1}) \end{aligned} \quad (\text{A.2})$$

then the Dyson orbital [58, 59, 161] is defined by

$$\begin{aligned} \varphi^D(x_N) = \sqrt{N} \sum_{l=1}^{l_{\max}} C_l^{N-1} \sum_{k=1}^{k_{\max}} C_k^N \\ \times \int dx_1 dx_2 \dots dx_{N-1} \Psi_k^N(x_1, x_2, \dots, x_N) \\ \times \Psi_l^{N-1}(x_1, x_2, \dots, x_{N-1}) \end{aligned} \quad (\text{A.3})$$

We detail below how to calculate the (N-1)-dimensional integral, following closely Arbelo-González et al.[161]

Any N-electrons Slater determinant can be rewritten as

$$\begin{aligned} \Psi_k^N(x_1, x_2, \dots, x_N) = \\ \frac{1}{\sqrt{N}} \sum_{i=1}^N (-1)^{N+i} \psi_{ki}^{N-1}(x_1, x_2, \dots, x_{N-1}) \chi_{d_{ki}}(x_N) \end{aligned} \quad (\text{A.4})$$

where $\psi_{ki}^{N-1}(x_1, x_2, \dots, x_{N-1})$ is the minor determinant obtained by removing the column i and the line N from the determinant $\Psi_k^N(x_1, x_2, \dots, x_N)$, and where $\chi_{d_{ki}}$ is the molecular spin-orbital appearing at column i in determinant k . The spin-orbital number is given by the function d_{ki} . Using equation (A.4), the equation (A.3) can

be rewritten

$$\begin{aligned}
 \varphi^D(x_N) &= \sum_{l=1}^{l_{\max}} C_l^{N-1} \sum_{k=1}^{k_{\max}} C_k^N \sum_{i=1}^N (-)^{N+i} \chi_{d_{ki}}(x_N) \\
 &\times \int dx_1 dx_2 \cdots dx_{N-1} \Psi_l^{N-1}(x_1, x_2, \cdots, x_{N-1}) \\
 &\times \psi_{ki}^{N-1}(x_1, x_2, \cdots, x_{N-1})
 \end{aligned} \tag{A.5}$$

The summation on k runs on all determinants of the N -electrons system, and the summation on i runs on all occupied spin-orbitals of the determinant k . Thus we can replace the summation on i by a summation on all spin-orbitals of the N -electrons system. Let us define the b coefficients such as

$$\begin{aligned}
 b_{d_{ki}} &= \sum_{l=1}^{l_{\max}} C_l^{N-1} C_k^N (-)^{N+i} \\
 &\times \int dx_1 dx_2 \cdots dx_{N-1} \Psi_l^{N-1}(x_1, x_2, \cdots, x_{N-1}) \\
 &\times \psi_{ki}^{N-1}(x_1, x_2, \cdots, x_{N-1})
 \end{aligned} \tag{A.6}$$

$$\varphi^D(x_N) = \sum_{k=1}^{k_{\max}} \sum_{i=1}^N b_{d_{ki}} \chi_{d_{ki}}(x_N) \tag{A.7}$$

d_{ki} will run on all the spatial orbital which are occupied at least one times in the list of the determinants. d_{ki} gives also the spin state. Thus all the quantities $b_{d_{ki}}$ which belong to the same spatial orbital j and spin state σ can be summed and the equation (A.7) can be rewritten

$$\varphi^D(x_N) = \sum_{j=1}^{N_o} \sum_{\sigma=\alpha,\beta} b_{j\sigma} \chi_{j\sigma}(x_N) \tag{A.8}$$

where N_o is the number of spatial orbitals (atomic or molecular).

The determination of the coefficients $b_{d_{ki}}$ involves the calculation of the $(N-1)$ -dimensional integral

$$\begin{aligned}
 I_{lki} &= \int dx_1 dx_2 \cdots dx_{N-1} \Psi_l^{N-1}(x_1, x_2, \cdots, x_{N-1}) \\
 &\times \psi_{ki}^{N-1}(x_1, x_2, \cdots, x_{N-1})
 \end{aligned} \tag{A.9}$$

The integral involves the product of two Slater determinants built over two non-orthogonal spin-orbital basis sets. The $(N-1)$ -dimensional integral can be reorga-

nized into an antisymmetrized product of (N-1) 1D integrals

$$\begin{aligned}
 I_{lki} = & \sum_{p \in S_n} (-)^p \hat{P} \int dx \varphi_{d_{l1}}(x) \chi_{d_{k1}}(x) \\
 & \times \int dx \varphi_{d_{l2}}(x) \chi_{d_{k2}}(x) \cdots \\
 & \times \int dx \varphi_{d_{l(i-1)}}(x) \chi_{d_{k(i-1)}}(x) \\
 & \times \int dx \varphi_{d_{li}}(x) \chi_{d_{k(i+1)}}(x) \cdots \\
 & \times \int dx \varphi_{d_{l(N-1)}}(x) \chi_{d_{kN}}(x)
 \end{aligned} \tag{A.10}$$

where the antisymmetrization operator acts over the $\chi_{d_{ki}}$ functions. This can be also written as a determinant in which appear the overlaps of every occupied molecular orbitals of the N-electrons system with every occupied molecular orbitals of the (N-1)-electrons system.

The functions $\varphi_{d_{lj}}$ and $\chi_{d_{ki}}$ are spin-orbitals, i.e. the products of a spin function $\sigma \in [\alpha, \beta]$ and a spatial molecular orbital. The latter are expanded over the spatial atomic orbitals basis set. Let us recall that both N-electrons and (N-1)-electrons systems have the same atomic orbitals basis set, the same geometry, but different molecular orbitals basis sets. Therefore, the overlaps between spin-orbitals appearing in equation (A.10) are calculated with

$$\langle \varphi_{d_{li}} | \chi_{d_{kj}} \rangle = \delta_{\sigma_{d_{li}}, \sigma_{d_{kj}}} \sum_{m=1}^{N_o} \sum_{n=1}^{N_o} u_{m d_{li}} v_{n d_{kj}} S_{mn} \tag{A.11}$$

where u and v are the LCAO coefficients and S the atomic orbital overlap matrix.

Appendix B

J-shifting approaches

The rate coefficients for an inelastic process at a given temperature T are calculated as

$$k(T) = \sqrt{\frac{8}{\pi\mu}} (k_B T)^{-\frac{3}{2}} \int_0^{\infty} E \sigma(E) e^{-\frac{E}{k_B T}} dE \quad (\text{B.1})$$

where μ is the reduced mass of the system, E the collision energy and σ is the inelastic cross section which in turn is defined as

$$\sigma(E) = \frac{\pi}{2\mu E} \sum_J (2J+1) P^J(E) \quad (\text{B.2})$$

with $P^J(E)$ as the average transition probability or opacity function for the total angular momentum quantum number J . Equation (B.1) can be rewritten as

$$k(T) = \sqrt{\frac{2\pi}{(\mu k_B T)^3}} \sum_J (2J+1) \int_0^{\infty} P^J(E) e^{-\frac{E}{k_B T}} dE \quad (\text{B.3})$$

Let us suppose that we only know the opacity function for a given value of J , say $J = 0$, and want to compute the rate coefficient. A simple approach is the so called standard J-shifting method in which the missing values are approximated as follow

$$P^J(E) \approx P^0(E - BJ(J+1)) \quad (\text{B.4})$$

where B is known as the shifting constant. Substitution of equation (B.4) into equation (B.3) leads to

$$k(T) = \sqrt{\frac{2\pi}{(\mu k_B T)^3}} \sum_J (2J+1) \int_0^{\infty} P^0(E - BJ(J+1)) e^{-\frac{E}{k_B T}} dE \quad (\text{B.5})$$

By using the variable substitution $E' = E - BJ(J+1)$ the above expression can be simplified to give

$$k(T) = k^0(T) \sum_J (2J+1) e^{-\frac{BJ(J+1)}{k_B T}} \quad (\text{B.6})$$

where

$$k^0(T) = \sqrt{\frac{2\pi}{(\mu k_B T)^3}} \int_0^{\infty} P^0(E) e^{-\frac{E}{k_B T}} dE \quad (\text{B.7})$$

The main deficiencies of the standard J-shifting are associated with the selection of the shifting constant B. The selection of B is to some extent arbitrary and consequently, the computed rate coefficients may have large uncertainties associated with it.

Let us now suppose that besides the opacity function for $J = 0$ we also have the opacity function for a nonzero value of J, then by requiring that

$$\int_0^{\infty} P^J(E) e^{-\frac{E}{k_B T}} dE = \int_0^{\infty} P^0(E - BJ(J+1)) e^{-\frac{E}{k_B T}} dE \quad (\text{B.8})$$

we can obtain the shifting constant B in a non-arbitrary way as

$$B(T) = \frac{k_B T}{J(J+1)} \ln \left[(2J+1) \frac{k^0}{k^J} \right] \quad (\text{B.9})$$

where k^J is defined similarly to k^0 ,

$$k^J(T) = \sqrt{\frac{2\pi}{(\mu k_B T)^3}} \int_0^{\infty} (2J+1) P^J(E) e^{-\frac{E}{k_B T}} dE \quad (\text{B.10})$$

The previous approach is known as uniform J-shifting and was introduced by Zhang and Zhang [122]. The physical significance of equation (B.8) is that it guarantees that the fitted probability function $P_{\text{fit}}^J(E) = P^0(E - BJ(J+1))$ gives the exact contribution to the rate coefficient as the original probability function $P^J(E)$ at the given temperature T.

In practical application it is desirable to calculate the opacity function for more than two values of J in order to obtain more accurate result. In this case the shifting constant B at a given temperature for $J \in [J_i, J_{i+1})$

$$B_i(T) = \frac{k_B T}{J_{i+1}(J_{i+1}+1) - J_i(J_i+1)} \ln \left(\frac{2J_{i+1}+1}{2J_i+1} \frac{k^{J_i}}{k^{J_{i+1}}} \right) \quad (\text{B.11})$$

Once $B_i(T)$ is obtained the contribution k^J is obtained as follow

$$k^J(T) = \frac{2J+1}{2J_i+1} k^{J_i}(T) \exp \left\{ -\frac{B_i(T) [J(J+1) - J_i(J_i+1)]}{k_B T} \right\} \quad (\text{B.12})$$

Appendix C

The character tables

Due to its importance in the present study, we give the character table and the multiplication table of the G_4 and G_8 group which are not easily found in the literature.

The G_4 group

Table C.1: Character table of the G_4 group.

$\Gamma_i :$	E	(12)	E^*	$(12)^*$
A_1	1	1	1	1
A_2	1	1	-1	-1
B_1	1	-1	-1	1
B_2	1	-1	1	-1

Table C.2: Multiplication table of the G_4 group.

$\Gamma_i :$	A_1	A_2	B_1	B_2
A_1	A_1	A_2	B_1	B_2
A_2	A_2	A_1	B_2	B_1
B_1	B_1	B_2	A_1	A_2
B_2	B_2	B_1	A_2	A_1

The G_8 group

Table C.3: Character table of the G_8 group.

$\Gamma_i :$	E	(12)(34)	E^*	$(12)(34)^*$	(12)	(34)	$(12)^*$	$(34)^*$
A'_1	1	1	1	1	1	1	1	1
A''_1	1	1	1	1	-1	-1	-1	-1
A'_2	1	1	-1	-1	1	1	-1	-1
A''_2	1	1	-1	-1	-1	-1	1	1
B'_1	1	-1	-1	1	1	-1	-1	1
B''_1	1	-1	-1	1	-1	1	1	-1
B'_2	1	-1	1	-1	1	-1	1	-1
B''_2	1	-1	1	-1	-1	1	-1	1

Table C.4: Multiplication table of the G_8 group.

$\Gamma_i :$	A'_1	A'_2	B'_1	B'_2	A''_1	A''_2	B''_1	B''_2
A'_1	A'_1	A'_2	B'_1	B'_2	A''_1	A''_2	B''_1	B''_2
A'_2	A'_2	A'_1	B'_2	B'_1	A''_2	A''_1	B''_2	B''_1
B'_1	B'_1	B'_2	A'_1	A'_2	B''_1	B''_2	A''_1	A''_2
B'_2	B'_2	B'_1	A'_2	A'_1	B''_2	B''_1	A''_2	A''_1
A''_1	A''_1	A''_2	B''_1	B''_2	A'_1	A'_2	B'_1	B'_2
A''_2	A''_2	A''_1	B''_2	B''_1	A'_2	A'_1	B'_2	B'_1
B''_1	B''_1	B''_2	A''_1	A''_2	B'_1	B'_2	A'_1	A'_2
B''_2	B''_2	B''_1	A''_2	A''_1	B'_2	B'_1	A'_2	A'_1

Bibliography

- [1] A. Dalgarno and R. A. McCray. The formation of interstellar molecules from negative ions. *ApJ*, 181:95–100, 1973.
- [2] E. Herbst. Can negative molecular ions be detected in dense interstellar clouds? *Nature*, 289(5799):656–657, 1981.
- [3] M. Tulej, D. A. Kirkwood, M. Pachkov, and J. P. Maier. Gas-phase electronic transitions of carbon chain anions coinciding with diffuse interstellar bands. *ApJ*, 506(1):L69, 1998.
- [4] R. Terzieva and E. Herbst. Radiative electron attachment to small linear carbon clusters and its significance for the chemistry of diffuse interstellar clouds. *Int. J. Mass Spectrom.*, 201(1):135 – 142, 2000.
- [5] B. J. McCall, J. Thorburn, L. M. Hobbs, T. Oka, and D. G. York. Rejection of the C_7^- diffuse interstellar band hypothesis. *ApJ*, 559(1):L49, 2001.
- [6] Y. Morisawa, H. Hoshina, Y. Kato, Z. Simizu, S. Kuma, N. Sogoshi, M. Fushitani, S. Watanabe, Y. Miyamoto, T. Momose, Y. Kasai, and K. Kawaguchi. Search for CCH^- , NCO^- , and NCS^- negative ions in molecular clouds. *Publ. Astron. Soc. Japan*, 57(2):325–334, 2005.
- [7] M. C. McCarthy, C. A. Gottlieb, H. Gupta, and P. Thaddeus. Laboratory and astronomical identification of the negative molecular ion C_6H^- . *ApJ*, 652(2):L141, 2006.
- [8] T. J. Millar, C. Walsh, and T. A. Field. Negative ions in space. *Chem. Rev.*, 117(3):1765–1795, 2017. PMID: 28112897.
- [9] S. Brünken, H. Gupta, C. A. Gottlieb, M. C. McCarthy, and P. Thaddeus. Detection of the carbon chain negative ion C_8H^- in TMC-1. *ApJ*, 664(1):L43, 2007.
- [10] P. Thaddeus, C. A. Gottlieb, H. Gupta, S. Brünken, M. C. McCarthy, M. Agúndez, M. Guélin, and J. Cernicharo. Laboratory and astronomical detection of the negative molecular ion C_3N^- . *ApJ*, 677(2):1132, 2008.

- [11] M. Agúndez, J. Cernicharo, M. Guélin, M. Gerin, M. C. McCarthy, and P. Thaddeus. Search for anions in molecular sources: C_4H^- detection in L1527. *A&A*, 478(1):L19–L22, 2008.
- [12] N. Sakai, T. Sakai, T. Hirota, and S. Yamamoto. Abundant carbon-chain molecules toward the low-mass protostar IRAS 04368+2557 in L1527. *ApJ*, 672(1):371, 2008.
- [13] M. A. Cordiner, J. V. Buckle, E. S. Wirström, A. O. H. Olofsson, and S. B. Charnley. On the ubiquity of molecular anions in the dense interstellar medium. *ApJ*, 770(1):48, 2013.
- [14] H. Gupta, C. A. Gottlieb, M. C. McCarthy, and P. Thaddeus. A survey of C_4H , C_6H , and C_6H^- with the Green Bank Telescope. *ApJ*, 691(2):1494, 2009.
- [15] N. Sakai, T. Shiino, T. Hirota, T. Sakai, and S. Yamamoto. Long carbon-chain molecules and their anions in the starless core, Lupus-1A. *ApJ*, 718(2):L49, 2010.
- [16] M. A. Cordiner, S. B. Charnley, J. V. Buckle, C. Walsh, and T. J. Millar. Discovery of interstellar anions in cepheus and auriga. *ApJ*, 730(2):L18, 2011.
- [17] N. Sakai, T. Sakai, Y. Osamura, and S. Yamamoto. Detection of C_6H^- toward the low-mass protostar IRAS 04368+2557 in L1527. *ApJ*, 667(1):L65, 2007.
- [18] A. J. Remijan, J. M. Hollis, F. J. Lovas, M. A. Cordiner, T. J. Millar, A. J. Markwick-Kemper, and P. R. Jewell. Detection of C_8H^- and comparison with C_8H toward IRC +10216. *ApJ*, 664(1):L47, 2007.
- [19] J. Cernicharo, M. Guélin, M. Agúndez, K. Kawaguchi, M. McCarthy, and P. Thaddeus. Astronomical detection of C_4H^- , the second interstellar anion. *A&A*, 467(2):L37–L40, 2007.
- [20] J. Cernicharo, M. Guélin, M. Agúndez, M. C. McCarthy, and P. Thaddeus. Detection of C_5N^- and vibrationally excited C_6H in IRC +10216. *ApJ*, 688(2):L83, 2008.
- [21] M. Agúndez, J. Cernicharo, M. Guélin, C. Kahane, E. Roueff, J. Kłos, F. J. Aoiz, F. Lique, N. Marcelino, J. R. Goicoechea, M. G. García, C. A. Gottlieb, M. C. McCarthy, and P. Thaddeus. Astronomical identification of CN^- , the smallest observed molecular anion. *A&A*, 517:L2, 2010.
- [22] T. J. Millar, E. Herbst, and R. P. A. Bettens. Large molecules in the envelope surrounding IRC+10216. *MNRAS*, 316(1):195–203, 2000.

- [23] T. J. Millar, C. Walsh, M. A. Cordiner, R. N. Chuimín, and E. Herbst. Hydrocarbon anions in interstellar clouds and circumstellar envelopes. *ApJ*, 662(2):L87, 2007.
- [24] N. Harada and E. Herbst. Modeling carbon chain anions in L1527. *ApJ*, 685(1):272, 2008.
- [25] E. Herbst and Y. Osamura. Calculations on the formation rates and mechanisms for C_nH^- anions in interstellar and circumstellar media. *ApJ*, 679(2):1670, 2008.
- [26] N. Douguet, S. Fonseca dos Santos, M. Raoult, O. Dulieu, A. E. Orel, and V. Kokoouline. Theory of radiative electron attachment to molecules: Benchmark study of CN^- . *Phys. Rev. A*, 88:052710, 2013.
- [27] N. Douguet, V. Kokoouline, and A. E. Orel. Photodetachment cross sections of the $C_{2n}H^-$ ($n = 1 - 3$) hydrocarbon-chain anions. *Phys. Rev. A*, 90:063410, 2014.
- [28] N. Douguet, S. Fonseca dos Santos, M. Raoult, O. Dulieu, A. E. Orel, and V. Kokoouline. Theoretical study of radiative electron attachment to CN , C_2H , and C_4H radicals. *J. Chem. Phys.*, 142(23):234309, 2015.
- [29] M. Khamesian, N. Douguet, S. Fonseca dos Santos, O. Dulieu, M. Raoult, W. J. Brigg, and V. Kokoouline. Formation of CN^- , C_3N^- and C_5N^- molecules by radiative electron attachment and their destruction by photodetachment. *Phys. Rev. Lett.*, 117:123001, 2016.
- [30] C. Barckholtz, T. P. Snow, and V. M. Bierbaum. Reactions of C_n^- and C_nH^- with atomic and molecular hydrogen. *ApJ*, 547(2):L171, 2001.
- [31] S. S. Kumar, D. Hauser, R. Jindra, T. Best, Š. Roučka, W. D. Geppert, T. J. Millar, and R. Wester. Photodetachment as a destruction mechanism for CN^- and C_3N^- anions in circumstellar envelopes. *ApJ*, 776(1):25, 2013.
- [32] J. Klos and F. Lique. First rate coefficients for an interstellar anion: application to the $CN^- - H_2$ collisional system. *MNRAS*, 418(1):271–275, 2011.
- [33] K. M. Walker, F. Lique, F. Dumouchel, and R. Dawes. Inelastic rate coefficients for collisions of C_6H^- with H_2 and He. *MNRAS*, 466(1):831–837, 2017.
- [34] H.-J. Werner, P. J. Knowles, G. Knizia, F. R. Manby, M. Schütz, P. Celani, W. Györffy, D. Kats, T. Korona, R. Lindh, A. Mitrushenkov, G. Rauhut, K. R. Shamasundar, T. B. Adler, R. D. Amos, A. Bernhardsson, A. Berning, D. L.

- Cooper, M. J. O. Deegan, A. J. Dobbyn, F. Eckert, E. Goll, C. Hampel, A. Hesselmann, G. Hetzer, T. Hrenar, G. Jansen, C. Köppl, Y. Liu, A. W. Lloyd, R. A. Mata, A. J. May, S. J. McNicholas, W. Meyer, M. E. Mura, A. Nicklass, D. P. O'Neill, P. Palmieri, D. Peng, K. Pflüger, R. Pitzer, M. Reiher, T. Shiozaki, H. Stoll, A. J. Stone, R. Tarroni, T. Thorsteinsson, and M. Wang. MOLPRO, version 2012.1, a package of ab initio programs, 2012. see.
- [35] J. Čížek. On the correlation problem in atomic and molecular systems. Calculation of wavefunction components in ursell-type expansion using quantum-field theoretical methods. *J. Chem. Phys.*, 45(11):4256–4266, 1966.
- [36] J. Čížek and J. Paldus. Coupled cluster approach. *Phys. Scr.*, 21(3-4):251, 1980.
- [37] T. H. Dunning. Gaussian basis sets for use in correlated molecular calculations. I. The atoms boron through neon and hydrogen. *J. Chem. Phys.*, 90(2):1007–1023, 1989.
- [38] R. A. Kendall, T. H. Dunning, and R. J. Harrison. Electron affinities of the first-row atoms revisited. Systematic basis sets and wave functions. *J. Chem. Phys.*, 96(9):6796–6806, 1992.
- [39] D. E. Woon and T. H. Dunning. Gaussian basis sets for use in correlated molecular calculations. III. The atoms aluminum through argon. *J. Chem. Phys.*, 98(2):1358–1371, 1993.
- [40] D. E. Woon and T. H. Dunning. Gaussian basis sets for use in correlated molecular calculations. IV. Calculation of static electrical response properties. *J. Chem. Phys.*, 100(4):2975–2988, 1994.
- [41] A. K. Wilson, D. E. Woon, K. A. Peterson, and T. H. Dunning. Gaussian basis sets for use in correlated molecular calculations. IX. The atoms gallium through krypton. *J. Chem. Phys.*, 110(16):7667–7676, 1999.
- [42] J. C. Light and R. B. Walker. An R matrix approach to the solution of coupled equations for atom-molecule reactive scattering. *J. Chem. Phys.*, 65(10):4272–4282, 1976.
- [43] D. E. Manolopoulos. An improved log derivative method for inelastic scattering. *J. Chem. Phys.*, 85(11):6425–6429, 1986.
- [44] J. Lill, G. Parker, and J. Light. Discrete variable representations and sudden models in quantum scattering theory. *Chem. Phys. Lett.*, 89(6):483 – 489, 1982.
- [45] J. C. Light, I. P. Hamilton, and J. V. Lill. Generalized discrete variable approximation in quantum mechanics. *J. Chem. Phys.*, 82(3):1400–1409, 1985.

- [46] J. C. Light and T. Carrington. *Discrete-Variable Representations and their Utilization*, pages 263–310. Wiley-Blackwell, 2007.
- [47] M. Lara-Moreno, T. Stoecklin, P. Halvick, and J.-C. Loison. New single-center approach of photodetachment and radiative electron attachment: Comparison with other theoretical approaches and with experimental photodetachment data. *J. Chem. Phys.*, 2018.
- [48] K. J. Reed, A. H. Zimmerman, H. C. Andersen, and J. I. Brauman. Cross sections for photodetachment of electrons from negative ions near threshold. *J. Chem. Phys.*, 64(4):1368–1375, 1976.
- [49] C. M. Oana and A. I. Krylov. Cross sections and photoelectron angular distributions in photodetachment from negative ions using equation-of-motion coupled-cluster Dyson orbitals. *J. Chem. Phys.*, 131(12):124114, 2009.
- [50] Y. Liu and C. Ning. Calculation of photodetachment cross sections and photoelectron angular distributions of negative ions using density functional theory. *J. Chem. Phys.*, 143(14):144310, 2015.
- [51] L. A. Collins and B. I. Schneider. Molecular photoionization in the linear algebraic approach: H_2 , N_2 , NO , and C_2 . *Phys. Rev. A*, 29:1695–1708, 1984.
- [52] T. N. Rescigno and A. E. Orel. Separable approximation for exchange interactions in electron-molecule scattering. *Phys. Rev. A*, 24:1267–1271, 1981.
- [53] T. N. Rescigno and A. E. Orel. Separable approximation for exchange interactions in electron-molecule scattering: Numerical stabilization procedures. *Phys. Rev. A*, 25:2402–2404, 1982.
- [54] C. M. Granados-Castro, L. U. Ancarani, G. Gasaneo, and D. M. Mitnik. Chapter one - A Sturmian approach to photoionization of molecules. In P. E. Hoggan and T. Ozdogan, editors, *Electron Correlation in Molecules – ab initio Beyond Gaussian Quantum Chemistry*, volume 73 of *Advances in Quantum Chemistry*, pages 3 – 57. Academic Press, 2016.
- [55] W. Sun, R. M. Pitzer, and C. W. McCurdy. Photodetachment cross section for the $3\sigma_u$ channel of f_2^- in the static-exchange approximation. *Phys. Rev. A*, 40:3669–3672, 1989.
- [56] E. Milne. XVIII. Statistical equilibrium in relation to the photo-electric effect, and its application to the determination of absorption coefficients. *Phil. Mag. Series*, 47(277):209–241, 1924.

- [57] J. C. Light, J. Ross, and K. E. Shuler. Rate coefficients, reaction cross sections and microscopic reversibility. In A. R. Hochstim, editor, *Kinetic processes in gases and plasmas*, pages 281–320. Academic Press, New York and London, 1969.
- [58] C. M. Oana and A. I. Krylov. Dyson orbitals for ionization from the ground and electronically excited states within equation-of-motion coupled-cluster formalism: Theory, implementation, and examples. *J. Chem. Phys.*, 127(23):234106, 2007.
- [59] G. Grell, S. I. Bokarev, B. Winter, R. Seidel, E. F. Aziz, S. G. Aziz, and O. Kühn. Multi-reference approach to the calculation of photoelectron spectra including spin-orbit coupling. *J. Chem. Phys.*, 143(7):074104, 2015.
- [60] P. Duffy, D. P. Chong, M. E. Casida, and D. R. Salahub. Assessment of Kohn-Sham density-functional orbitals as approximate Dyson orbitals for the calculation of electron-momentum-spectroscopy scattering cross sections. *Phys. Rev. A*, 50:4707–4728, 1994.
- [61] S. Hamel, P. Duffy, M. E. Casida, and D. R. Salahub. Kohn–Sham orbitals and orbital energies: fictitious constructs but good approximations all the same. *J. Electron Spectrosc. Relat. Phenom.*, 123(2):345 – 363, 2002. Determination of cross-sections and momentum profiles of atoms, molecules and condensed matter.
- [62] F. E. Harris and H. H. Michels. Multicenter integrals in quantum mechanics. I. Expansion of Slater type orbitals about a new origin. *J. Chem. Phys.*, 43(10):S165–S169, 1965.
- [63] H. Le Rouzo. Multipole expansion of Cartesian Gaussian orbitals about a new origin. *Int. J. Quantum Chem.*, 64(6):647–653, 1997.
- [64] I. Ema, J. M. García de la Vega, G. Ramírez, R. López, R. J. Fernández, H. Meissner, and J. Paldus. Polarized basis sets of slater-type orbitals: H to ne atoms. *J. Comput. Chem.*, 24(7):859–868, 2003.
- [65] R. J. Fernández, R. López, I. Ema, and G. Ramírez. Efficiency of the algorithms for the calculation of slater molecular integrals in polyatomic molecules. *J. Comput. Chem.*, 25(16):1987–1994, 2004.
- [66] M. A. Morrison and L. A. Collins. Exchange in low-energy electron-molecule scattering: Free-electron-gas model exchange potentials and applications to e^- -H₂ and e^- -N₂ collisions. *Phys. Rev. A*, 17:918–938, 1978.

- [67] N. T. Padial and D. W. Norcross. Parameter-free model of the correlation-polarization potential for electron-molecule collisions. *Phys. Rev. A*, 29:1742–1748, 1984.
- [68] W. N. Sams and D. J. Kouri. Noniterative solutions of integral equations for scattering. I. Single channels. *J. Chem. Phys.*, 51(11):4809–4814, 1969.
- [69] W. N. Sams and D. J. Kouri. Noniterative solutions of integral equations for scattering. II. Coupled channels. *J. Chem. Phys.*, 51(11):4815–4819, 1969.
- [70] R. G. Tonkyn, J. W. Winniczek, and M. G. White. Rotationally resolved photoionization of O_2^+ near threshold. *Chem. Phys. Lett.*, 164(2):137–142, 1989.
- [71] K. M. Ervin, I. Anusiewicz, P. Skurski, J. Simons, and W. C. Lineberger. The only stable state of O_2^- is the $X^2\Pi_g$ ground state and it (still!) has an adiabatic electron detachment energy of 0.45 eV. *J. Phys. Chem. A*, 107(41):8521–8529, 2003.
- [72] K. P. Huber and G. H. (auth.). *Molecular Spectra and Molecular Structure: IV. Constants of Diatomic Molecules*. Springer US, 1 edition, 1979.
- [73] S. E. Bradforth, E. H. Kim, D. W. Arnold, and D. M. Neumark. Photoelectron spectroscopy of CN^- , NCO^- , and NCS^- . *J. Chem. Phys.*, 98(2):800–810, 1993.
- [74] R. T. Wiedmann, R. G. Tonkyn, M. G. White, K. Wang, and V. McKoy. Rotationally resolved threshold photoelectron spectra of OH and OD. *J. Chem. Phys.*, 97(2):768–772, 1992.
- [75] J. R. Smith, J. B. Kim, and W. C. Lineberger. High-resolution threshold photodetachment spectroscopy of OH^- . *Phys. Rev. A*, 55:2036–2043, 1997.
- [76] G. Parlant and F. Fiquet-Fayard. The $O_2^2\Pi_g$ resonance: theoretical analysis of electron scattering data. *J. Phys. B At. Mol. Phys.*, 9(9):1617, 1976.
- [77] L. M. Branscomb. Photodetachment cross section, electron affinity, and structure of the negative hydroxyl ion. *Phys. Rev.*, 148:11–18, 1966.
- [78] S. Gozem and A. I. Krylov. ezDyson user’s manual. <http://iopenshell.usc.edu/downloads/>.
- [79] S. Gozem, A. O. Gunina, T. Ichino, D. L. Osborn, J. F. Stanton, and A. I. Krylov. Photoelectron wave function in photoionization: Plane wave or coulomb wave? *J. Phys. Chem. Lett.*, 6(22):4532–4540, 2015.

- [80] R. A. Beyer and J. A. Vanderhoff. Cross section measurements for photodetachment or photodissociation of ions produced in gaseous mixtures of O₂, CO₂, and H₂O. *J. Chem. Phys.*, 65(6):2313–2321, 1976.
- [81] D. S. Burch, S. J. Smith, and L. M. Branscomb. Photodetachment of O⁻. *Phys. Rev.*, 112:171–175, 1958.
- [82] L. C. Lee and G. P. Smith. Photodissociation and photodetachment of molecular negative ions. VI. ions in O₂/CH₄/H₂O mixtures from 3500 to 8600 Å. *J. Chem. Phys.*, 70(4):1727–1735, 1979.
- [83] S. Trippel, J. Mikosch, R. Berhane, R. Otto, M. Weidemüller, and R. Wester. Photodetachment of cold OH⁻ in a multipole ion trap. *Phys. Rev. Lett.*, 97:193003, 2006.
- [84] P. Hlavenka, R. Otto, S. Trippel, J. Mikosch, M. Weidemüller, and R. Wester. Absolute photodetachment cross section measurements of the O⁻ and OH⁻ anion. *J. Chem. Phys.*, 130(6):061105, 2009.
- [85] W. Skomorowski, S. Gulania, and A. I. Krylov. Bound and continuum-embedded states of cyanopolyynes anions. *Phys. Chem. Chem. Phys.*, 20:4805–4817, 2018.
- [86] S. J. Burns, J. M. Matthews, and D. L. McFadden. Rate coefficients for dissociative electron attachment by halomethane compounds between 300 and 800 K. *J. Chem. Phys.*, 100(50):19436–19440, 1996.
- [87] L. G. Christophorou and J. K. Olthoff. Electron attachment cross sections and negative ion states of SF₆. *Int. J. Mass Spec.*, 205(1):27 – 41, 2001. Low Energy Electron-Molecule Interactions (Stamatovic honor).
- [88] A. A. Viggiano, T. M. Miller, J. F. Friedman, and J. Troe. Low-energy electron attachment to SF₆. III. From thermal detachment to the electron affinity of SF₆. *J. Chem. Phys.*, 127(24):244305, 2007.
- [89] W. B. Knighton, T. M. Miller, E. P. Grimsrud, and A. A. Viggiano. Electron attachment to PSCl₃. *J. Chem. Phys.*, 120(1):211–216, 2004.
- [90] S. Petrie. Novel pathways to CN⁻ within interstellar clouds and circumstellar envelopes: implications for IS and CS chemistry. *MNRAS*, 281(1):137–144, 1996.
- [91] S. Petrie and E. Herbst. Some interstellar reactions involving electrons and neutral species: Attachment and isomerization. *Astrophys. J.*, 491(1):210, 1997.

- [92] T. Pino, M. Tulej, F. Güthe, M. Pachkov, and J. P. Maier. Photodetachment spectroscopy of the $C_{2n}H^-$ ($n = 2 - 4$) anions in the vicinity of their electron detachment threshold. *J. Chem. Phys.*, 116(14):6126–6131, 2002.
- [93] T. Best, R. Otto, S. Trippel, P. Hlavenka, A. von Zastrow, S. Eisenbach, S. Jézouin, R. Wester, E. Vigrén, M. Hamberg, and W. D. Geppert. Absolute photodetachment cross-section measurements for hydrocarbon chain anions. *ApJ*, 742(2):63, 2011.
- [94] A. N. Heays, A. D. Bosman, and E. F. van Dishoeck. Photodissociation and photoionisation of atoms and molecules of astrophysical interest. *A&A*, 602: A105, 2017.
- [95] E. P. Wigner. On the behavior of cross sections near thresholds. *Phys. Rev.*, 73: 1002–1009, 1948.
- [96] M. A. Cordiner and T. J. Millar. Density-enhanced gas and dust shells in a new chemical model for irc+10216. *The Astrophysical Journal*, 697(1):68, 2009.
- [97] F. Carelli, F. A. Gianturco, R. Wester, and M. Satta. Formation of cyanopolyynes anions in the interstellar medium: The possible role of permanent dipoles. *J. Chem. Phys.*, 141(5):054302, 2014.
- [98] K. Connolly and D. J. Griffiths. Critical dipoles in one, two, and three dimensions. *Am. J. Phys*, 75(6):524–531, 2007.
- [99] M. Lara-Moreno, T. Stoecklin, and P. Halvick. Interaction of rigid C_3N^- with He: Potential energy surface, bound states, and rotational spectrum. *J. Chem. Phys.*, 146(22):224310, 2017.
- [100] R. Kołos, M. Gronowski, and P. Botschwina. Matrix isolation IR spectroscopic and ab initio studies of c_3n^- and related species. *J. Chem. Phys.*, 128(15):154305, 2008.
- [101] T. Stoecklin, O. Denis-Alpizar, and P. Halvick. Rovibrational energy transfer in the He– C_3 collision: rigid bender treatment of the bending-rotation interaction and rate coefficients. *MNRAS*, 449(4):3420–3425, 2015.
- [102] C. Hampel, K. A. Peterson, and H.-J. Werner. A comparison of the efficiency and accuracy of the quadratic configuration interaction (QCISD), coupled cluster (CCSD), and Brueckner coupled cluster (BCCD) methods. *Chem. Phys. Lett.*, 190(1):1 – 12, 1992.

- [103] S. M. Cybulski and R. R. Toczyłowski. Ground state potential energy curves for He₂, Ne₂, Ar₂, He–Ne, He–Ar, and Ne–Ar: A coupled-cluster study. *J. Chem. Phys.*, 111(23):10520–10528, 1999.
- [104] S. Boys and F. Bernardi. The calculation of small molecular interactions by the differences of separate total energies. Some procedures with reduced errors. *Mol. Phys.*, 19(4):553–566, 1970.
- [105] Y. Ajili, T. Trabelsi, O. Denis-Alpizar, T. Stoecklin, A. G. Császár, M. Mogren Al-Mogren, J. S. Francisco, and M. Hochlaf. Vibrational memory in quantum localized states. *Phys. Rev. A*, 93:052514, 2016.
- [106] D. Papp, J. Sarka, T. Szidarovszky, A. G. Csaszar, E. Matyus, M. Hochlaf, and T. Stoecklin. Complex rovibrational dynamics of the Ar–NO⁺ complex. *Phys. Chem. Chem. Phys.*, 19:8152–8160, 2017.
- [107] M. Rotenberg. *Theory and Application of Sturmian Functions*, volume 6 of *Advances in Atomic and Molecular Physics*. Academic Press, 1970.
- [108] E. Yurtsever, O. Yilmaz, and D. Shillady. Sturmian basis matrix solution of vibrational potentials. *Chem. Phys. Lett.*, 85(1):111 – 116, 1982.
- [109] S. E. Choi and J. C. Light. Determination of the bound and quasibound states of Ar–HCl van der Waals complex: Discrete variable representation method. *J. Chem. Phys.*, 92(4):2129–2145, 1990.
- [110] J. Hutson. *An introduction to the dynamics of van der Waals complexes*, volume 1A of *Advances in Molecular Vibrations and Collision Dynamics*. JAI Press, Greenwich, 1991.
- [111] M. Lara-Moreno, T. Stoecklin, and P. Halvick. Rotational (de-)excitation of C₃N[−] by collision with He atoms. *MNRAS*, 467(1):4174, 2017.
- [112] F. Dumouchel, A. Spielfiedel, M. Senent, and N. Feautrier. Temperature dependence of rotational excitation rate coefficients of C₂H[−] in collision with He. *Chem. Phys. Lett.*, 533:6 – 9, 2012.
- [113] T. A. Yen, E. Garand, A. T. Shreve, and D. M. Neumark. Anion photoelectron spectroscopy of C₃N[−] and C₅N[−]. *J. Phys. Chem. A*, 114(9):3215–3220, 2010. PMID: 20000480.
- [114] O. Denis-Alpizar, T. Stoecklin, P. Halvick, and M.-L. Dubernet. Rotational relaxation of CS by collision with *ortho*- and *para*-H₂ molecules. *J. Chem. Phys.*, 139(20):204304, 2013.

- [115] G. Guillon, T. Stoecklin, A. Voronin, and P. Halvick. Rotational relaxation of HF by collision with *ortho*- and *para*-H₂ molecules. *J. Chem. Phys.*, 129(10): 104308, 2008.
- [116] M. L. Dubernet, F. Daniel, A. Grosjean, and C. Y. Lin. Rotational excitation of *ortho*-H₂O by *para*-H₂ ($j_2 = 0, 2, 4, 6, 8$) at high temperature. *A&A*, 497(3): 911–925, 2009.
- [117] F. Lique, R. Tobała, J. Kłos, N. Feautrier, A. Spielfiedel, L. F. M. Vincent, G. C. iński, and M. H. Alexander. Can we estimate H₂ ($j = 0$) rate coefficients from He rate coefficients? Application to the SiS molecule. *A&A*, 478(2):567–574, 2008.
- [118] J. Cernicharo, A. Spielfiedel, C. Balança, F. Dayou, M.-L. Senent, N. Feautrier, A. Faure, L. Cressiot-Vincent, L. Wiesenfeld, and J. R. Pardo. Collisional excitation of sulfur dioxide in cold molecular clouds. *A&A*, 531:A103, 2011.
- [119] K. M. Walker, B. H. Yang, P. C. Stancil, N. Balakrishnan, and R. C. Forrey. On the validity of collider-mass scaling for molecular rotational excitation. *ApJ*, 790(2):96, 2014.
- [120] A. E. DePristo, S. D. Augustin, R. Ramaswamy, and H. Rabitz. Quantum number and energy scaling for nonreactive collisions. *J. Chem. Phys.*, 71(2): 850–865, 1979.
- [121] G. C. Corey and F. R. McCourt. Inelastic differential and integral cross sections for $^{2S+1}\Sigma$ linear molecule- 1S atom scattering: The use of hund’s case (b) representation. *J. Phys. Chem.*, 87(15):2723–2730, 1983.
- [122] D. H. Zhang and J. Z. H. Zhang. Uniform J-shifting approach for calculating reaction rate constant. *J. Chem. Phys.*, 110(16):7622–7626, 1999.
- [123] A. M. Arthurs and A. Dalgarno. The theory of scattering by a rigid rotator. *Proc. R. Soc. London. Series A, Math. Phys. Sci.*, 256(1287):540–551, 1960.
- [124] I. C. Percival and M. J. Seaton. The partial wave theory of electron-hydrogen atom collisions. *Math. Proc. Cambridge Philos. Soc.*, 53(3):654–662, 1957.
- [125] T. Stoecklin, A. Voronin, and J. C. Rayez. Vibrational quenching of N₂($v = 1, j_{\text{rot}} = j$) by ^3He : Surface and close-coupling calculations at very low energy. *Phys. Rev. A*, 66:042703, 2002.
- [126] F. Lique, N. Bulut, and O. Roncero. Hyperfine excitation of OH⁺ by H. *MNRAS*, 461:4477, 2016.

- [127] G. Werfelli, P. Halvick, P. Honvault, B. Kerkeni, and T. Stoecklin. Low temperature rate coefficients of the $\text{H} + \text{CH}^+ \rightarrow \text{C}^+ + \text{H}_2$ reaction: New potential energy surface and time-independent quantum scattering. *J. Chem. Phys.*, 143(11):114304, 2015.
- [128] C. W. McCurdy and W. H. Miller. Interference effects in rotational state distributions: Propensity and inverse propensity. *J. Chem. Phys.*, 67(2):463–468, 1977.
- [129] M. Wernli, L. Wie, A. Faure, and P. Valiron. Rotational excitation of HC_3N by H_2 and He at low temperatures. *A&A*, 464(3):1147–1154, 2007.
- [130] P. Langevin. Une formule fondamentale de theorie cinetique. *Ann. Chim. Phys*, 5:245, 1905.
- [131] G. Gioumousis and D. P. Stevenson. Reactions of gaseous molecule ions with gaseous molecules. V. Theory. *J. Chem. Phys.*, 29(2):294–299, 1958.
- [132] R. McGill, J. W. Tukey, and W. A. Larsen. Variations of Box Plots. *Am. Stat.*, 32(1):12–16, 1978.
- [133] M. Frigge, D. C. Hoaglin, and B. Iglewicz. Some implementations of the Boxplot. *Am. Stat.*, 43(1):50–54, 1989.
- [134] P. Halvick, T. Stoecklin, F. Lique, and M. Hochlaf. Explicitly correlated treatment of the Ar-NO^+ cation. *J. Chem. Phys.*, 135(4):044312, 2011.
- [135] C. Orek, J. Kłos, F. Lique, and N. Bulut. Ab initio studies of the $\text{Rg-NO}^+(\text{X}^1\Sigma^+)$ van der Waals complexes ($\text{Rg} = \text{He, Ne, Ar, Kr, and Xe}$). *J. Chem. Phys.*, 144(20):204303, 2016.
- [136] G. B. Arfken. *Mathematical methods for physicists*. Academic Press, 3rd edition, 1985.
- [137] A. D. Buckingham. *Permanent and Induced Molecular Moments and Long-Range Intermolecular Forces*, chapter 2, pages 107–142. Wiley-Blackwell, 2007.
- [138] D. Shiner, J. M. Gilligan, B. M. Cook, and W. Lichten. H_2 , D_2 and HD ionization potentials by accurate calibration of several iodine lines. *Phys. Rev. A*, 47:4042–4045, 1993.
- [139] P. Bunker. *Molecular Symmetry and Spectroscopy*. Elsevier Science, 2012.
- [140] J. C. Light and Z. Bačić. Adiabatic approximation and nonadiabatic corrections in the discrete variable representation: Highly excited vibrational states of triatomic molecules. *J. Chem. Phys.*, 87(7):4008–4019, 1987.

- [141] E. Wilson, J. Decius, and P. Cross. *Molecular Vibrations: The Theory of Infrared and Raman Vibrational Spectra*. Dover Books on Chemistry. Dover Publications, 2012.
- [142] G. F. Englot and H. Rabitz. Dimensionality control of coupled scattering equations using partitioning techniques: The case of two molecules. *Phys. Rev. A*, 10:2187–2205, 1974.
- [143] S. Green. Rotational excitation in H₂–H₂ collisions: Close-coupling calculations. *J. Chem. Phys.*, 62(6):2271–2277, 1975.
- [144] G. Herzberg and L. L. Howe. The lyman bands of molecular hydrogen. *Can. J. Phys.*, 37(5):636–659, 1959.
- [145] M. Lara-Moreno, T. Stoecklin, P. Halvick, and M. Hochlaf. Quantum tunneling dynamical behaviour on weakly bound complexes: the case of a CO₂–N₂ dimer. *Phys. Chem. Chem. Phys.*, doi:10.1039/C8CP04465A, 2018.
- [146] M. A. Walsh, T. R. Dyke, and B. J. Howard. Determination of the structure of N₂ – CO₂ from its infrared spectrum. *J. Mol. Struct.*, 189(1):111 – 120, 1988.
- [147] J. A. G. Castano, A. Fantoni, and R. M. Romano. Matrix-isolation FTIR study of carbon dioxide: Reinvestigation of the CO₂ dimer and CO₂ – N₂ complex. *J. Mol. Struct.*, 881(1):68 – 75, 2008.
- [148] D. J. Frohman, E. S. Contreras, R. S. Firestone, S. E. Novick, and W. Klemperer. Microwave spectra, structure, and dynamics of the weakly bound complex, N₂ – CO₂. *J. Chem. Phys.*, 133(24):244303, 2010.
- [149] T. Konno, S. Yamaguchi, and Y. Ozaki. Infrared diode laser spectroscopy of N₂ – ¹²C¹⁸O₂. *J. Mol. Spectrosc.*, 270(1):66 – 69, 2011.
- [150] M. Venayagamoorthy and T. Ford. Ab initio molecular orbital studies of the vibrational spectra of some van der waals complexes. part 1. complexes of molecular nitrogen with carbon dioxide, nitrous oxide, carbonyl sulphide and carbon disulphide. *J. Mol. Struct.*, 565-566:399 – 409, 2001.
- [151] J. Fišer, T. Boublík, and R. Polák. Intermolecular interactions in the (CO₂)₂, N₂ – CO₂ and CO – CO₂ complexes. *Collect. Czech. Chem. Commun*, 69(1):177–188, 2004.
- [152] K. M. de Lange and J. R. Lane. Explicit correlation and intermolecular interactions: Investigating carbon dioxide complexes with the CCSD(T) – F12 method. *J. Chem. Phys.*, 134(3):034301, 2011.

- [153] S. Nasri, Y. Ajili, N.-E. Jaidane, Y. N. Kalugina, P. Halvick, T. Stoecklin, and M. Hochlaf. Potential energy surface of the CO₂ – N₂ van der Waals complex. *J. Chem. Phys.*, 142(17):174301, 2015.
- [154] J. Tennyson and A. van der Avoird. Quantum dynamics of the van der Waals molecule (N₂)₂: An ab initio treatment. *J. Chem. Phys.*, 77(11):5664–5681, 1982.
- [155] H. Chen and J. C. Light. Vibrations of the carbon dioxide dimer. *J. Chem. Phys.*, 112(11):5070–5080, 2000.
- [156] R. Zare. *Angular momentum: understanding spatial aspects in chemistry and physics*. George Fisher Baker non-resident lectureship in chemistry at Cornell University. Wiley, 1988.
- [157] L. Wang, M. Yang, A. R. W. McKellar, and D. H. Zhang. Spectroscopy and potential energy surface of the H₂ – CO₂ van der waals complex: experimental and theoretical studies. *Phys. Chem. Chem. Phys.*, 9:131–137, 2007.
- [158] Z. Bačić and J. C. Light. Accurate localized and delocalized vibrational states of HCN/HNC. *J. Chem. Phys.*, 86(6):3065–3077, 1987.
- [159] S. Zou, J. M. Bowman, and A. Brown. Full-dimensionality quantum calculations of acetylene-vinylidene isomerization. *J. Chem. Phys.*, 118(22):10012–10023, 2003.
- [160] J. H. Baraban, P. B. Changala, G. C. Mellau, J. F. Stanton, A. J. Merer, and R. W. Field. Spectroscopic characterization of isomerization transition states. *Science*, 350(6266):1338–1342, 2015.
- [161] W. Arbelo-González, R. Crespo-Otero, and M. Barbatti. Steady and time-resolved photoelectron spectra based on nuclear ensembles. *J. Chem. Theory Comput.*, 12(10):5037–5049, 2016.

TITRE: Etude des mécanismes possibles de formation et de destruction d'anions dans le milieu interstellaire.

RÉSUMÉ: L'étude des mécanismes de formation et de destruction des anions moléculaires est devenu un champ d'intérêt prononcé après la détection récente de six anions moléculaires (C_4H^- , C_6H^- , C_8H^- , CN^- , C_3N^- , C_5N^-) dans le milieu interstellaire. Dans les environnements interstellaires où la densité d'électrons est relativement importante, le canal principal de formation de ces anions devrait être l'attachement électronique radiatif. Mais il manque aujourd'hui des données expérimentales et théoriques permettant d'évaluer cette hypothèse. D'autre part, le photodétachement est la principale cause de destruction de ces anions dans les nuages diffus et les régions de photodissociation. Une approche basée sur un développement monocentrique est appliquée à l'étude de ces deux processus opposés que sont le photodétachement et l'attachement électronique radiatif. Les résultats obtenus avec la présente méthode sont comparés à des données expérimentales et théoriques précédemment rapportées et montrent un bon accord. Cette méthode est ensuite utilisée pour déterminer les constantes de vitesse nécessaires pour confirmer si ces mécanismes sont cruciaux pour la chimie d'anions interstellaires. En plus des constantes de vitesse de formation et de destruction des anions, les constantes de vitesse d'excitation collisionnelle sont nécessaires pour modéliser les abondances observées des anions. Nous avons choisi de porter notre effort sur le calcul des constantes de vitesse de transition entre états rotationnels de la molécule C_3N^- dans son état vibrationnel fondamental lors des collisions avec H_2 et He en utilisant de nouvelles surfaces d'énergie potentielles.

MOTS CLÉS: anions interstellaires, attachement électronique radiatif, photodétachement, constantes de vitesse de transitions rotationnelle, surfaces d'énergie potentielle.

TITLE: Study of the possible mechanism of formation and destruction of anions in the interstellar medium

ABSTRACT: The mechanisms of formation and destruction of molecular anions have become a field of special interest after the recent detection of six molecular anions (C_4H^- , C_6H^- , C_8H^- , CN^- , C_3N^- , C_5N^-) in the interstellar medium. The main channel of formation of these anions is expected to be radiative electron attachment in environments where the density of electron is relatively important. There is however at the moment a lack of experimental and theoretical data allowing to assess this hypothesis. Photodetachment, on the other hand, is the main source of destruction of the anions in diffuse clouds and photodissociation regions. A single center expansion approach is applied to the study of both processes: photodetachment and radiative electron attachment. The results obtained with the present method are compared to previously reported experimental and theoretical data and show a good agreement. This method is then employed to determine the rate constants which are needed to confirm whether or not these mechanisms are crucial for the chemistry of the interstellar anions. Along with the formation and destruction rates, rotational excitation rate coefficients are needed to accurately model the observed anions abundances. We focus on the calculation of state-to-state rotational transitions rate coefficients of the C_3N^- molecule in its ground vibrational state in collisions with H_2 and He using new potential energy surfaces.

KEYWORDS: interstellar anions, radiative electron attachment, photodetachment, state-to-state rate coefficients, potential energy surfaces
